SLURRY EROSION BEHAVIOR OF OIL AND GAS PIPELINE STEELS

by

Tahrim Alam

Submitted in partial fulfilment of the requirements
for the degree of Master of Applied Science

at

Dalhousie University
Halifax, Nova Scotia
April 2016

To my wonderful wife and family – those who suffered

Table of Contents

List of Tables

List of Figures

Abstract

Slurry erosion is a destructive process encountered in oil and gas transmission pipelines. During transportation, the inner surface of pipelines are exposed to flowing abrasive liquid which causes slurry erosion. Complex mechanism and progressive nature of this problem create augmented challenges to pipeline economy and operation. Oil and gas industries spend millions of dollars to deal with the problems caused by wet erosion. Material integrity and degradation rate are key factors in the long-term performance of oil and gas pipeline networks. This research focuses on understanding the degradation processes of pipeline steels caused by the slurry erosion. The effects of slurry velocity and abrasive concentrations on erosion rate and mechanisms are identified and discussed in details. The present research also correlates the slurry erosion response of steel to its microstructure.

List of Abbreviations and Symbols Used

Abbreviations

AcC	Accelerated Cooling
AISI	American Iron and Steel Institute
API	American Petroleum Institute
ASTM	American Society for Testing and Materials
BCC	Body Centered Cubic
BE	Binding Energy
BS	British Standards
CFD	Computational Fluid Dynamics
CST	Cooling Stop Temperature
DH	Dislocation Hardening
DIN	Germany Steel Grades
EDS	Energy Dispersive Spectroscopy
EOR	Enhanced Oil Recovery
FBC	Fluidized Bed Combustion
FRT	Finish Rolling Temperature
GB	China Steel Grades
GR	Grain Refinement
HSLA	High-strength Low Alloy Steel
HSS	High-strength Steel
ICP	Inductively Coupled Plasma Mass Spectrometry
ISO	International Organization for Standardization

JIS	Japanese Steel Grades
JISC	Japanese Industrial Standards Committee
KE	Kinetic Energy
M	Molar
NBS	National Standards Body
PR	Pearlite Reduction
R_a	Average Roughness
SAE	Society of Automotive Engineers
SPE	Solid Particle Erosion
TMT	Thermo-Mechanical Treatment
UNS	Unified Numbering System
XRD	X-ray Diffraction

Symbols

a	Thermal diffusivity of the erodent, (m^2 s^{-1})
A	Surface area (mm^2)
Cp	Specific heat
d	Density (g cm^{-3})
D_t	Density of target material
D_p	Density of abrasive particle
E	Normalized erosion rate
E_1	Erosion rate
EW	Equivalent weight
f_c	Proportion of particles impacting the surface
H_s	Static hardness of target material
H_d	Dynamic hardness of target material
k	Constant
n	Velocity exponent
r_0	Radius of the erodent (m)
S	Synergistic component

t	Test duration (s)
T	Total mass loss rate of the material (μm s^{-1})
T_m	Melting temperature
V_1	Velocity (m s^{-1})
V_m	Volume of material removed
ΔW	Weight loss of the specimen (g)
α	Particle impact angle (°)
a_r/ε_c^2	Constant (0.7)
v	Particle velocity (m s^{-1})

Acknowledgements

Foremost, I would like to thank my supervisor, Professor Dr. Zoheir Farhat, director of the Advanced Tribology Laboratory (ATL). I am extremely fortunate to have an advisor who guided me all the times when my steps faltered and act as my mentor and guardian for last two years. He has been supportive since the first day I started working at ATL group. His insightful comments and constructive criticisms motivated me to focus my ideas and raise my standards. He taught me how to express ideas by questioning thoughts. My learning from Dr. Farhat was not only confined into research. I strongly believe my experience at ATL group will be an asset for the next step of my life. Thank you Dr. Farhat for being such an amazing mentor.

I would like to express my sincerest gratitude to Dr. George Jarjoura. I am deeply grateful to him for all his help and invaluable suggestions. Also, I would like to thank Dr. Hany El Naggar for agreeing to be my thesis committee member. Thank you for guiding me throughout my journey.

I am indebted to the members of ATL. I would like to express my heartfelt gratitude to Dr. Md. Aminul Islam. Whenever I was in trouble, he was always the helping hand. His patience and support helped me overcome many crisis situations. Thank you very much Murad bhai (MD). I would also like to thankfully acknowledge the contribution of my group mate Iris. I appreciate the help and support I received from my colleagues and friends Shahriar Iqbal, Tousif Ahmed, Rabin Neupane, Abdullah Almotairi, Chenxin Jin, Mark Amegadzie and all my present and past group members. I am grateful to Dean Grijm of the machine and instrument shops for his amazing help and support. I would also like to thank Patricia Scallion of IRM and Gerald Fraser of the Materials Engineering Center.

Most importantly, I must express my very profound gratitude to all my family members. My parents have been a source of encouragement and inspiration throughout my whole life. I would like to acknowledge the endless love and support of my brother Rumi, my sisters Sumi & Tushi and my sister-in-law Shifa.

Last but not the least, none of this would have been possible without the love and patience of my wife, Disha. I am not sure that I could've finish my degree without your love, care and constant support. Thank you very much for being there for me all the time.

This publication was made possible by NPRP grant no. 6-027-2-010 from the Qatar National Research Fund (a member of Qatar Foundation). The statements made herein are solely the responsibility of the authors.

Tahrim Alam

April, 2016

Chapter 1

Introduction

Oil and gas are foremost sources used to meet the increasing demand of energy in recent years. Hydro transportation is the most economical and flexible way to transport oil and gas from production sites to the consumer and can last for several decades with minimal maintenance. Pipeline transportation is also the most used mode to carry petroleum products to refineries and consumers. North America, has approximately 500,000 miles of transmission pipeline network for the transportation of oil and natural gas with 2 million miles of inter-city natural gas distribution pipelines [1], [2]. Figure 1-1 shows the relative transportation mode used in USA to carry oil and petroleum based products [3]. Recent data presents that 120 countries use slightly less than 3.5 million km of transportation pipeline while 75% of pipelines are used in USA, Russia and Canada [4].

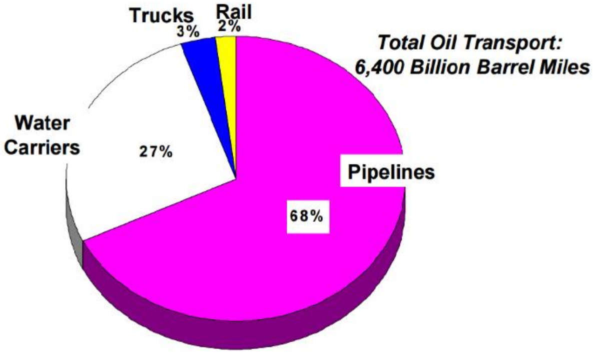

Figure 1-1 **Relative transportation mode of domestic shipments of oil and petroleum products in USA** [3].

Pipelines provide enormous economic facility. Pipelines are more cost effective compared to other alternative transportation options such as: tanker trucks and rail roads. Also, the required energy to operate transportation pipelines is significantly lower than trucks or rail roads. In addition, pipelines have a lower carbon footprint, less spill rate per barrel and produce negligible environmental pollution. Furthermore, pipelines are mostly buried underground, which provide a safer passage for transportation. Table 1 shows the incident rates for different transportation modes where it is evident that the majority of the incidents occur in roads and rails.

Table 1-1 **Petroleum and natural-gas incident rates: pipelines vs road and railway (2005-2009)** [5].

Mode	Avg. billion ton-miles per year	Avg. incidents per year	Incidents per billion ton-miles
Road	34.8	695.2	19.95
Railway	23.9	49.6	2.08
Petroleum pipeline	584.1	339.6	0.58
Natural gas pipeline	338.5	299.2	0.89

Low carbon steels and high strength low alloy steels (HSLA) are extensively used in the production of pipelines. HSLA steels, such as, API X-series steels [6] are most utilized in oil and gas transportation pipelines. During oil and gas transmission, pipelines are subjected to enormous pressure. Thus, pipeline materials have to possess high strength, toughness and optimized geometry in order to transmit oil and gas without failure [7]. API X-series steels offer high strength, good weldability and low price to strength ratio which make them suitable option for pipeline industries.

The historical development of HSLA steels is illustrated in Figure 1-2 [8]. In early seventies, thermomechanical rolling was introduced replacing hot rolling and normalizing. The latter process enables materials up to API X70 (480 MPa) to be produced from steels that are micro-alloyed with niobium and vanadium with reduced carbon content. An improved processing method, consisting of thermo-mechanical rolling with subsequent accelerated cooling, has emerged in the eighties. Introducing this new method result in development of high-strength steels with reducing carbon content (excellent field weldability). API X80 is the example of this new high strength steel. Accordingly, addition of alloying elements such as: Mo, Cu and Ni along with thermo-mechanical rolling with modified accelerated cooling raise the strength way higher and results in new steel grades API X100 and API X120.. In recent years, API X70 and API X80 are the most used steel grades employed in to long distance pipelines whereas API X100 and API X120 steels are being extensively evaluated [9].

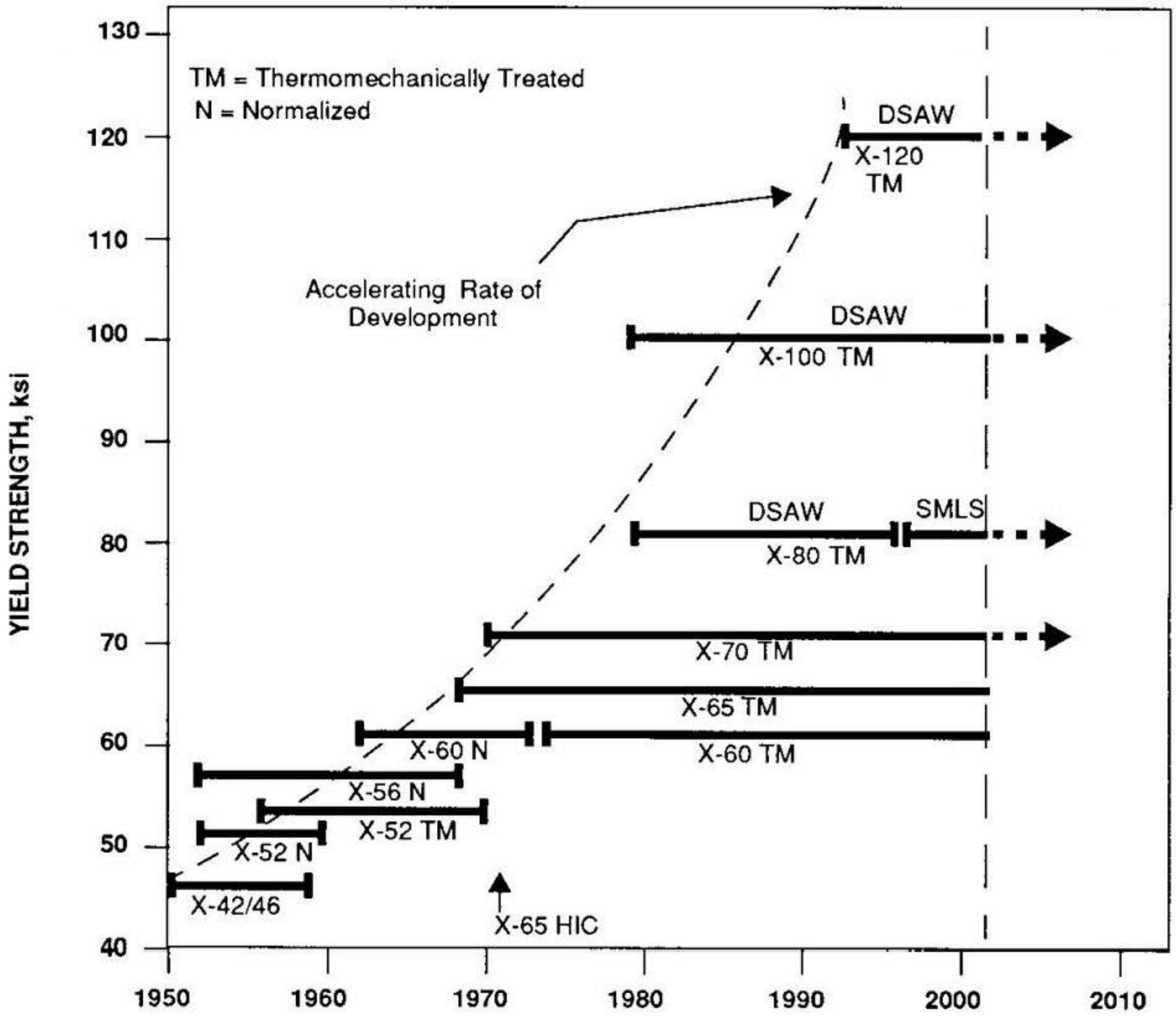

Figure 1-2 **Historical development of API X-series pipeline steels** [8].

However, one major drawback of carbon steels and API X-series steels is their susceptibility to erosion degradation. The co-existence of three phases: carrier liquid (oil), hard solid particles (abrasive particles) and material surface (pipeline inner surface) are responsible for slurry erosion in pipelines [10]. Despite pipelines good safety record, this complex mode of failure reduces the pipe wall thickness [11] and shortens the life span of pipelines. This causes irreversible damage to life and environment [12], [13]. It also causes damage to power plants, heater drain pipings, feedwater lines, etc. Erosion damage has been recognized as a potential safety issue after the pipe rupture incident at Surry Power station in December 1986 [14]. In addition, some other incidents of pipe wall thinning is summarized in Table 1-2 [14]. The erosion-corrosion damage-related cost to the global transmission pipeline industry is approximately $50 billion annually. Hence, slurry erosion has received significant attention among researchers in recent years.

Table 1-2 Petroleum and natural-gas incident rates: pipelines vs road and railway (2005-2009) [14].

Plant	Year	Description	Reference
Oconee 3	1976	Extraction line pinhole leak	NRC IN 82-22
Oconee 3	1980	Replace erosion/corrosion thinned elbow	NRC IN 82-22
Browns Ferry 1	1982	Failure of 8-inch discharge line on the MSR drain pump	INPO Significant Event Report (SER) 41-82
Oconee 2	1983	Failure of a 3- to 10-inch expander downstream of a reheater drain tank	INPO SER 23-85
Calvert Cliffs 1	1984	Rupture of a 16-inch elbow in a branch line from a cold reheat steam line	INPO LER 88-84
Haddam Neck	1985	Pipe rupture downstream of a feedwater heater	INPO Licensee Event Report (LER) 305-85006
Kewaunee	1985	Rupture of a 2-inch excess steam vent line from a MSR	INPO LER 305-85017
Hatch 2	1986	Rupture of a 20- to 16-inch reducer in an extraction steam line	INPO LER 366-86010
Ginna	1986	Failure of a 6-inch elbow of a moisture separator reheater drain line	INPO LER 244-86004

1.1 Objectives

In order to mitigate slurry erosion in practice, a fundamental understanding of the erosion behavior of carbon and low alloy steels is necessary to develop strategies for combating degradation and prolonging the life of the steel pipe. However, slurry erosion mechanism is a complex phenomenon and is not well understood. Furthermore, erosion mechanisms are greatly influenced by several environmental factors. Studying a single variable even in a laboratory scale is a challenging task as all these factors are closely intertwined. The present study examines the slurry erosion behavior of AISI 1018, AISI 1080, API X42, API X70, API X80, API X100 and API X120 steels under different environmental conditions. The research provides a comprehensive and a systematic investigation on the effect of slurry velocity and slurry concentration on erosion behavior of steel. In addition, the study also correlates the erosion response to the steel microstructure. This information provides engineers and designers with the necessary data to make appropriate material selection decisions under different operating conditions.

Slurry erosion is responsible for major failures in oil and gas transmission pipelines and affects many industries, including pipelines, pumps, turbines, offshore structures, etc. The current study generates new knowledge governing materials behavior under erosion attack. The work is expected to create interest from pipeline engineers, designers and pipeline industries. The specific objectives of the research are summarized as follows:

1. Investigate the effect of slurry velocity on erosion of carbon and API X-series steels.
2. Investigate the effect of slurry concentration on erosion behavior of carbon and low alloy steels.
3. Investigate the effect of microstructure on erosion behavior of carbon steel.

4. Study dominant erosion mechanisms under different environmental conditions.
5. Study the eroded surface profile to analyze the nature of the erosion scar.

1.2 Thesis Outline

This thesis is presented in 5 chapters. The contents of this thesis are arranged in the following sequence:

Chapter 2 presents a review of background information on classification of steels and development of high strength low alloy steel (HSLA). Also, the basic theory and up-to-date literature review on the subject of slurry erosion is discussed here.

Chapter 3 presents the characterization of test specimens (physical and chemical properties) and experimental methods employed in this research.

Chapters 4 discusses the experimental results obtained in this study.

Chapter 5 summarizes the conclusion of the research, contributions and recommendations for future work.

Chapter 2

Literature Review

In this chapter, extensive literature review on high strength low alloy steel and erosion of steel is presented.

2.1 Classification of Steel

Steel Standards, which provide guidance and specification on technical delivery conditions for a range of steel products, are based on differing criteria such as manufacturing method (Bessemer steel, open-hearth steel, electric-furnace steel, crucible steel, etc.), final use (machine steel, spring steel, boiler steel, structural steel or tool steel), mechanical properties/ hardenability etc. Among all these steel standards from different countries, the majority of standards are defined in terms of the chemical composition by what the approximate content of the important elements in the steel is indicated. For an experienced engineer, the composition indicates a heat treatment that can be given to the steel and the corresponding mechanical properties obtainable.

Based upon their chemical composition and physical properties, steel grades have been developed by a number of standards organizations.

1. American Iron and Steel Institute (AISI) and Society of Automotive Engineers (SAE) steel grades
2. British Standards

3. International Organization for Standardization (ISO standard)
4. Unified numbering system (UNS)
5. ASTM International
6. Society of Automotive Engineers (SAE).
7. Japanese steel grades (JIS standard)
8. Germany steel grades (DIN standard)
9. China steel grades (GB standard)

2.1.1 Steel grades and standards

2.1.1.1 AISI and SAE Steel Grades

This steel specification represents the results of the cooperative effort of the American Iron and Steel Institute (AISI) and Society of Automotive Engineers (SAE) in a simplification program aimed at greater efficiency in meeting the steel needs of American industry.

The first digit of the four or five numerical designation indicates the type of steel. Thus 1 indicates carbon steel, 2 for nickel steel, 3 for nickel-chromium steel, etc. In the case of simple alloy steels; the second digit indicates the approximate percentage of the predominant alloying element. The last two or three digits usually indicate the mean carbon content divided by 100. Consequently, the symbol 2520 indicates a nickel steel of approximately 5 percent nickel and 0.20 percent carbon.

In addition to the numerals, AISI specifications may include a letter prefix to indicate the manufacturing process employed in producing the steel. The prefix "C" denoted open-hearth furnace or basic oxygen furnace and "E" denotes electric arc furnace steel. SAE specifications now employ the same four-digit numerical designations as the AISI specifications with the elimination of all letter prefixes. An "H" suffix can be added to any designation to denote hardenability is a major requirement. The chemical requirements are loosened, but hardness values defined for various distances on a Jominy test.

Table 2-1 SAE designation for carbon and alloy steel [15]–[17].

SAE Designation	**Type**
1xxx	Carbon steels
2xxx	Nickel steels
3xxx	Nickel-chromium steels
4xxx	Molybdenum steels
5xxx	Chromium steels
6xxx	Chromium-vanadium steels
7xxx	Tungsten steels
8xxx	Nickel-chromium-vanadium steels
9xxx	Silicon-manganese steels

Table 2-2 SAE designation for stainless steel [18]–[21].

SAE Designation	**Type**
100 Series	Austenitic chromium-nickel-manganese alloys
200 Series	Austenitic chromium-nickel-manganese alloys
300 Series	Austenitic chromium-nickel alloys
400 Series	Ferritic and martensitic chromium alloys
500 Series	Heat-resisting chromium alloys
600 Series	Martensitic precipitation hardening alloys

Table 2-3 AISI designation of steel [22].

AISI Designation	**Type**
10xx	Basic open-hearth and acid Bessemer carbon steel
11xx	Basic open-hearth and acid Bessemer carbon steel, high S, low P
12xx	Basic open-hearth carbon steels, high S, high P
13xx	Manganese 1.75
23xx	Nickel 3.50
31xx	Nickel 1.25, Chromium 0.60
40xx	Molybdenum 0.20 or 0.25
41xx	Chromium 0.50, 0.80, Molybdenum 0.20 or 0.35
44xx	Molybdenum 0.53
48xx	Nickel 3.50, Molybdenum 0.25
50xx	Chromium 0.40
61xx	Chromium 0.60, Vanadium 0.13
86xx	Nickel 0.55, Chromium 0.50, Molybdenum 0.20
92xx	Silicon 2.00
93xx	Nickel 3.25, Chromium 1.20, Molybdenum 0.12
98xx	Nickel 1.00, Chromium 0.80, Molybdenum 0.25

2.1.1.2 Standards for Steels

The International Organization for Standardization, widely known as ISO, is an international standard-setting body composed of representatives from various national standards organizations. As for example, ISO 65:1981 is for carbon steel tubes suitable for screwing applications in accordance with ISO 7-1, ISO 657 are used for hot-rolled steel sections [23]–[25]. ISO 898 is used for fasteners made of carbon steel and alloy steel, ISO 2852 is used for stainless steel clamp pipe couplings for the food-industry[26]–[28]. ISO 8501 is used for preparation of steel substrates before application of paints and related products – visual assessment of surface cleanliness and ISO 3506 is used for of corrosion-resistant stainless steel fasteners [29]–[31].

The unified numbering system (UNS) is an alloy designation system widely accepted in North America. It consists of a prefix letter and five digits designating a material composition. A prefix of S indicates stainless steel alloys, C for copper, brass, or bronze alloys, T for tool steels, etc. The UNS is managed jointly by the ASTM International and SAE International. A UNS number alone does not constitute a full material specification because it establishes no requirements for material properties, heat treatment or quality. ASTM steel standards are instrumental in classifying, evaluating and specifying the material, chemical, mechanical and metallurgical properties of the different types of steels, which are primarily used in the production of mechanical components, industrial parts and construction elements, as well as, other accessories related to them. The steels can be of the carbon, structural, stainless, ferritic, austenitic and alloy types. These steel standards are helpful in guiding metallurgical laboratories and refineries, product manufacturers and other end-users of steel and its variants in their proper processing and application procedures to ensure quality towards a safe use.

British Standards produced by BSI Group is incorporated under a Royal Charter which is formally designated as the National Standards Body (NSB) for the UK. The standards produced are titled British Standard XXXX [-P]:YYYY, where XXXX stands for the number of the standard, P stands for the number of the part of the standard (where the standard is split into multiple parts), and YYYY stands for the year in which the standard came into effect. The standard simply provides a shorthand way of claiming that certain specifications are met. And it encouraged manufacturers to adhere to a common method for such a specification. As for example, BS 5400- 5:2005 steel is the code for the design of composite bridges [22].

JIS standards developed by the Japanese Industrial Standards Committee (JISC) begin with the prefix JIS, followed by a letter G for carbon and low-alloy steels. Examples: JIS G3445 STKM11A is a low-carbon tube steel containing 0.12%C, 0.35%Si, 0.60%Mn, 0.04%P, 0.04%S; JIS G4403 SKH2 (AISI T1Grade) is a tungsten high-speed tool steel containing 0.73-0.83%C, 3.8-4.5%Cr, 0.4%Mn, 0.4%Si, 0.8-1.2%V and 17-19%W [22].

German steel specifications often start with the letters DIN and followed by an alphanumeric or a numeric code. Examples: DIN 40NiCrMo66 or 1.6565 is a Ni-Cr-Mo steel that contains 0.35-0.45%C, 0.9-1.4%Cr, 0.5-0.7%Mn, 0.2-0.3%Mo, 1.4-1.7%Ni, 0.035%S; DIN 17200 1.1149 or DIN 17200 Cm22 is a non-resulfurized carbon steel containing 0.17-0.245C, 0.3-0.6%Mn, 0.02-0.035% S and 0.4% max Si [22].

However, steels can also be classified by the broad range of carbon content, such as, low-carbon steels contain up to 0.30% C. The largest category of this class of steel is cold-rolled and annealed flat products (sheet or strip). These high-formability steels usually have a very low content of carbon, less than 0.10% C, and up to 0.4% Mn. Typical uses are in automobile body panels, tin plate, and wire products.

The carbon content of rolled steel structural plates and sections may be increased to approximately 0.30%, with higher manganese content up to 1.5%. These materials are generally used for stampings, forgings, seamless tubes, and boiler plate.

Medium-carbon steel with 0.30 to 0.60% carbon and 0.60 to 1.65% manganese is utilized for shafts, axles, gears, crankshafts, couplings and forgings. Steel in a range of 0.40 to 0.60% carbon are also used for rails, railway wheels and rail axles, since the increase of carbon content to approximately 0.5% with an accompanying increase in manganese allows medium carbon steels to be used in the quenched and tempered condition.

High-carbon steels contain 0.60 to 1.00% carbon and 0.30 to 0.90% manganese. High-carbon steel is typically used for spring materials and high-strength wires.

Experimental steels containing 1.25 to 2.0% carbon is called ultrahigh-carbon steel. These thermo-mechanically processed steels are famous for their microstructures that consist of ultrafine, equiaxed grains of spherical, discontinuous pro-eutectoid carbide particles.

2.1.2 High Strength Low Alloy Steel (HSLA)

High-strength low-alloy steels (HSLA) are type of alloy steels that provides better mechanical properties or greater resistance to erosion and corrosion than carbon steels. HSLA steels vary from other steels in the way that they are not made to meet a specific chemical composition but rather to specific mechanical properties. They have a carbon content between 0.05–0.25% to retain formability and weldability. Other alloying elements include up to 2.0% manganese and small quantities of copper, nickel, niobium, nitrogen, vanadium, chromium, molybdenum, titanium, calcium, rare-earth elements, or zirconium [32]–[37]. Copper, titanium, vanadium, and niobium are added for strengthening purposes. These elements are intended to alter the microstructure of carbon steels, which is usually a ferrite-pearlite aggregate. Addition of these alloying elements produce a very fine dispersion of alloy carbides in an almost pure ferrite matrix. High-strength steels possess highly refined grain and high cleanliness. They are characterized by low sulphur content and reduced amount of detrimental second phases such as oxides, inclusions and pearlite [38]–[40]. This eliminates the toughness-reducing effect of a pearlitic volume fraction yet maintains and increases the material strength by refining the grain size. Hence, the yield strength of ferrite increases by 50% for every halving of the mean grain diameter. Precipitation strengthening plays a minor role. Their yield strengths can be anywhere between 250–590 MPa (36,000–86,000 psi). Because of their higher strength and toughness HSLA steels usually require 25 to 30% more power to form, as compared to carbon steels. Table 2-4 shows the major alloying elements and their effect on HSLA steels.

Table 2-4 **Major HSLA steel categories** [41].

Type	Alloying Elements/Phases	Desired Properties
Weathering steel	Cu, P	Atmospheric corrosion resistance and solid solution strengthening
Microalloyed ferrite–pearlite steels	Nb, V, Ti	Precipitation strengthening and grain refinement
As-rolled pearlitic steel	C, Mn	Enhanced strength, toughness, formability and weldability
Accicular ferrite steel	Low carbon bainite	Enhanced strength, toughness, formability and weldability
Dual-phase steel	Martensite dispersed in ferritic matrix	Combination of ductility and high tensile strength
Inclusion-shape controlled steel	Ca, Zr/Ti	Ductility and through-thickness toughness

2.1.2.1 HSLA Steel Categories

High strength low alloy steels are manufactured in order to provide specific desirable combinations of properties such as toughness, formability, weldability and atmospheric corrosion resistance. Hence, HSLA steels include many grades and standards designed to meet the precise set of properties for specific operations. However it is interesting to note that, HSLA steels are not considered as alloy steel considering the presence of small amount of alloying element. Instead, they are considered as special category steels which includes special processing techniques such as controlled rolling and accelerated cooling method. Copper, silicon, nickel, chromium, and phosphorus are added to increase corrosion resistance. Zirconium, calcium, and rare-earth elements are added for sulfide-inclusion shape control, which increases formability. These are needed because most HSLA steels have directionally sensitive properties. Formability and impact strength can vary significantly when tested longitudinally and transversely to the grain. Bends that are parallel to the longitudinal grain are more likely to crack around the outer edge because it experiences tensile loads. This directional characteristic is substantially reduced in HSLA steels that have been treated for sulfide shape control and usually 20 to 30% lighter than a carbon steel with the same strength [39]. The main categories of HSLA steels are as follows:

2.1.2.2 API 5L Steels

The American Petroleum Institute (API) is a leader in the development of petroleum and petrochemical equipment. API operates standards covering topics that range from drill bits to environmental protection. Many of these standards are adopted by ISO for worldwide acceptance. In the last 30 years, large demands have been placed on the pipe manufacturer with respect to the development and the processing of materials to pipe-line. Generally, longitudinally welded large-diameter pipe-line is used for the transportation of oil and gas, because it offers the highest safety in pipeline operation and represents the most economical solution. From the point of view of pipeline economy, the pipe must favorably respond to lay in the field and permit high operating pressures for the pipelines. These requirements imply that the pipeline steel has to possess high strength and toughness and that the pipe shall have optimized geometry. Figure 2-1 presents the manufacturing flow diagram of API 5L steel pipeline.

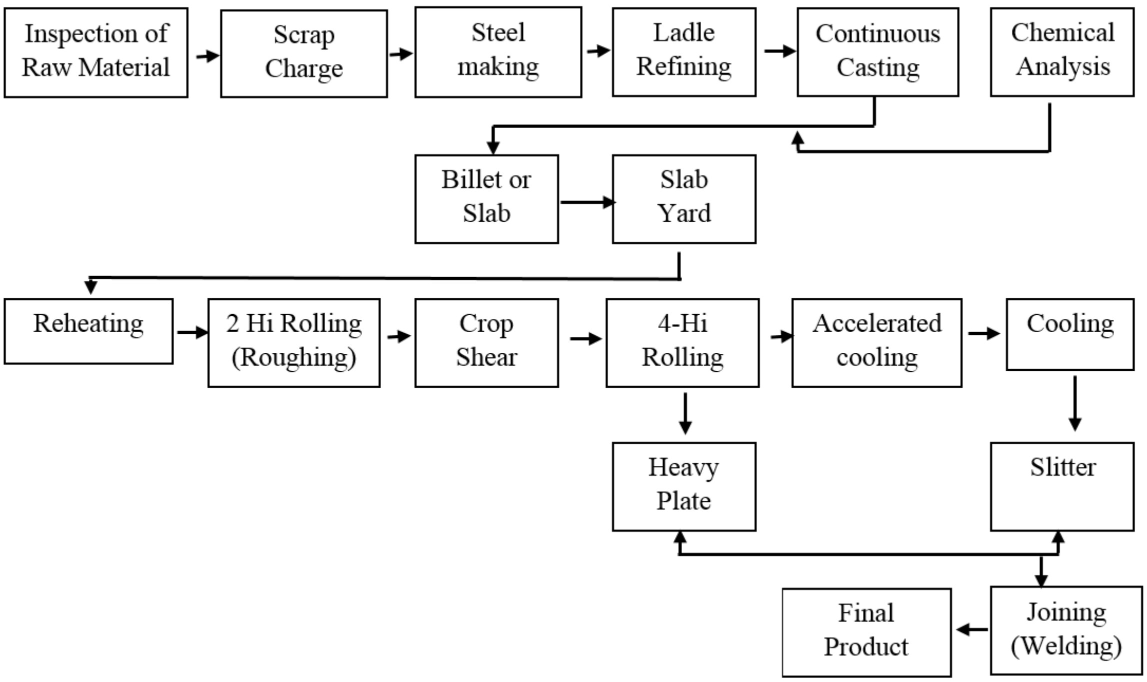

Figure 2-1 Manufacturing flow diagram of API 5L pipeline.

API 5L series is a specification providing standards for pipe suitable for use in conveying gas, water, and oil in both the oil and natural-gas industries. This specification covers seamless and welded steel line pipe. As for example, API 5L X-42 referred to pipeline steel having the yield strength of 42 Ksi produced from steels, and it is micro-alloyed with niobium, vanadium and a reduced carbon content. An improved processing method, which emerged in the eighties, consisted of thermo-mechanical rolling with subsequent accelerated cooling. It is possible to produce higher strength materials like API 5L X-80 (80 Ksi). It has a further reduced carbon content and thereby excellent field weldability by this method. Additions of molybdenum, copper and nickel enable the strength level to be raised to that of grade X-100 (100 Ksi), when the steel is processed by thermo-mechanical rolling along with modified accelerated cooling. The most important three factors govern the property of HSLA are microstructure, alloying element and thermo-mechanical treatment [42]. Chemical composition and mechanical property of API 5L series steel are given in Table 2-5.

Microstructural features such as dislocation, grain boundaries and precipitation influence the mechanical properties of steels. However, it has to be specifically designed for specific conditions [43]–[45]. The most modern line pipe steels have different and complex microstructural arrangements depending on their chemical compositions and processing routes. In low alloy steels, they develop during transformation of the austenite phase during cooling, and the development depends on the cooling rate and cooling stop temperature.

Figure 2-2 shows, how the combination of the various types of microstructures contributes to increase the mechanical strength and toughness of steels starting from normalized X-60 grade [46]. Typically, the steel contains about 0.2% carbon, 1.55% manganese, 0.12% vanadium, 0.03% niobium, and 0.02% nitrogen. The X-70 steel mentioned in the figure was thermo-mechanically processed, micro-alloyed and contains only 0.12% carbon. Thermo-mechanical rolling causes a significant reduction of the ferrite grain size. Strength and toughness properties can be improved simultaneously only by grain refinement. The loss of strength resulting from reduced pearlite contents can be offsetted by precipitation hardening and dislocation hardening. Reduction of pearlite content, grain refining, dislocation hardening and precipitation hardening contributed independently and in combination to the development of X-70 steel with improved weldability and favorable ductile-brittle transition temperatures. Furthermore, increase in strength and toughness, which led to the development of X-80 steel, can only be attained by changing the microstructure of the steel matrix from ferrite/pearlite to ferrite/bainite. In comparison with the thermo-mechanically rolled X-70 steel, the X-80 steel has further reduced carbon content, reduced grain size and increased dislocation density.

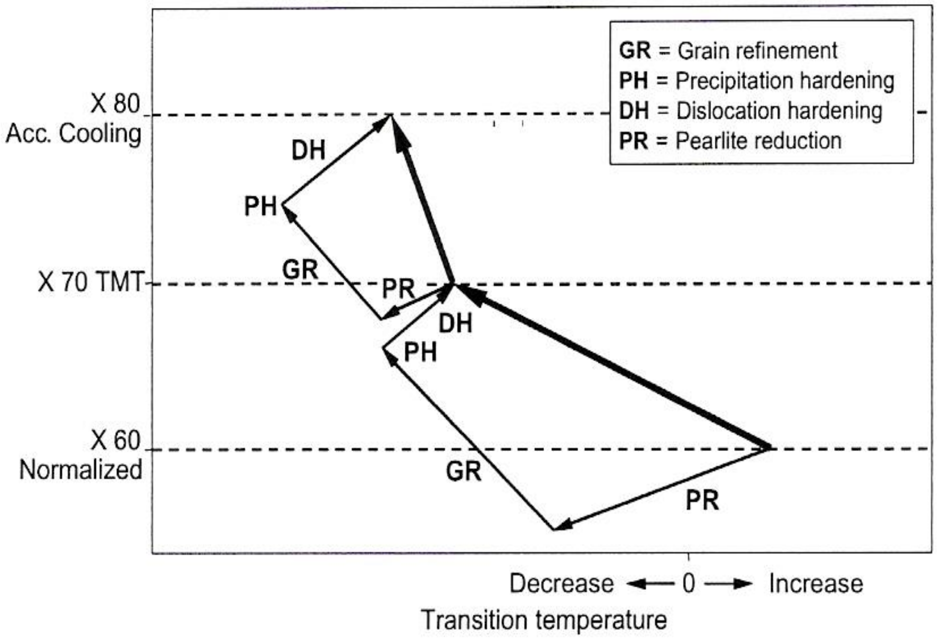

Figure 2-2 **Effect of microstructure on strength and toughness of HSLA steel** [46].

The micro-alloying of steels with the addition of small amounts of strong carbo-nitride forming elements in conjunction with controlled rolling practices has achieved a great improvement in their mechanical properties. The alloying elements improve the mechanical properties through many factors, the most important of which are [47], [48]:

1. Refinement of the ferrite grain size by the formation of a fine sub-grain structure.
2. Strain induced precipitation of the carbides and nitrides of the strong carbide and nitride forming elements.
3. Precipitation strengthening of the ferrite.

Titanium, niobium, vanadium are the most commonly used alloying elements to precipitate as carbo-nitrides and induce the grain refinement in steels. Apart from these, other elements such as molybdenum, copper, nickel and aluminum are also added to these steels to enhance mechanical properties [48].

Table 2-5 **Major effects of alloying elements in high-strength low alloy steel** [49]–[51].

Element (wt%)	**Effect and Reason for Addition**
C (0.03-0.10)	Matrix strengthening (by precipitation)
Mn (1.6-2.0)	Delays austenite decomposition during Accelerated cooling (AcC) Substitutional strengthening effect Decreases ductile to brittle transition temperature Indispensable to obtain a fine-grained lower bainite microstructure
Si (up to 0.6)	Improvement in strength (solid solution)
Nb (0.03-0.06)	Reduces temperature range in which recrystallization is possible between rolling passes Retards recrystallization and inhibit austenite grain growth (improves strength and toughness by grain refinement)
Ti (0.005-0.03)	Grain refinement by suppressing the coarsening of austenite grains (TiN formation) Strong ferrite strengthener Fixes the free Ni (prevent detrimental effect of Ni on hardenability)
Ni (0.2-1.0)	Improves the properties of low carbon steels without impairing field weldability and low temperature toughness In contrast to Mg and Mo, Ni tends to form less hardened microstructural constituents detrimental to low temperature toughness in the plate (increases fracture toughness)
V (0.03-0.08)	Leads to precipitation strengthening during the tempering treatment Strong ferrite strengthener
Mo (0.2-0.6)	Improves hardenability and thereby promotes the formation of the desired lower bainite microstructure

2.2 Erosion

Erosion is a mechanical wear process that gradually removes material by repeated deformation and cutting actions caused by solid particle impingement [52]–[54]. Due to geological formation, sand particles are common in earth crust. In oil and gas industries, several actions such as: reduction in sediment consolidation and pore pressure, increasing production rate and fluid viscosity, etc. can influence and trigger sand production from oil and natural-gas wells. According to operational experiences, it can be said that sand production is almost inevitable in oil and gas field. However, the sand exclusion system is not widespread among operators due to lower production rates. Erosion causes mechanical degradation of materials, as well as, enhance corrosion rate. Therefore, erosion has become a major concern in oil and gas production fields in recent years.

2.2.1 Solid Particle Erosion

Mass loss due to repeated impact of small solid particle on a material surface is called solid particles erosion (SPE). Erosion is a severe problem in many engineering systems such as: steam and jet turbines, pipelines and valves carrying particulate matter and fluidized bed combustion (FBC) systems. Solid particle erosion is to be expected whenever hard particles are entrained in a gas or liquid medium impinging on a solid at any significant velocity (greater than 1 m/s, or 3.3 ft/s) [55]. The metal surface undergoes surface roughening (depending on particle size and velocity; roughening ranges from polishing to severe roughening) followed by thinning of component of the system. Solid particle erosion can occur in a gaseous or liquid media where particles can be accelerated or decelerated in both cases.

2.2.2 Slurry Erosion

Material degradation process due to interaction of solid particles suspended in a liquid media is known as slurry erosion [56]. In practical cases, fluid machineries such as: hydroturbines, pipelines etc. are prone to slurry erosion followed by destruction of nozzles, vanes, impellers, buckets, seals and other parts. Materials can be removed either by cutting or sliding wear by impact of a sharp particle at a gazing angle or deformation wear by impact resulting surface fracture and subsequent removal. The common particle motion in the slurry includes sliding, rolling, and saltation. Hence, both types of eroding processes are inherent in slurry erosion to varying degrees. In oil and gas field, solid particles such as: sand particles, scale, corrosion by products, etc. is suspended in liquid while transportation occurs through the pipeline. As a result, slurry erosion has a severe impact, particularly in oil and gas industries.

2.2.3 Erosion of Steel

Erosion is a material loss process that results from repeated impact of small, solid particles. Though solid particle erosion is useful for some applications such as sandblasting and high-speed abrasive water jet cutting, it is extremely detrimental for many engineering equipment in practice such as: pipelines, steam and jet turbines, valves carrying particulate matter and fluidized bed combustion (FBC) systems, rocket engines, etc. [20], [57]–[62]. Thus, erosion has received significant attention amongst researchers in recent years [63]–[75]. Much work has been directed towards providing a fundamental understanding of this complex failure mode by suggesting models and mechanisms that account for the experimental erosion rates under specific operating conditions [76]–[84].

Low carbon steels and high strength low alloy steels (HSLA) are common in oil and gas industries. However, their poor erosion resistance dampens their performance under practical operating conditions [79], [85]–[90]. Many researchers proposed models to explain this complex degradation mode under specific environmental conditions [91]–[94]. Though, a comprehensive view of erosion modes and mechanisms under a wide range of operating conditions is lacking.

2.2.4 Factors Affecting Slurry Erosion

Slurry erosion is a time dependent process and is influenced by numerous environmental factors. Several factors have been identified by researchers that influence erosion rate, such as, impacting particle properties (density, hardness, size and shape), target material properties (hardness, ductility and microstructure) and particle flux [73], [84], [95]–[99]. Clark [100] suggested five important factors that influence the erosion rate significantly. They are: 1) slurry concentration, 2) flow speed, 3) impact angle, 4) particle size and 5) particle shape. In addition, nature of suspended liquid, flow characteristics and target material properties considerably affects the erosion rate [100]. However, studying a single variable even in a laboratory scale is a challenging task as all these factors are closely intertwined [72]. As a result, researchers have endeavored to develop a relation between erosion rate and affecting factors [101][102]. Thus, slurry erosion can be presented by following equation [81]:

$$E_w = K_1 V^{\beta} d^{\gamma} C^{\Phi} f(\alpha) \qquad \text{Equation 2-1}$$

where, E_w= erosion rate, V= slurry velocity, d= particle size, C= slurry concentration, K_1, α, β, γ and Φ are constants. These constants are closely dependent on abrasive particle and target material properties. Extensive research work has been carried out to identify the effect of these factors on slurry erosion behavior of materials [73], [83], [103]–[108].

2.2.4.1 Effect of Slurry Concentration

Slurry concentration significantly influences the erosion behavior of materials and has received the attention of many researchers [72], [79], [101]. Based on previous studies, it was established that erosion rate increases with increasing slurry concentration [63], [109]–[111]. Higher particle concentration causes more particle-material surface interactions, which leads to rapid erosion rate [110]. However, particle-particle interaction also plays a significant role at higher slurry concentration. At higher slurry concentration, abrasive particles of incoming slurry collides with each other and also with the backscattered particles (rebound effect). Such collision effectively reduces the velocity and alters the impact angle of the forthcoming particles. This phenomenon is referred as “cushioning effect” and the effect increases gradually with increasing slurry concentration [109]. Clark [72] suggested that, the particle-particle interaction is significant when slurry concentration goes above 5 wt.% for sand-water suspension. Rapid increase in collision between backscattered and forthcoming particles influences the erosion rate and mechanisms. Accordingly, it was reported that this interaction is insignificant if the concentration is less than 0.25 wt.% [71].]. Furthermore, it is reported that a protective layer may develop on the target material surface during slurry flow due to embedded particles [72]. These layers of particles protect the material surface from direct impact by incoming particles. At high slurry concentration, only a fraction of particles strike the material surface [112]. Hence, most erosion results show a non-linear upward trend with increasing slurry concentration. It was also reported that, after a critical value, increasing slurry concentration does not significantly influence the erosion behavior of materials [112], [113].

2.2.4.2 Effect of Slurry Velocity

The effect of particle velocity on erosion rate has been studied extensively by many researchers [105], [114], [115]. The velocity of an abrasive particle exerts a complex power-law relationship with erosion rate. In 1960, Finnie [116] demonstrated a strong correlation between material removal volume and the square of the velocity of abrasive particles. Several studies [117]–[123] suggested that erosion rate exhibits an empirical power law relationship with particle velocity:

$$E_1 = kV_1^n \qquad \text{Equation 2-2}$$

where, E_1 is the erosion rate, V_1 is velocity, k is a constant and η is the velocity exponent. η varies from 0.34 to 4.83 depending upon slurry condition. For dilute suspension (less than 5 wt. %) and ductile target materials, the value of η is around 2.5 [72]. The increase in kinetic energy of the abrasive particle associated with the particle velocity is primarily responsible for more erosion damage with increasing particle velocity. The normal component of impact velocity (indenting component) is mostly responsible for the depth, while the horizontal component of impact velocity is responsible for the shape of the erosion scar [68].

2.2.4.3 Effect of Flow Characteristics

During slurry erosion, abrasive particles collide with the material surface. Particle-material surface collision depends upon the following factors [124]: 1) Reynolds number, Re (describes the flow field), 2) Stokes number, St, (characterizes the abrasive particles) and 3) viscous boundary layer thickness. When slurry flows over a material surface, a combination of gravitational, frictional and drag forces act on the particle-metal contact points [125]. In addition, lubrication forces due to the viscous flow act on abrasive particles both in lateral and longitudinal directions [124]. The resultant contact force induce deformation on the surface and cause erosion. The principal force that controls the particle inertia is the viscous drag force which tends to keep the particle path along the slurry streamline [124]. However, slurry streamline direction may change from the original trajectory depending upon the Reynolds number of the liquid. On the other hand, the particle trajectory during slurry flow changes with increasing Stokes number (ratio of particle inertia to drag force) of abrasive particle [124].]. It is believed that depending upon the Reynolds number of the liquid and Stokes number of the abrasive particle, a stagnation zone may develop at the center of the eroded surface [124]. The presence of a stagnation zone on eroded profile was reported in a previous study [126]. Moreover, fluid viscosity plays a significant role on particle-material impact point. Highly viscous liquid will drag the abrasive particles laterally around the material surface and divert the direct collision trajectory [127]. Therefore, with increasing the viscosity of the carrier liquid only few particles would be able to strike the material surface due to reduction in collision efficiency and particle velocity.

2.2.4.4 Effect of Particle Distribution

Particle size, shape and hardness have a significant effect on erosion rate and mechanism and are discussed below:

2.2.4.4.1 Particle Size

The size of abrasive particles plays a significant role in the erosion prediction of materials. The erosion rate is closely related to the collision efficiency of particles. The following equation is used to explain the collision efficiency of particles [73], [97]:

$$Collision\ Efficiency = \frac{r_c}{r_0} \qquad \text{Equation 2-3}$$

where, r_c= the number of particles striking a unit area of the surface in unit time and r_0= the number of particles contained within the volume of suspension swept by the area in unit time. Previous studies [73], [97] reported that collision efficiency of abrasive particles decreases with decreasing particle size. The larger particles have high inertia, which results in the collision efficiency close to unity. On the other hand, smaller particles, having low inertia and kinetic energy, are susceptible to retardation before impact [73]. Hence, smaller particles cause less erosion damage compared to larger particles. Figure 2-3 shows the increase in erosion rate with increasing particle size [73]. Another study proposed an alternate theory to explain the particle size effect [128]. Based on that report, it can be said that heat generation due to particle material surface collision results in softening of materials by raising the surface temperature. Thus, local plasticity due to rise of the temperature forms extruded lips, which can easily be removed by further impact. Therefore, as particle size decreases, erosion rate also decreases due to sharp drop in local heating [128].

However, Mishra and Finnie reported that the size of the erodent particles has little or no effect on the erosion rate for ductile materials as long as the particle size is above 100 μm [98].

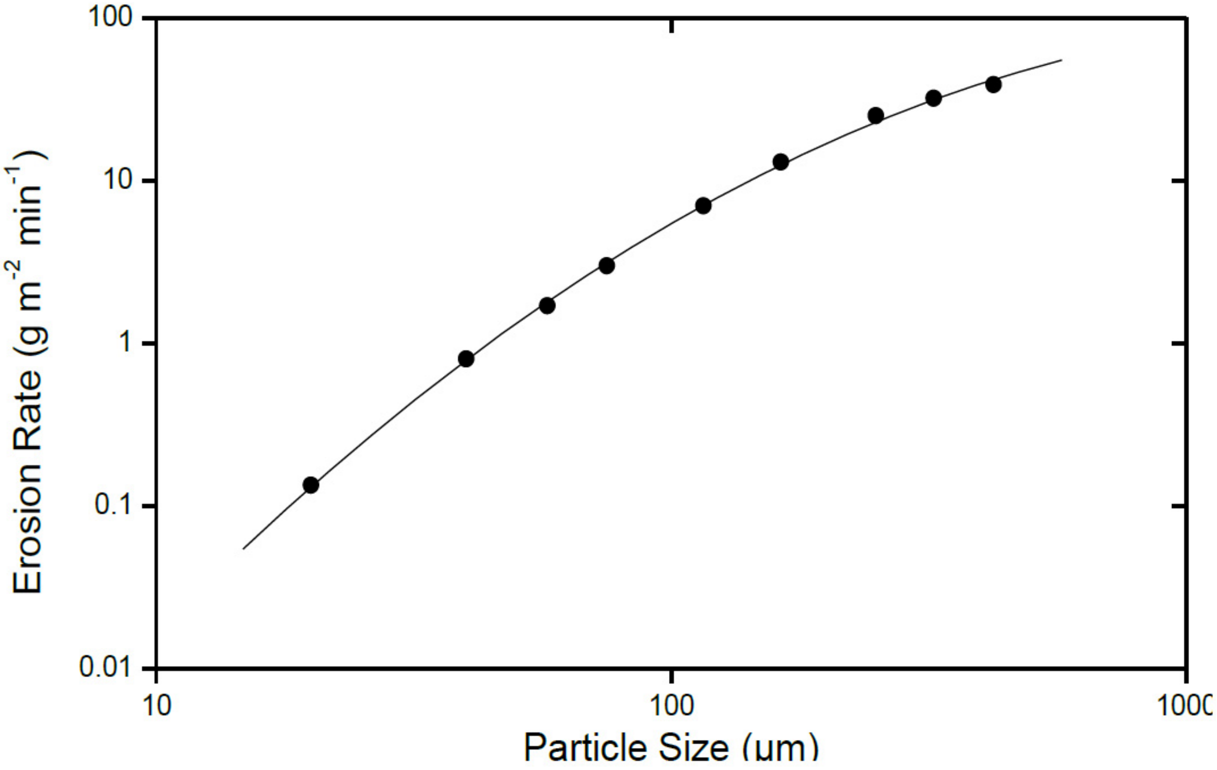

Figure 2-3 Variation of erosion rate with particle size [73].

2.2.4.4.2 Particle Shape

Another important parameter that significantly influences erosion behaviour is the erodent shape. Sharp and angular particles are most effective on cutting while spherical particles mostly cause ploughing and deformation damage. When sharp abrasive particles strike a material surface, they create deep craters and vulnerable lips. On the other hand, shallow craters are created due to impact between rounded particles and target material surface [129]. It is well established that sharp abrasive particles cause more material removal than spherical particles [130]–[138]. However, determination of particle angularity is a challenging task. Stachowiak [139] proposed

Spike Parameter (S.P) method to define particle angularity where particle boundary is defined by a set of triangles. Larger and sharper size of the tringle causes more erosion damage on the target material surface. Desale et al. [81] and Roy et al. [140] also studied the effect of particle angularity and reached similar conclusion. Figure 2-4 illustrates the Spike Parameter to define particle angularity. Depending upon the relative impact position different cutting processes are observed on the material surface due to impact by angular sharp particles [129]. On the other hand, when round shaped particle strikes the surface, erosion resistance of target material increases with increasing material hardness. However, erosion resistance of target material is independent of hardness and depends on material microstructure and the operating erosion mechanisms during the process in case of impact by sharp angular particles [99], [141]–[143].

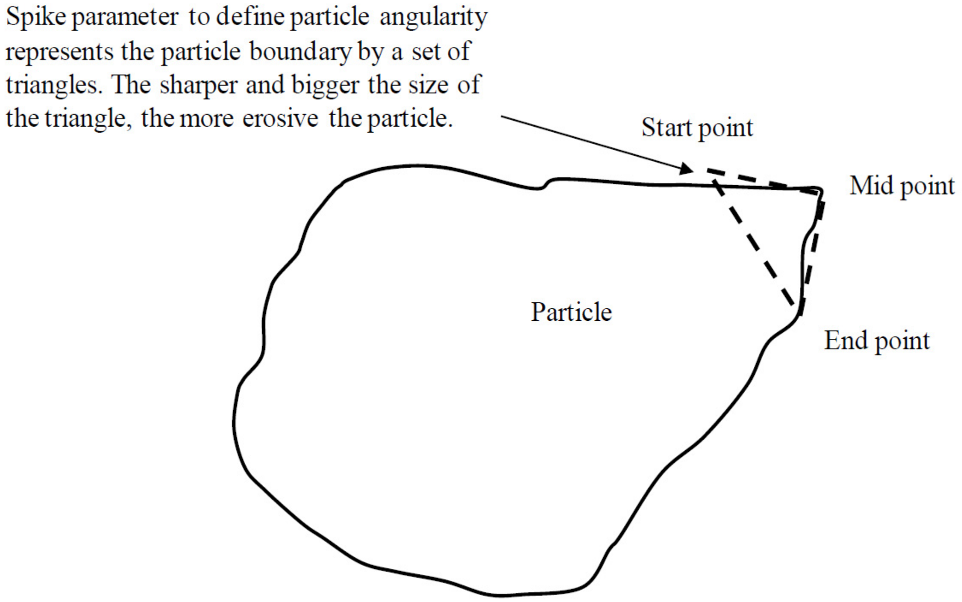

Figure 2-4 **Schematic illustration of the Spike Parameter (S.P) to define particle angularity** [139].

2.2.4.4.3 Particle Hardness

The erosion rate of materials is sensitive to the ratio of the abrasive particle hardness (H_a) to the target material hardness (H_s). The abrasive particle must be harder than the target surface for erosion to occur [144]. Previous study reported a drastic drop in erosion rate when abrasive particle hardness is lower than the target material hardness [145]. Accordingly, erosion rate becomes significant when the abrasive particle hardness is at least an order of magnitude higher than the base material [98]. Therefore, a minimum ratio of the relative hardness of the abrasive particle to the material surface is required for erosion damage. Experimental observation showed that, if H_a/H_s exceeds the value 1.2, then plastic flow in target material will occur by collision with abrasive particles independent of their shape [129]. Figure 2-5 illustrates the effect of hardness on particle-material contact zone during impact. This phenomenon also explains why the heat treatment of steels appears to have almost no effect on their erosion resistance [146]. The reason behind that is if the abrasive particle hardness is considerably higher than the base material, a relatively small increase in material hardness, due to heat treatment, would not have significant effect on erosion behavior.

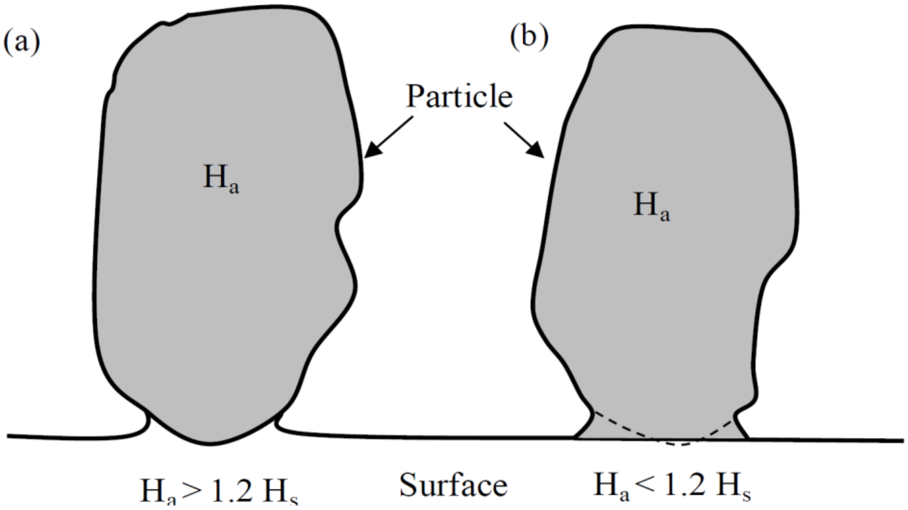

Figure 2-5 **Schematic diagram showing the effect of H_a/H_s on particle-material contact zone, a) particle will indent the surface when $H_a > 1.2\ H_s$ and b) plastic flow will occur in the particle when $H_a < 1.2\ H_s$ [129].**

2.2.5 Erosion Mechanism

Erosion mechanism is a complex phenomenon that is influenced by many environmental factors. Different degradation mechanisms are found acting independently and sometimes simultaneously depending upon the operating conditions, particle distribution and particle trajectory. Erosion mechanisms of steel can be divided into two main categories: ductile and brittle. Studying the erosion behavior of the materials under different impact angle provides clear evidence on these two types of mechanisms. It is reported that ductile materials show maximum erosion rate at low impact angle (15°-30°) while brittle materials are subjected to maximum erosion rate at normal impact angle (90°).

During erosion, an abrasive particle has to impact the material surface with a critical velocity [133] and specific impacting orientation in order to cause deformation [147], [148]. However, in most cases, particle impact forms a crater and vulnerable lips at the edge of the crater. Such lips are prone to be detached upon further impact [149], [150]. Normal impact of abrasive particles causes formation of deformed platelets on the material surface. These deformed platelets are then eventually removed by fracture and cause erosion [150], [151]. Levy and Hickey [63] observed different geometrical shapes of deformed platelets and concluded that platelets formed due to slurry erosion have different geometries compared to platelets formed in solid particle erosion.

At higher slurry concentration, "Cushioning Effect" plays a significant role on erosion of steels [109]. The forthcoming abrasive particles collide with back scattered particles, and these collisions alter the velocity and impact angle of the forthcoming particles. When abrasive particles impact the material surface at an acute angle, the kinetic energy of the particles can be divided into two components [110]:

1. The horizontal component which favors cutting mechanism.
2. The perpendicular component which promotes severe plastic deformation.

Depending upon the impingement angle and kinetic energy of abrasive particles, several erosion mechanisms such as: ploughing and microcutting are observed. Ploughing was reported by Santa et al. [152] and Goyal et al. [153] where Shivamurthy et al. [154] and Das et al. [155] reported the presence of microcutting as dominant erosion mechanism. Common types of erosion mechanisms are summarized in Table 2-6.

Table 2-6 Common types of erosion mechanisms [110], [153]–[155].

Types of Erosion	**Environmental Conditions**	**Damage Type**
Plastic deformation and fracture	Impingement angle = 90°	Repeated impacts of erodent particles at normal incidence creates deformed platelets and cause fracture of a material from the impact site.
Delamination	Impingement angle = 90°	Formation of sub-surface cracks parallel to the eroded surface, extension of these cracks to the surface and formation of plate-like debris.
Microcutting	Impingement angle < 90°	Angular impact by abrasive particles with critical kinetic energy cut materials from the surface.
Ploughing	Impingement angle < 90°	Displacing materials to the front and sides of the particle. Repeated impacts on the neighboring site cause removal of highly strained materials from the terminal lip of the crater.

2.2.6 Erosion Models

Erosion behavior of a material depends on the operating parameters and conditions. In order to quantify the erosion damage researchers proposed several erosion predictive models. Meng and Ludema [156] studied proposed erosion models and chose 28 models based on a list criterion. Selected erosion models and their underlying mechanisms are discussed in this section.

2.2.6.1 Finnie's Erosion Model

Finnie [132], [146] first developed an erosion model which states that mechanical wear due to erosion is dependent on the particle motion entrained in the flowing fluid, as well as, the interaction between the particles and the surface. This model was developed by solving the equations of motion of the particles and assumed that the entrained particles obey the laws of motion. In addition, this model states that the volume of the material removed during erosion is dependent on the swept area by the erodent. The simple model is described by the following equations [132], [146]:

$$V_m = \left(\frac{f_c}{2k_4}\right)\frac{D_t V_1^2}{0.9272 H_s}\left(sin2\alpha - \frac{8}{k_4}sin^2\alpha\right); \qquad tan\alpha \le \frac{k_4}{8}$$

Equation 2-4

$$V_m = \left(\frac{f_c}{16}\right)\frac{D_t V_1^2}{0.9272 H_s}(cos^2\alpha); \qquad tan\alpha \ge \frac{k_4}{8}$$

where, fc is the proportion of particles impacting the surface and cutting in an idealized manner. V_1 is the erodent particle impact velocity, D_t and H_s are the density and static hardness of target material respectively and α is the particle impact angle. In Equation 2-4, k_4 is the ratio of vertical to horizontal force components on the particle and is assumed to be constant.

2.2.6.2 Bitter's Erosion Model

Bitter [68], [157] proposed two types of erosion mechanisms in his model. The first one is deformation mechanism, and the rest is cutting mechanism. This model was formulated based on the mass, velocity and impact angle of the abrasive particles combined with the mechanical properties of the target materials. Also, energy distribution during collision between abrasive particle and target material is described by energy balance. It is interesting to note that, Finnie related material strength to the absorbed energy during cutting while Biter's model correlated energy absorbed to the integrated product of the stress-strain curve. The following equations are used to describe Bitter's erosion model [68], [157]:

$$W_d = \frac{1}{2}\frac{m(sin \propto - U_p)^2}{\gamma}$$

$$W_{c1} = 2mC_1\left(\frac{v\ sin \propto - U_p^2}{\sqrt{vsin} \propto}\right)[v\ cos \propto - C_1\frac{v\ sin \propto - U_p^2}{\sqrt{vsin} \propto} - \rho 1] \tag{Equation 2-5}$$

$$W_{c2} = \frac{1}{2}[\frac{mv^2cos^2 \propto - k_1(sin \propto - U_p)^{\frac{3}{2}}}{\rho 1}]$$

Where, W_d = total deformation wear, C_1 = is a constant that depends on density and elastic load unit, W_{c1} = cutting wear unit, W_{c2} = cutting wear unit loss, α = impact angle, ρ= energy needed to scratch out a unit volume from the surface, U_p = maximum particle velocity at which collision is purely elastic, γ = deformation wear factor and k_1 = constant based on mechanical properties.

2.2.6.3 Hutchings' Erosion Model

The Hutchings erosion model proposed that the erosion for ductile materials at normal impact by spherical particles occurs by the formation and subsequent detachment of platelets of metal lying parallel to the eroded surface [129]. This model assumed that at normal impact by spherical particles forms a plastically deformed region around the dentation. After several cycles of indentation, this region becomes work hardened and eventually detached from the material surface as wear debris [131]. The total work done by the abrasive particle as it strikes the material surface is equal to its initial kinetic energy. The final expression for dimensionless erosion rate (E) was expressed as,

$$E = 0.033\frac{\alpha_r D_t D_p^{\frac{1}{2}} V_1^3}{\varepsilon_c^2 H_d^{\frac{3}{2}}} \qquad \text{Equation 2-6}$$

where, H_d and D_t are the dynamic hardness and density of the target material respectively, D_p is the density of erodent particles, and V_1 is the erodent particle velocity. The term a_r/ε_c^2 cannot be measured independently. Hutchings assumed the value of a_r/ε_c^2 to be equal to 0.7.

2.2.6.4 Hashish's Erosion Model

The erosion model proposed by Hasish [158] addressed the deficiencies in Finnie's model. Higher velocity exponents (η>2), shape and density of abrasive particles were taken in to account in this model. A characteristic velocity C_k is introduced in this model that combines material flow stress, particle density and shape factor. The model can be described by following equation [158]:

$$E = \frac{14}{\pi}\frac{\rho_m}{\rho_p}\left(\frac{v\,sin \propto - v_c}{C_k}\right)^{2.5} cot \propto \qquad \text{Equation 2-7}$$

where, E is the ratio of mass of the materials removed to the mass of the abrasive particle, C_k is the modified characteristic velocity that combines the characteristics of the abrasive particles and target materials.

2.2.7 API Guidelines for Erosion in Oilfield

Erosion causes major damages in oil transportation pipelines due to ageing of oilfield assets. Instead of using sand screen, oilfield pipeline operators tend to redesign the facilities in order to avoid production rate drop [159], [160]. However, most erosion models are applicable for specific erosion condition [70]. In addition, erosion rate prediction of these models are not accurate enough in terms of practical field operations. Hence operators are provided with guidelines to avoid major failure without dropping production rate. One of the popular guidelines is API-RP-14E. According to this guideline, the highest allowable velocity in the pipeline is given by following expression:

$$V_c = \frac{C}{\sqrt{P}} \qquad \text{Equation 2-8}$$

where, Vc = maximum allowable erosion velocity, ρ = density and C = an empirical constant. However, this equation is not ideal for the situation where erosion and corrosion both are involved. Salama [113] proposed the following equation for the fluid where erosion due to the sand is predominant:

$$V = \frac{D\sqrt{Pm}}{20\sqrt{w}} \qquad \text{Equation 2-9}$$

where, W is the sand flow rate and D is the internal diameter of the pipe. The modified expression for multiphase flow is as follows [113]:

$$ER = \frac{1}{S_m}\frac{WV_m^2 d_p}{d^2 \rho_m} \qquad \text{Equation 2-10}$$

where ER is the erosion penetration rate, W is the sand production rate, Vm is the fluid mixture velocity, dp is the sand size, D is the pipe diameter, ρ_m is the fluid mixture density and *Sm* is the geometry-dependent constant. Shirazi et al. [161] also proposed a model which is associated with a wider range of operating conditions. The model can be illustrated by the following equation:

$$h = F_M F_S F_P F_{\frac{r}{D}} \frac{W V_L^{1.73}}{(\frac{D}{D_0})^2} \qquad \text{Equation 2-11}$$

where h is the penetration rate, F_M is the empirical constant that accounts for material hardness, F_S is the empirical sand sharpness factor, F_p is the penetration factor for steel (based on 1″ pipe diameter), $F_{r/D}$ is the penetration factor for elbow radius, W is the sand production rate, V_L is the characteristic particle impact velocity, D is the pipe diameter and D_0 is the reference of 1 inch pipe diameter.

Chapter 3

Experimental Details

A set of slurry erosion tests have been carried out to study the erosion behavior of pipeline steels using a wet erosion test rig. This chapter presents the preparation, materials characterization and detailed layout of the experimental methods and operating conditions employed in this study.

3.1 Materials Characterization

Test specimens were characterized to determine the mechanical and chemical properties. ICP, SEM and optical microscopy were performed to characterize the materials. After the erosion test, the eroded surface was scanned using a high resolution 3D profilometer to study the eroded profile.

3.1.1 Physical Properties

In this study, AISI 1018, AISI 1080, API X80, API X100 and API X120 pipes and bars were cut to prepare test specimens (15.8± 0.03 mm diameter and 6.1 ± 0.02 mm thick). The mechanical properties of these steels are summarized in Table 3-1. The hardness of AISI 1080 steel was found much higher than AISI 1018 as expected due to the higher amount of pearlite in the microstructure. Whereas, Young's moduli of all test specimens was found almost similar as Young's moduli is a structure insensitive property and its value mainly determined by the atomic bond strength of iron.

Table 3-1 Physical properties of AISI 1018, AISI 1080, API X80, X100 and API X120 steels.

Properties	AISI 1018	AISI 1080	API X42	API X70	API X80	API X100	API X120
Yield strength (MPa)	310	585	290	482	555	690	883
Elongation	20%	12%	23%	17%	16%	15.2%	14.3%
Modulus of elasticity (GPa)	205	200	210	203	210	210	210
Density (g cm^{-3})	7.87	7.87	7.87	7.87	7.87	7.87	7.87
Vickers hardness (GPa)	1.285	3.03	1.344	1.814	2.43	2.50	2.97
Average grain size (μm)	10±2	12±2	8±2	5±2	8±2	5±2	4±2
%Pearlite	20	100	19	5	5	5	4

Alpha aluminum oxide (Al_2O_3) powder was used as abrasive. The physical properties of abrasive particles are given in Table 3-2. The particle size distribution of abrasive particles was measured using Malvern Mastersizer 3000 laser diffraction particle size analyzer (Figure 3-1). The average particle size is found to be approximately 57±2 μm. The SEM micrograph of abrasive particles is presented in Figure 3-2(a). And Figure 3-2(b) is a magnified image of Figure 3-2(a). Figure 3-2(a) and Figure 3-2(b) showed the presence of sharp and angular abrasive particles, which are primarily responsible for the erosion degradation.

Table 3-2 Physical properties and chemical composition of aluminum oxide.

Physical properties	
Crystal phase	Alpha
Specific gravity	3.95 g cm^{-3}
Particle shape	Angular
Vickers hardness	27.13 GPa
Particle size	57±2 µm

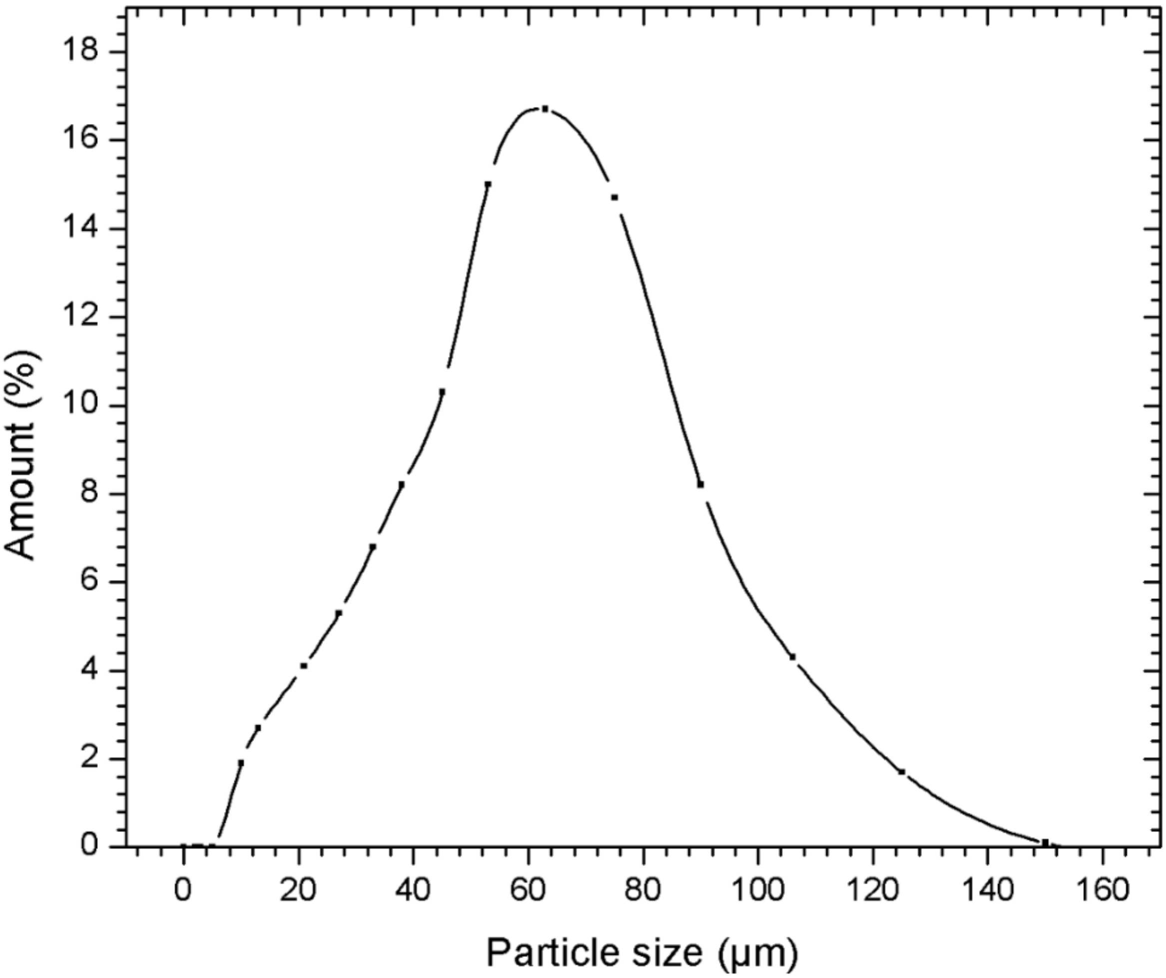

Figure 3-1 Particle size distribution of alumina abrasive having an average particle size of 57 ± 2 µm.

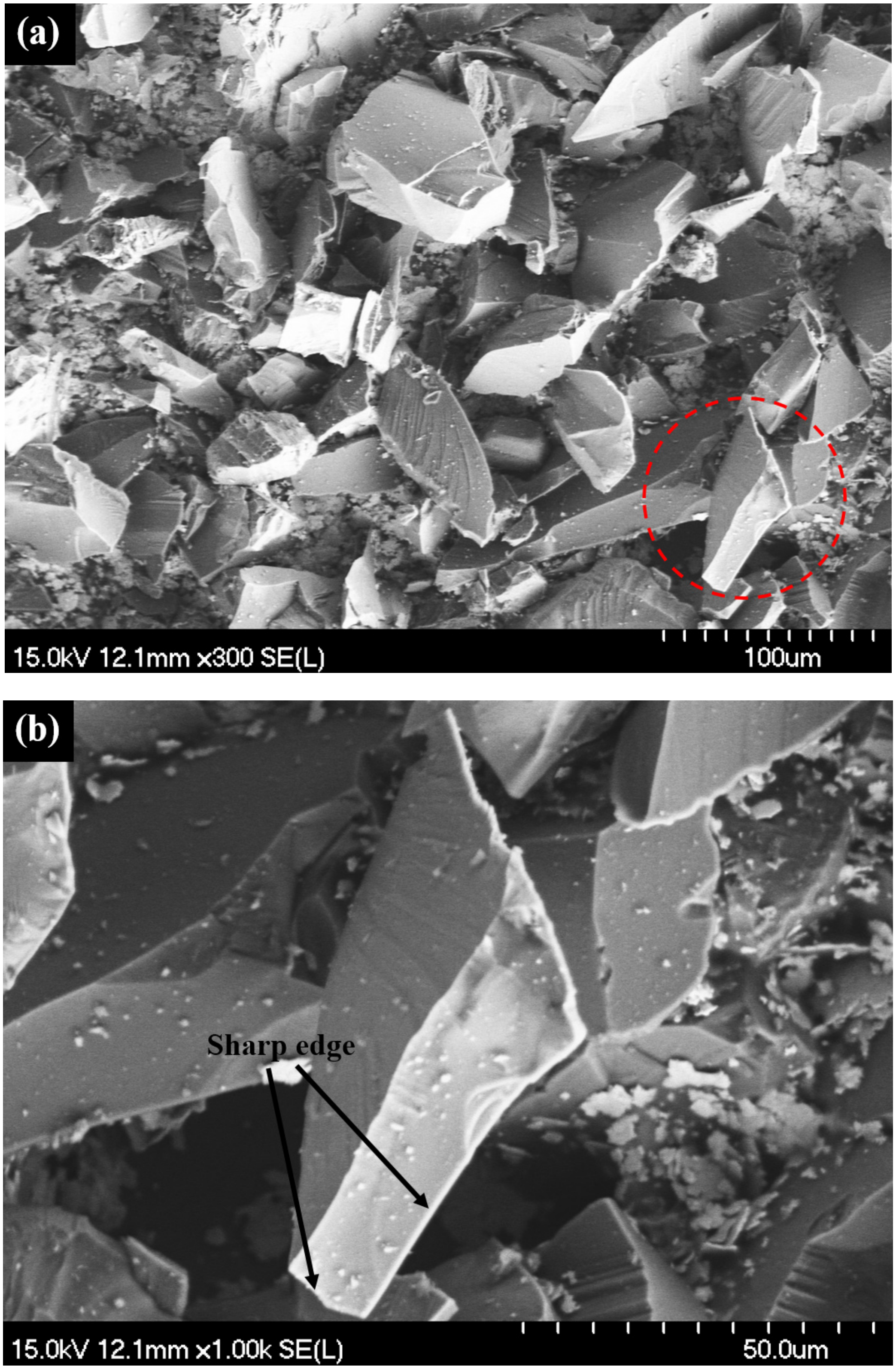

Figure 3-2 SEM micrograph of the alumina abrasive showing irregular shaped particles.

3.1.2 Chemical Properties

The chemical compositions of AISI 1018, AISI 1080, API X80, API X100 and API X120 steels were measured by using Inductively Coupled Plasma Mass Spectrometry (ICP). The results are summarized in Table 3-3. X-ray diffraction (XRD) experiments were carried out using a high-speed Bruker D8 advance system employing Cu-Kα1 radiation having a wave length (λ) of 1.54 Å, tube voltage of 40 kV and tube current of 40 mA. Figure 3-3 shows the XRD pattern of API X42 steel as a representative example. XRD peaks were matched to those in the Powder Diffraction Files (PDF) and identified as carbon steel peaks having a BCC crystal structure.

Table 3-3 Chemical composition of carbon and pipeline steels.

Elements	AISI 1018	AISI 1080	API X42	API X70	API X80	API X100	API X120
C	0.182	0.814	0.169	0.061	0.149	0.103	0.141
Si	0.095	0.120	0.067	0.150	0.125	0.151	0.132
Mn	0.754	0.598	0.372	1.223	0.555	1.221	0.561
Cr	0.181	0.122	0.027	0.018	0.060	0.070	0.070
P	0.040	0.040	0.040	0.010	0.010	0.010	0.010
Cu	0.186	0.230	0.008	0.008	0.020	0.009	0.019
Ti	0.008	0.001	0.002	0.015	0.004	0.018	0.001
V	0.001	0.021	0.001	0.028	0.030	0.036	0.031
S	0.021	0.014	0.004	0.002	0.001	0.001	0.001
Fe	balance	balance	balance	balance	balance	balance	balance

The chemical composition of alumina abrasive is provided in Table 3-4.

Table 3-4 Chemical composition of aluminum oxide.

Chemical composition					
AlO_2	TiO_2	SiO_2	Fe	MgO	Alkali
99.5	0.099	0.05	0.08	0.02	0.30

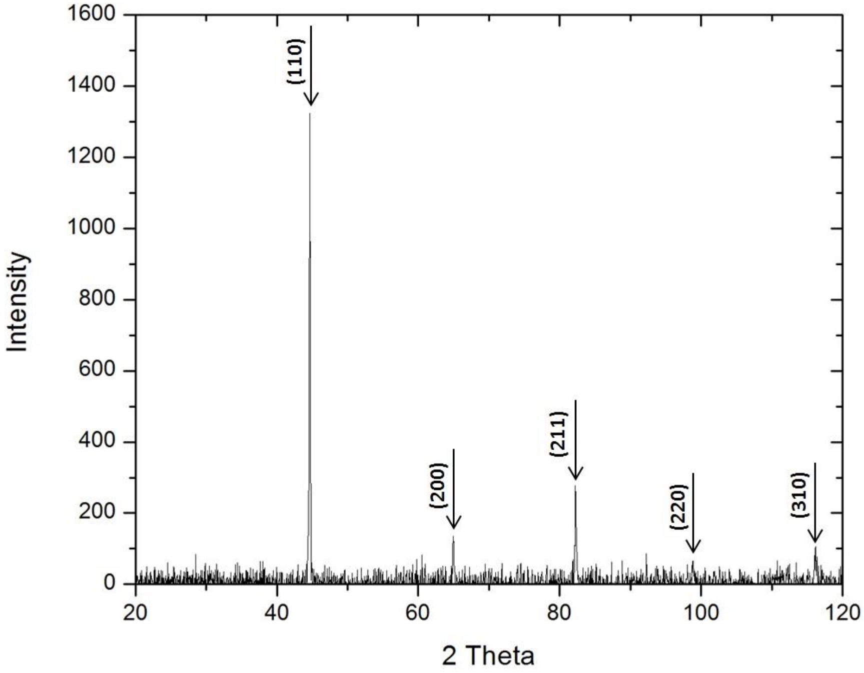

Figure 3-3 **XRD pattern of API X42 steel identified as carbon steel peaks having a BCC crystal structure.**

3.1.3 Microstructural Properties

In this study, steel coupons were used as test specimens. Specimens were first ground using 240, 320, 400 and 600 grit SiC abrasive papers. The samples were then polished using 1, 0.3 and 0.05 µm gamma alumina suspension. After that, specimens were cleaned with acetone in an ultrasonic bath. Cleaned specimens were then etched using a 5% Nital solution to examine the microstructure. Figure 3-4 (a), (b), (c), (d), (e), (f) and (g) represent the optical micrographs of AISI 1018, AISI 1080, API X42, API X70, API X80, API X100 and API X120 steels respectively. AISI 1018, API X42 and API X70 steel microstructures consist of ferrite and pearlite (Figure 3-4 (a), Figure 3-4 (c) and Figure 3-4 (d)). Whereas, AISI 1080 steel microstructure shows presence of 100% pearlite (Figure 3-4 (b)). However, the microstructure of API X80 consist of deformed ferrite, bainite, and pearlite (Figure 3-4 (e)). On the other hand, the microstructure of API X100 steel comprised of very fine bainite and ferrite having lath-like and granular type morphology (Figure 3-4(f)). Matrix microstructure of API X120 is composed of bainitic ferrite and acicular ferrite [162]. The addition of molybdenum, copper and nickel increases the temperature of the maximum rate of pearlite transformation and decreases the temperature of the maximum rate of bainite transformation and thus promotes the formation of the desired lower bainite microstructure [48]. A similar type of microstructure for API X100 was previously observed by others [163]. Microstructural constituents and average grain sizes for these steels are shown in Table 3-1.

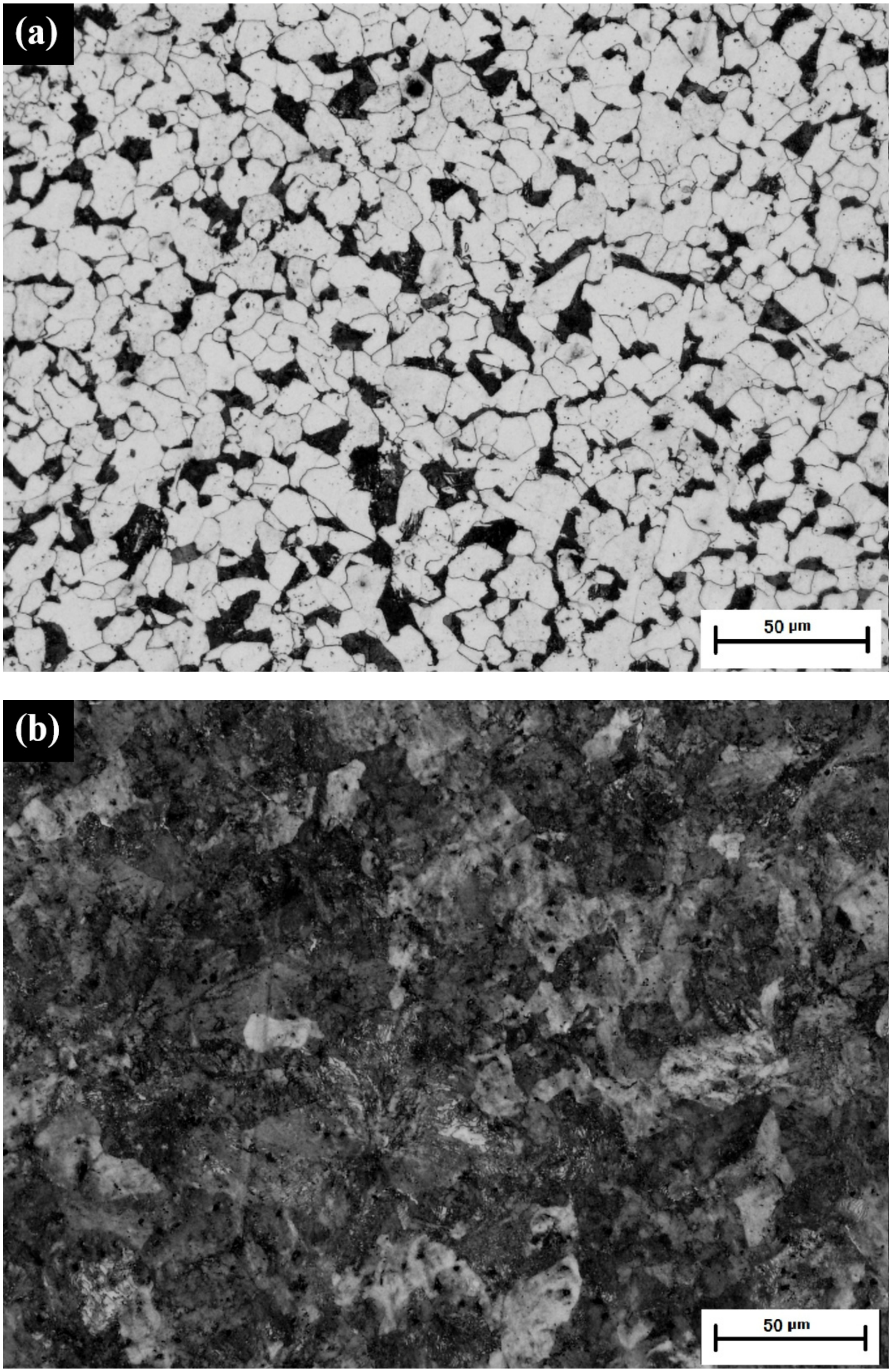

Figure 3-4 Optical micrograph of (a) AISI 1018 and (b) AISI 1080 steels.

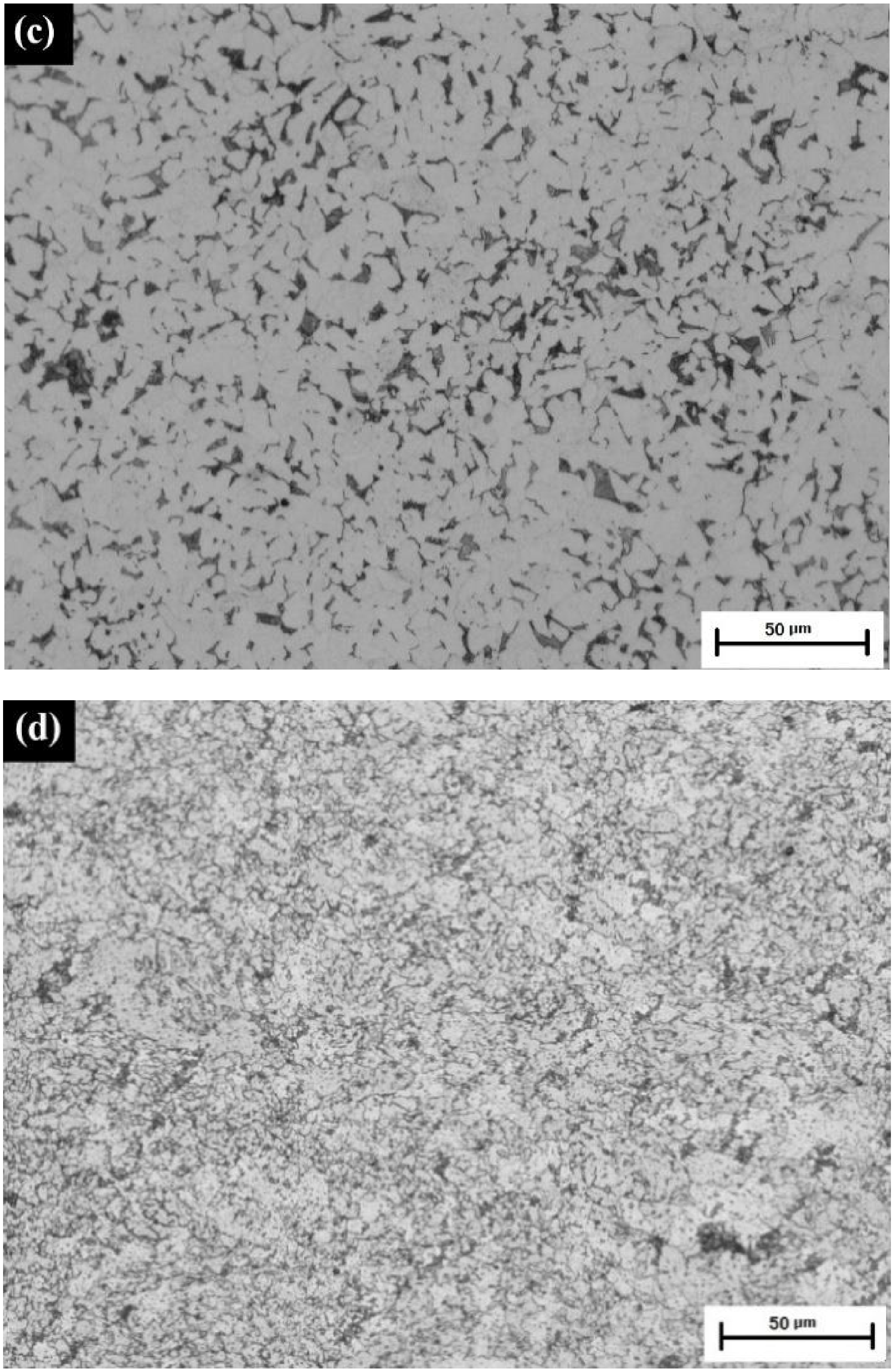

Figure 3-4 Optical micrograph of (c) API X42 and (d) API X70 steels.

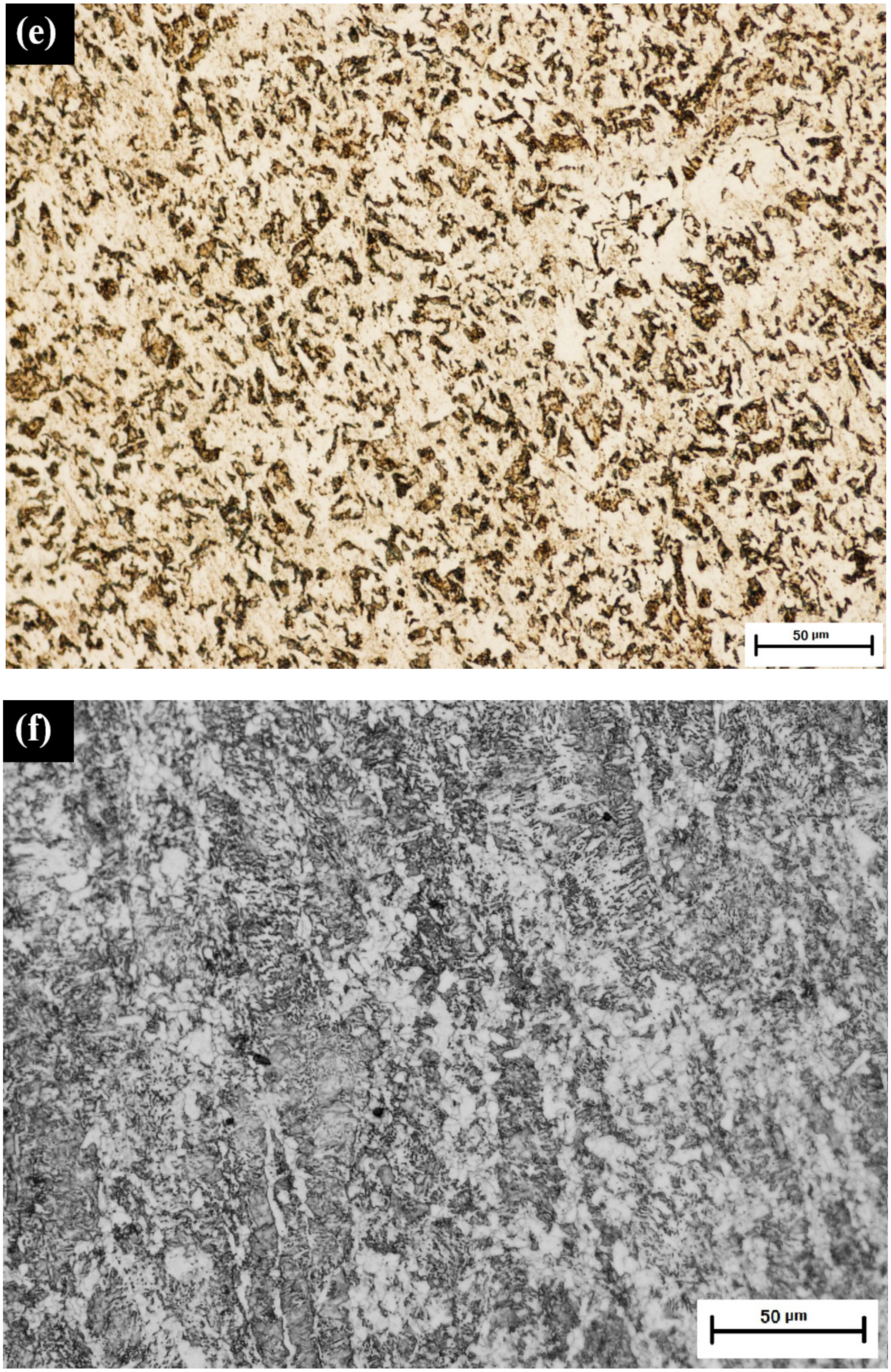

Figure 3-4 Optical micrograph of (e) API X80 and (f) API X100 steels.

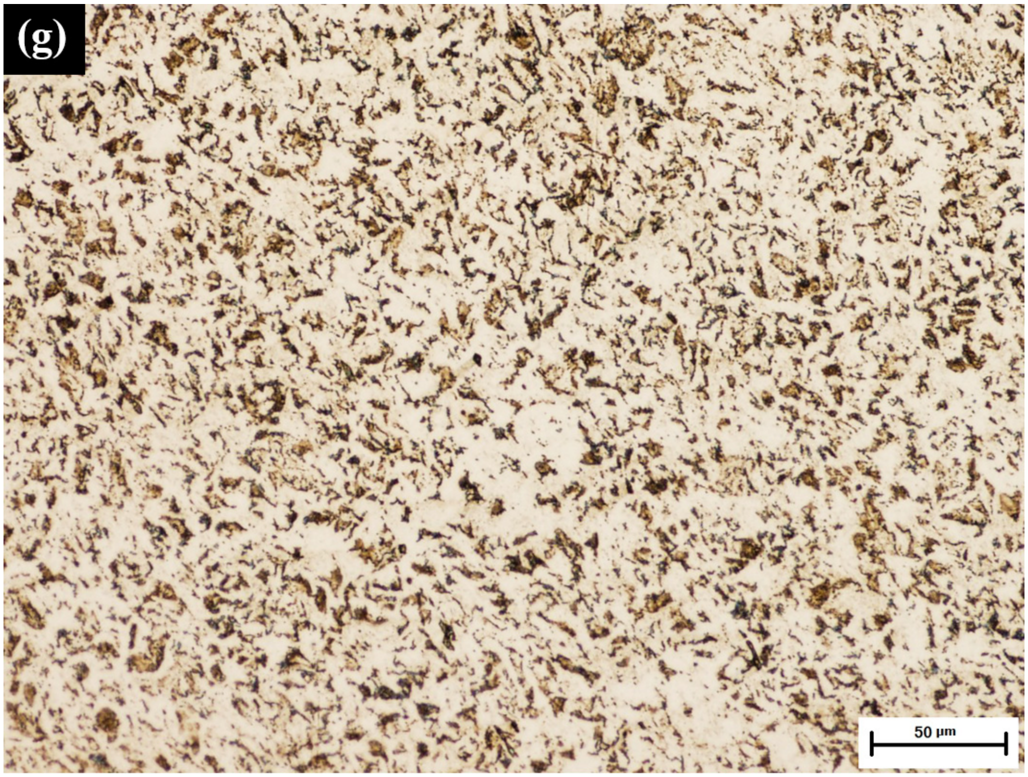

Figure 3-4 Optical micrograph of (g) API X120 steel.

3.2 Experimental Setup

The detailed information about experimental setup and operating conditions employed in this study is discussed in this section.

3.2.1 Slurry Erosion Tester

A jet type rig, capable of eroding materials under well controlled exposure condition, was used in this research work. The schematic diagram of the slurry erosion tester is illustrated in Figure 3-5. The test rig is composed of a slurry reservoir, agitator, slurry flow meter, nozzle, submerged specimen holder and a pump. First water and abrasive particles were poured into the slurry reservoir. A mechanical agitator is installed on the test rig to achieve a homogeneous slurry. Continuous agitation prevents slurry mixture from settling at the bottom. The slurry flows from slurry chamber to the nozzle by using a mechanical pump. In order to achieve a uniform particle distribution in the stream a nozzle (inner diameter: 2.3 mm, length: 33 mm) having a length to diameter ratio of 14:1 was used. Test specimen was placed in a movable specimen holder in order to control the standoff distance. The slurry discharged from the nozzle strikes the specimen surface and cause erosion. The isometric view of specimen holder and nozzle is shown in Figure 3-6.

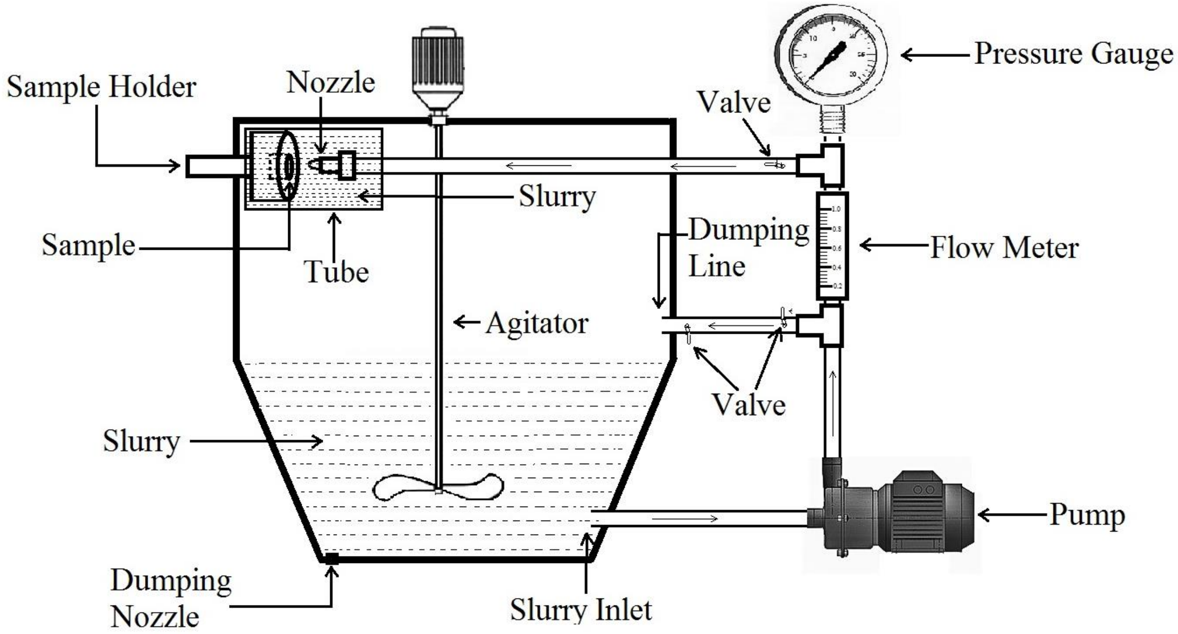

Figure 3-5 **Schematic diagram of experimental setup for slurry erosion tester.**

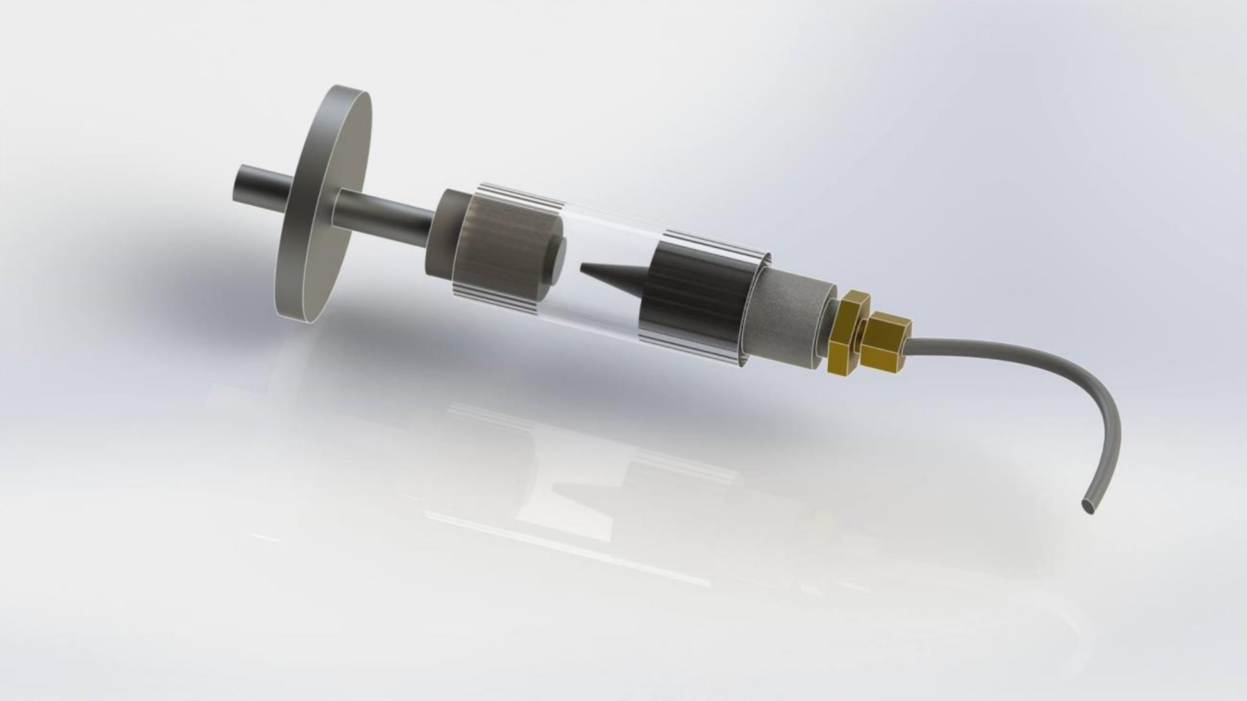

Figure 3-6 **Isometric view of erosion sample holder and nozzle (SolidWorks).**

Operating conditions for erosion tests are given in Table 3-5. A wide range of slurry velocity (0.20-12 $m\ s^{-1}$) and concentration (0-5 g L^{-1}) was employed in the current study in order to assess the effect of slurry velocity and concentration on erosion rate and dominant erosion mechanisms. Specimens were weighed using a digital balance (with an accuracy of 1×10^{-5} g) before and after each erosion test. The eroded specimens were cross-sectioned in a longitudinal direction in order to investigate the sub-surface of the erosion scars. Specimens were cut using a Buehler® isomet 1000 slow precision saw using a diamond wafering blade (15.2 cm diameter × 0.5 cm thick). Isomet 1000 precision saw has an automatic cut-off switch, a counter balanced sliding load weight system, a built-in metric digital micrometer cross-feed for sample location and a removable coolant tray with built-in dressing device, in order to avoid excessive heating. Erosion rate was calculated using the following equation [164],

$$E_0 = \left[\frac{\Delta W}{A\ d\ t}\right] K_1 \qquad \text{Equation 3-1}$$

Where, ΔW is the weight loss (g) of the specimen, A is the surface area (mm^2), d is the density (g cm^{-3}), t is test duration (s) and K_1 is a constant (1 × 10^6 µm cm^{-1}).

To be able to compare erosion rates performed using different particle velocities, the erosion rate needs to be normalized with respect to the slurry flow rate for a given slurry velocity. That is, the normalized erosion (E) rate is calculated by dividing erosion rate (mg s^{-1}) by the abrasive particle flow rate (mg s^{-1}) using the following equation [165]:

$$\text{Normalized erosion rate}, E = \frac{\text{Erosion rate (mg s}^{-1})}{\text{Particle flow rate (mg s}^{-1})} \qquad \text{Equation 3-2}$$

Table 3-5 Operating conditions for slurry erosion tests.

Parameters	Operating Conditions
Nozzle diameter	2.3 mm
Standoff distance	3 mm
Test duration	30, 180, 420 and 600 s
Impact angle	90°
Slurry concentration	0, 10, 20, 30, 40, 50 g L^{-1}
Slurry velocity	0.20, 0.29, 0.36, 0.43 and 12 m s^{-1}

Chapter 4

Results and Discussion

This chapter focuses on some of the complexities associated with slurry erosion of pipeline steels. The erosion behavior of steel depends upon the surrounding factors. The erosion rate and erosion mechanisms rapidly alter depending upon these variables. In this chapter, an attempt has been made to evaluate the effect of slurry velocity and slurry concentration on the erosion rate and erosion mechanisms. Dominant erosion mechanisms for different velocity and concentrations are identified and discussed in detail.

4.1 Erosion Behavior of Steels

In order to measure the erosion rate, each specimen was weighed before and after slurry exposure for 30, 180, 420 and 600 s for different slurry velocities and concentrations. Figure 4-1 represents the trend of the increase in weight loss of steel specimens with increasing test duration for AISI 1018, AISI 1080, API X42 and API X70 steel samples at 1% slurry concentration for different slurry velocities. Figure 4-2 shows typical trends of increasing weight loss with exposure time for 3 wt.% slurry concentration. It is evident that weight loss increases with increasing test duration. Also no significant change in slope was observed in the plots for all steels. As wear mechanism transition is associated with change in wear rate, these plots indicate that no wear transition has taken place throughout test durations. That is, the same dominant erosion mechanisms operates throughout the entire test period. Furthermore, it is also observed that in general weight loss of the steel increases with increasing slurry concentration. Different erosion mechanisms may operate on the steels surfaces depending upon the velocity and concentration which are discussed later in section (4.2 Erosion Mechanism).

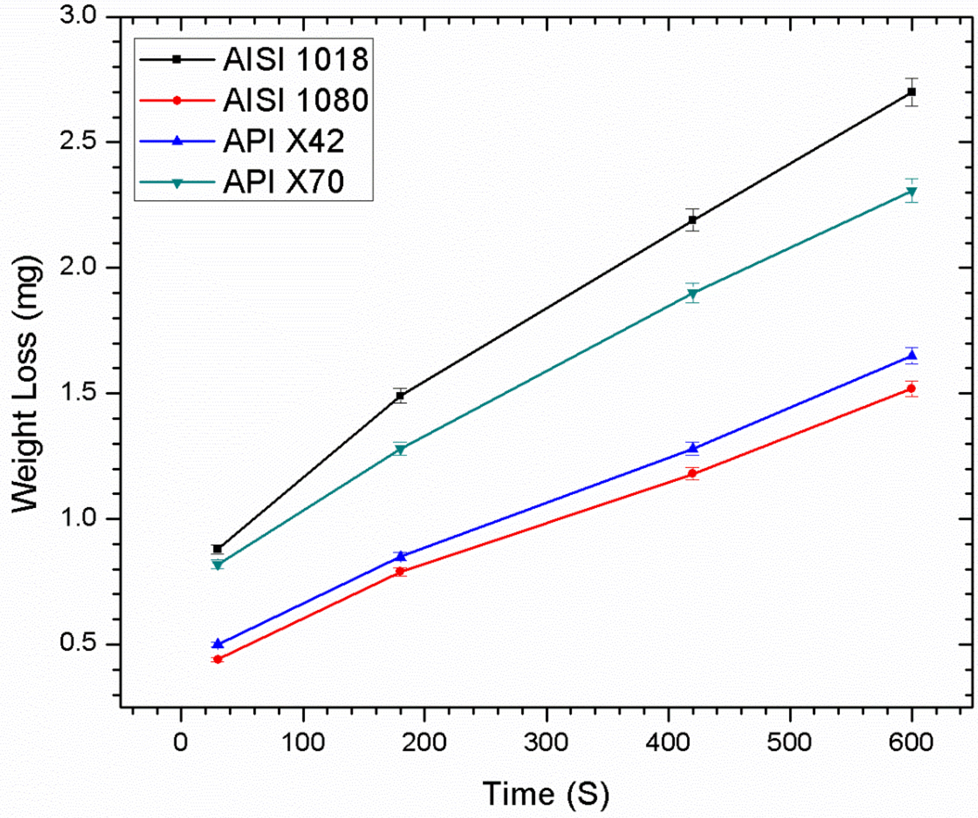

Figure 4-1 Weight loss vs time for AISI 1018, AISI 1080, API X42 and API X70 steel at 0.43 m s^{-1} slurry velocity and normal impact angle.

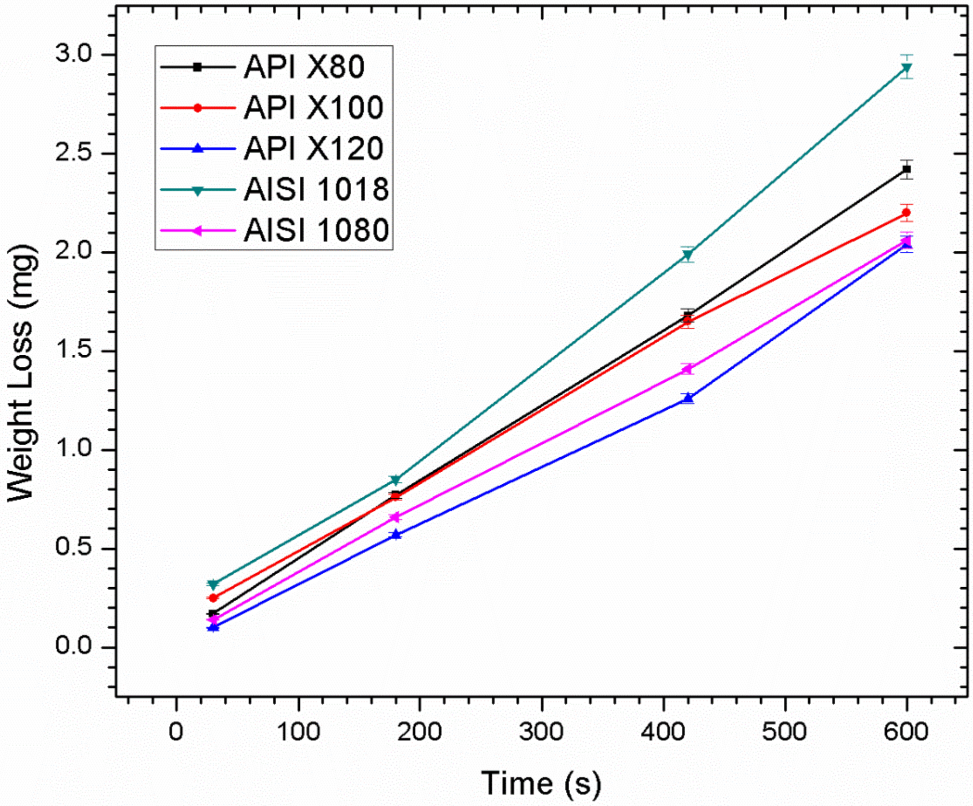

Figure 4-2 **Weight loss vs time for AISI 1018 steel for 3% slurry concentration and 12 m s^{-1} slurry velocity at normal impact angle.**

4.1.1 Eroded Surface Topography

Eroded surface topography has been studied by performing profilometry scan on each specimen after the slurry erosion test at 4% concentration. Scanned profiles were then stitched together for comparison (Figure 4-3). According to these scans, the maximum depth of the erosion scar varies from 2.45 µm to 24.14 µm at 4% concentrations for 30s to 600s. The maximum depths were calculated by measuring the deepest points of the scars to the unaffected surfaces of the materials.

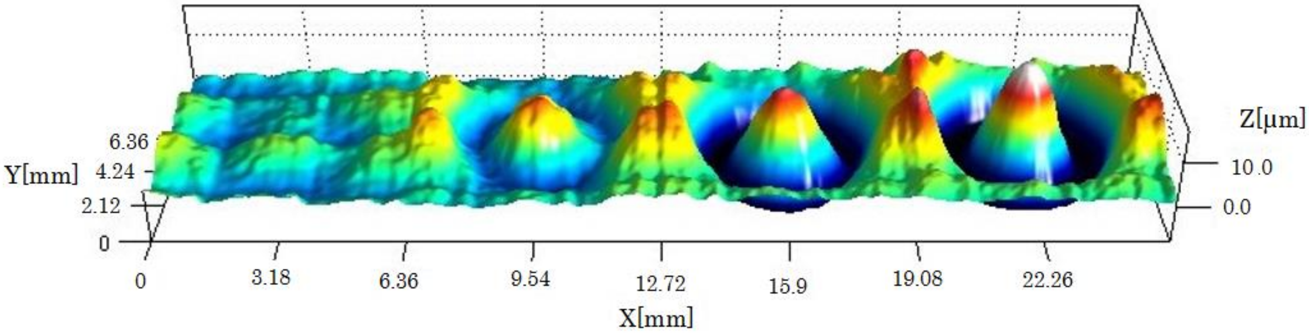

Figure 4-3 Erosion scar of AISI 1018 at 4% concentration for normal angle of incidence and different time intervals (from left to right, 30, 180, 420 and 600 s) profilometry scan (aspect ratio, 1:1:0.5).

During the erosion test, repeated impact by the slurry on the material surface induces plastic deformation, which favors an increase in surface roughness. However, the mean surface roughness of eroded AISI 1018 was found to be 5.1±2 µm. Then again, the average particle size used in this study was 57 ± 2 µm. So it can be said that the localized surface roughness didn't affect the global impact angle. Hence, the local surface roughness was not expected to have significant effect on erosion rate. It is clear that the depth of the erosion scar (Z axis) is shallow compared to the size of the scar (X and Y axis). Thus, it is evident that the depth of the erosion scar is shallow enough with respect to incoming slurry that local impact angle of slurry flow is reasonably close to the incident angle of the slurry stream.

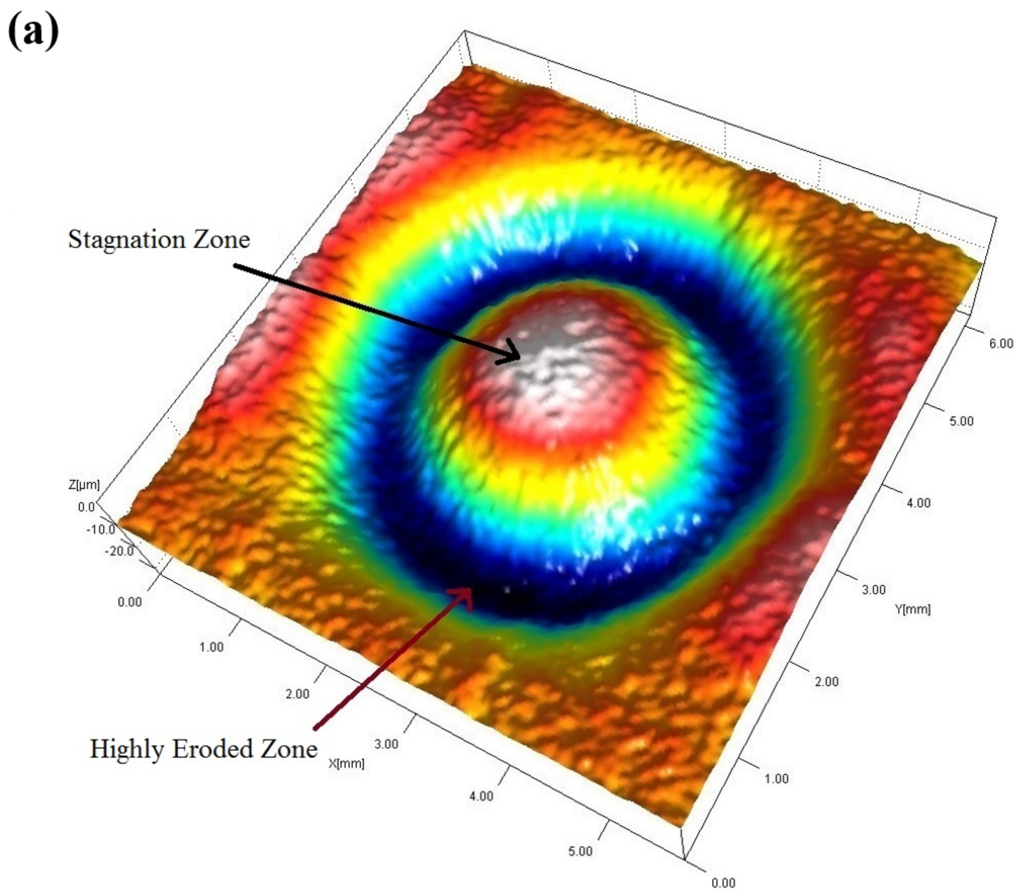

Figure 4-4 Erosion scar of AISI 1018 at 4% slurry concentration for 600s and normal angle of incidence, (a) profilometry scan (aspect ratio, 1:1:40).

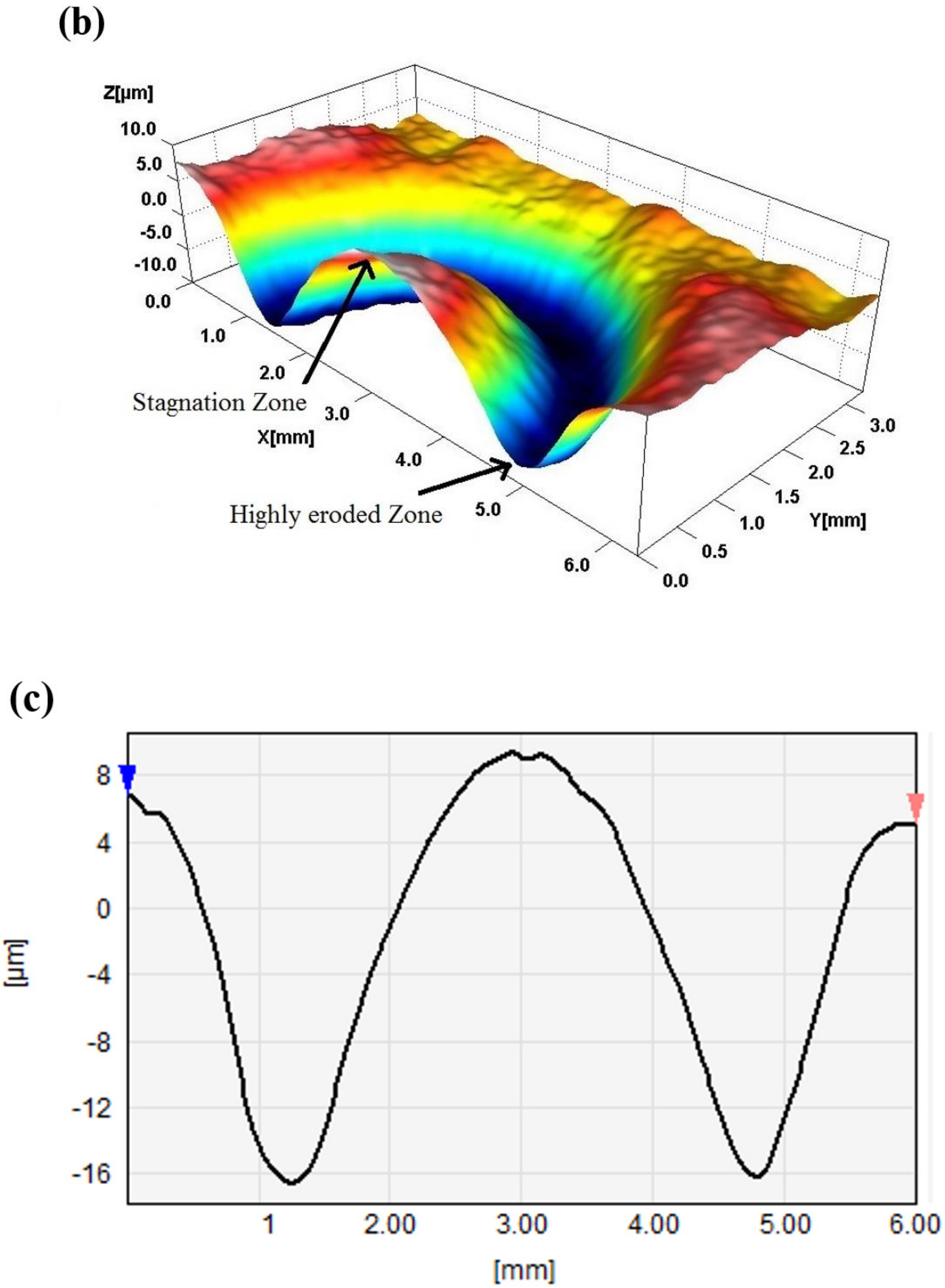

Figure 4-4 Erosion scar of AISI 1018 at 4% slurry concentration for 600s and normal angle of incidence, (b) the cross section of eroded surface profile (aspect ratio, 1:40). and (c) profile depth comparison (aspect ratio, 1:40).

It is interesting to note that, the profile of the cross-section of the eroded surface was found to be "W" shaped in the current study (Figure 4-4 (b)). Similar finding was reported by Mansouri et al. [126]. The fluid dynamics of slurry is primarily responsible for this phenomenon. The fluid flow pattern of slurry depends upon the Reynolds number (R_e) and is given by [124],

$$R_e = \frac{\rho_f UL}{\mu} \qquad \text{Equation 4-1}$$

where, ρ_f and μ are the fluid density and viscosity, respectively. U is the flow velocity and L is the cross-section of the channel. On the other hand, the abrasive particles behavior within the slurry flow can be characterized by Stokes number of the particle (S_t), as follows [124],

$$S_t = \frac{4}{3}\frac{\rho_p}{\rho_f}\frac{a}{L} \qquad \text{Equation 4-2}$$

S_t is proportional to the ratio of the abrasive particle inertia to the fluid drag force. Abrasive particle inertia attempts to keep the particle on its original trajectory.

An important parameter that determines if and where an abrasive particle would impact the surface in a pipe bend on T-channel is the thickness of the boundary layer (δ) [124],

$$\delta = \frac{L}{\sqrt{R_e}} \qquad \text{Equation 4-3}$$

As the boundary thickness increases as a result of low Reynolds number (i.e., low fluid velocity) for a given low value of Stokes number of the particle, the abrasive particle would deviate more from its original trajectory and towards the streamline of the flow.

Abrasive particles suspended in liquid tend to follow the direction of slurry flow for low Stokes number[124], [166], [167]. Due to low Reynolds number of the fluid and low Stokes number of the abrasive particle in slurry, a stagnation zone was developed at the center of the eroded surface where the velocity of the incoming slurry reduces to zero (Figure 4-4 (a)), as reported in a previous study [126]. Hence, total mass loss at the center due to slurry erosion is negligible. Accordingly, the velocity of the slurry increases gradually away from the stagnation zone. The abrasive particles impact occurs of some distance from the stagnation zone and forms a ring of highly eroded region of the surface of the steel, as shown in Figure 4-4 (a). The 2D profile of Figure 4-4 (a) is represented in Figure 4-4 (c). The entire phenomenon can be explained more clearly by Figure 4-5. During the erosion test, the entire system (nozzle and specimen holder) was submerged in the slurry mixture. After the slurry was ejected from the nozzle, the fluid flow deviates to both sides of the channel. On the other hand, the abrasive particles path is influenced by two factors, particle inertia, which attempts to keep the particle moving in its original straight path and the fluid flow stream pulls the particle in its deviated path. The position where the abrasive particle impacts the surface is controlled by the extent of these two effects. As a result, the velocity of the slurry reduces to zero at the center of the eroded profile and creates a stagnation zone. The region where the abrasive particles impact the steel surface show high erosion as shown in Figure 4-5. However, the height of the stagnation zone was found slightly high compared to the unaffected steel surface (Figure 4-4 (a) and 4-4 (c)). The reason behind this is that during the abrasive particle impact material deforms and flows of material from the highly eroded zone to the stagnation zone. Thus, the height of the stagnation zone increased compared to the unaffected surface. The entire mechanism is described in detail in later section (4.2 Erosion Mechanism, Figure 4-12).

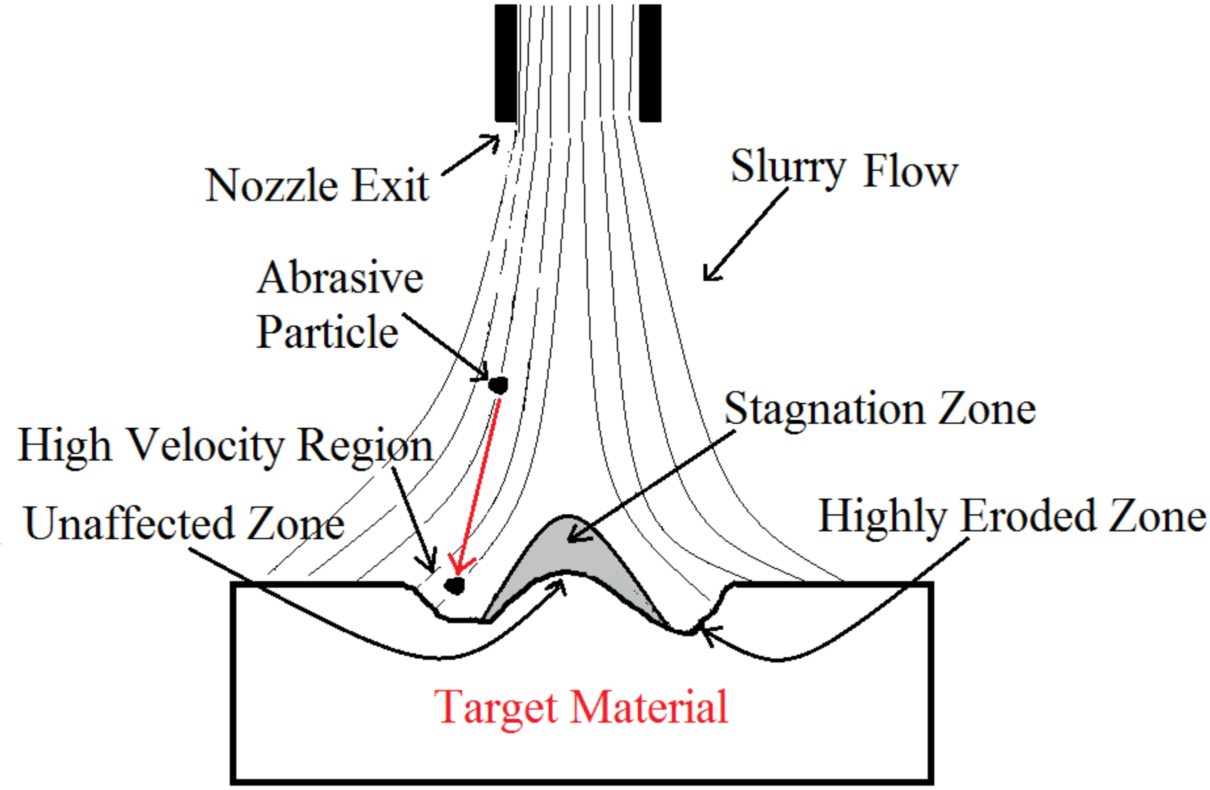

Figure 4-5 **Schematic diagram of the velocity contour of the slurry flow at normal impingement angle.**

4.1.2 Effect of Slurry Velocity

Slurry erosion rate was determined from the slope of weight loss vs time plot. Slurry flow rate was calculated by measuring total slurry weight (water + abrasive particle) per unit time. To be able to compare erosion rates performed using different particle velocities, the erosion rate is normalized with respect to the slurry flow rate for a given slurry velocity.

Figure 4-6 shows normalized erosion rates as a function of slurry velocity. It was observed that slurry erosion of AISI 1018, AISI 1080, API X42 and API X70 steel increases with increasing slurry velocity. Several researchers reported that higher material removal rate at higher particle velocity is due to the higher kinetic energy of the abrasive particles [168]–[170]. However, the abrasive particle has to attain a critical velocity to induce plastic deformation on the surface[122]. At lower slurry velocity, most particles have velocities below a threshold value which causes elastic deformation. As a result, lower erosion rate was observed at low slurry velocity. On the other hand, when slurry velocity is increased, more abrasive particles attain the required threshold velocity. Continuous impact by the abrasive particles with velocity higher than the critical value develops plastically deformed platelets, which are then detached upon further impacts. Hence, the erosion rate increases with increasing slurry velocity as evident from Figure 4-6. However, it is interesting to note that, the slope of the curve in Figure 4-6 varies with varying slurry velocity. At higher slurry velocity, embedded particles are observed in the steel specimen which acts as reinforcing elements. As a result, the slope of normalized erosion rate vs slurry velocity decreases as slurry velocity increases. It is important to note that, normalized erosion rate of AISI 1018 steel is higher than AISI 1080 steel for all velocity conditions used in this study. Steel microstructure plays an important role in determining the erosion rate. AISI 1018 steel exhibits 20% pearlite while AISI 1080 exhibits almost 100% pearlitic microstructure (Table 3-1). Thus, normalized erosion rate data indicates that pearlite is more effective in resisting erosion than ferrite.

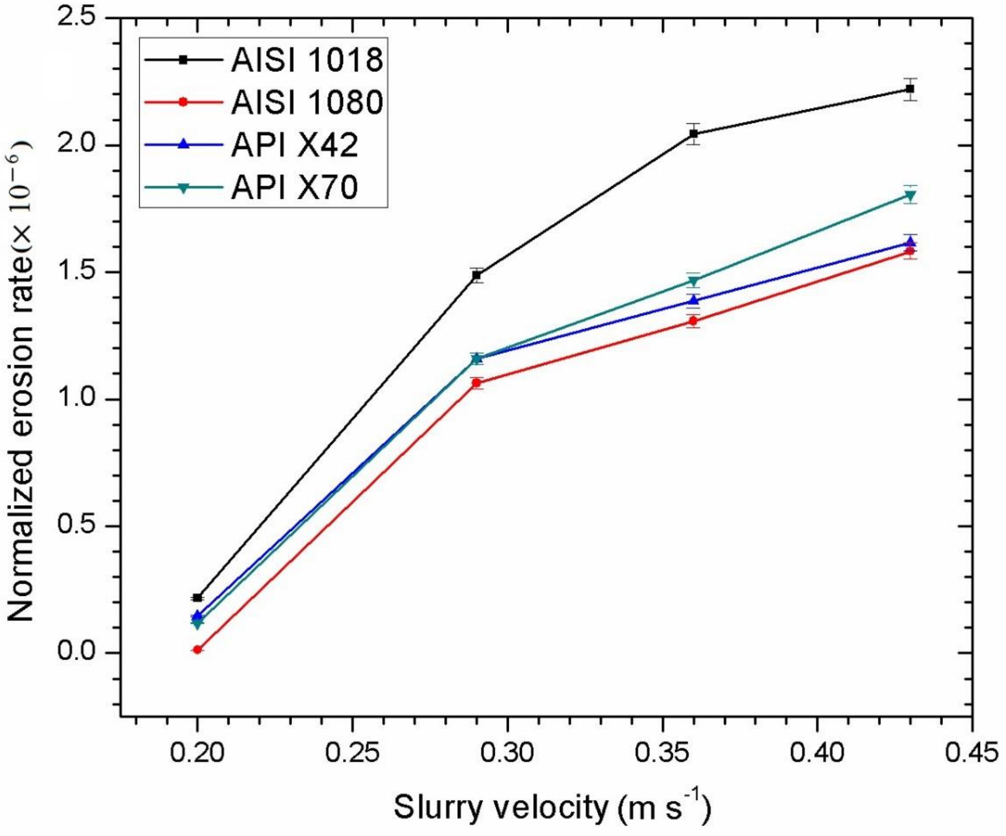

Figure 4-6 **Normalized erosion rate vs slurry velocity for AISI 1018, AISI 1080, API X42 and API X70 steel at normal impact angles.**

4.1.3 Effect of Slurry Concentration

Figure 4-7 shows the change in normalized erosion rate as a function of slurry concentration. It can be seen from the figure that the normalized erosion rates of AISI 1018, AISI 1080, API X80, API X100 and API X120 increase with increasing slurry concentration as observed in other erosion studies [63], [109], [110], [153]. This is because of the fact that, at low slurry concentration, the particle to material surface interaction area is much less compared to higher concentration slurry erosion test. Also, a previous study [122]] reported that abrasive particles have to attain a critical energy to induce plastic deformation on the material surface which is an essential condition for erosion degradation. At low slurry concentration, the amount of critically energized particle is less. As slurry concentration is increased, more particles acquire energies higher than the threshold value. Continuous impacts by these particles create plastically deformed platelets, which are then detached by further interactions. Thus, erosion rate increased with increasing slurry concentration as evident in Figure 4-7. However, it is interesting to note that, the slope of the Figure 4-7 changes with increasing slurry concentrations. The main reason for this phenomenon is “cushioning effect” [109]. At high slurry concentrations, the incoming slurry stream collides with the backscattered particles, which protects the material surface, this is known as “cushioning effect”. This effect is gradually increased with increasing slurry concentration. Hence, the slope of the normalized erosion rate vs slurry concentration decreases as slurry concentration increases.

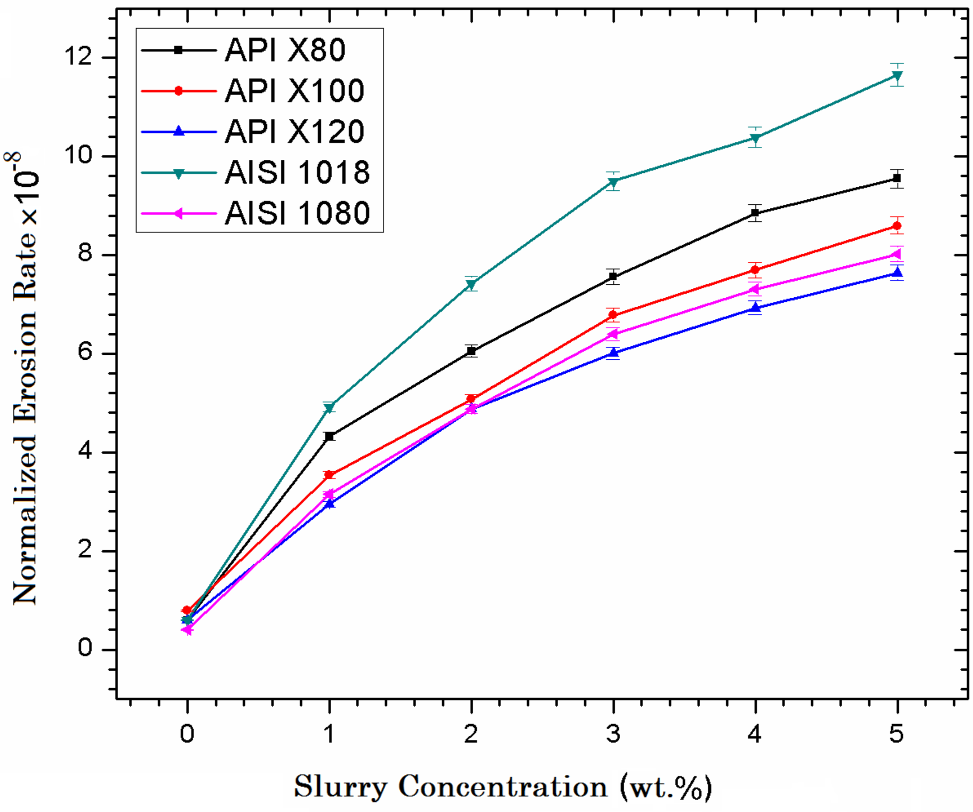

Figure 4-7 Normalized erosion rate vs slurry concentration for AISI 1018, AISI 1080, API X80, API X100 and API X120 steel at normal impact angles.

4.2 Erosion Mechanisms

Erosion is a complex and progressive time dependent phenomena. Several environmental factors have significant influences on slurry erosion mechanisms of pipeline steels. Different erosion mechanisms were found acting simultaneously depending upon the operating conditions, abrasive particle size, shape and trajectory. The total erosion rate is the sum of the individual contributions of these mechanisms. Thus, identification of dominant erosion mechanisms is a challenging task. SEM images were taken at different zone of the eroded profiles where the damage caused by individual particle impact could be seen. However, it is important to note that, erosion mechanisms are the function of slurry velocity and concentration and the steels used in this study show similar erosion mechanisms for a particular set of environmental condition. In this section, erosion mechanisms of steels are divided based on slurry velocity and slurry concentration.

4.2.1 Effect of Slurry Velocity

During slurry erosion, plastic deformation on eroded surfaces is observed at both low and high velocity conditions. Figure 4-8(a) shows the eroded surface morphology for AISI 1018 steel. Plastic deformation and formation of platelets are dominant because of the continuous impact by the sharp abrasive particles. These platelets are then removed due to repeated impacts by the incoming particles. Similar phenomenon was reported in previous studies [171], [172]. Figure 4-8(b) shows plastic deformation in API X70 steel. As the abrasive particle strikes the surface, the deformed material is squeezed out of the contact zone. Repeated impacts by the abrasive particles cause fracture of the platelets as evident in Figure 4-8 (c). As more particles strike the surface, platelets begin detaching from surface and form small fragments (Figure 4-8 (d)). Similar behavior is also observed in previous studies [168], [173]–[175].

At higher slurry velocity, due to rebounding effect, abrasive particles deflect from their original trajectory. These abrasive particles have velocities higher than the threshold value and are observed to cause microcutting action (Figure 4-8 (e)) [176][177][178]. The rebound particles collide with new incoming particle and deflect them from their original trajectory. Those deflected particles impact the specimen surface at an acute angle and cause microcutting. At high impact velocity, deep penetration of abrasive particles results in embedded Al_2O_3 as shown in Figure 4-8 (f). It is found that crack initiates in embedded particles due to repeated impact by the incoming slurry stream (Figure 4-8 (f)). Some of these embedded particles are then fractured and removed from the matrix (Figure 4-8 (g)). Removal of embedded particle creates vulnerable ridges, which are then detached by further impact (Figure 4-8 (h)).

Figure 4-9 shows a schematic diagram explaining how the material is removed during slurry erosion. At the initial stage of erosion, abrasive particles impact the steel surface (Figure 4-9 (a)) and deform the metal plastically. Plastic deformation on the specimen surface creates vulnerable lips. The rebound particle then inhibits the motion of the incoming abrasive particle (Figure 4-9 (b)). After collision with the rebound particle, the new abrasive particle deflects from its original trajectory (Figure 4-9 (c)) and the abrasive particle impacts the specimen surface at an acute angle. Material is then removed through microcutting (Figure 4-9 (d)). Figures 4-9 (e)-(f) show the removal of vulnerable lips due to repeated impact by the abrasive particles.

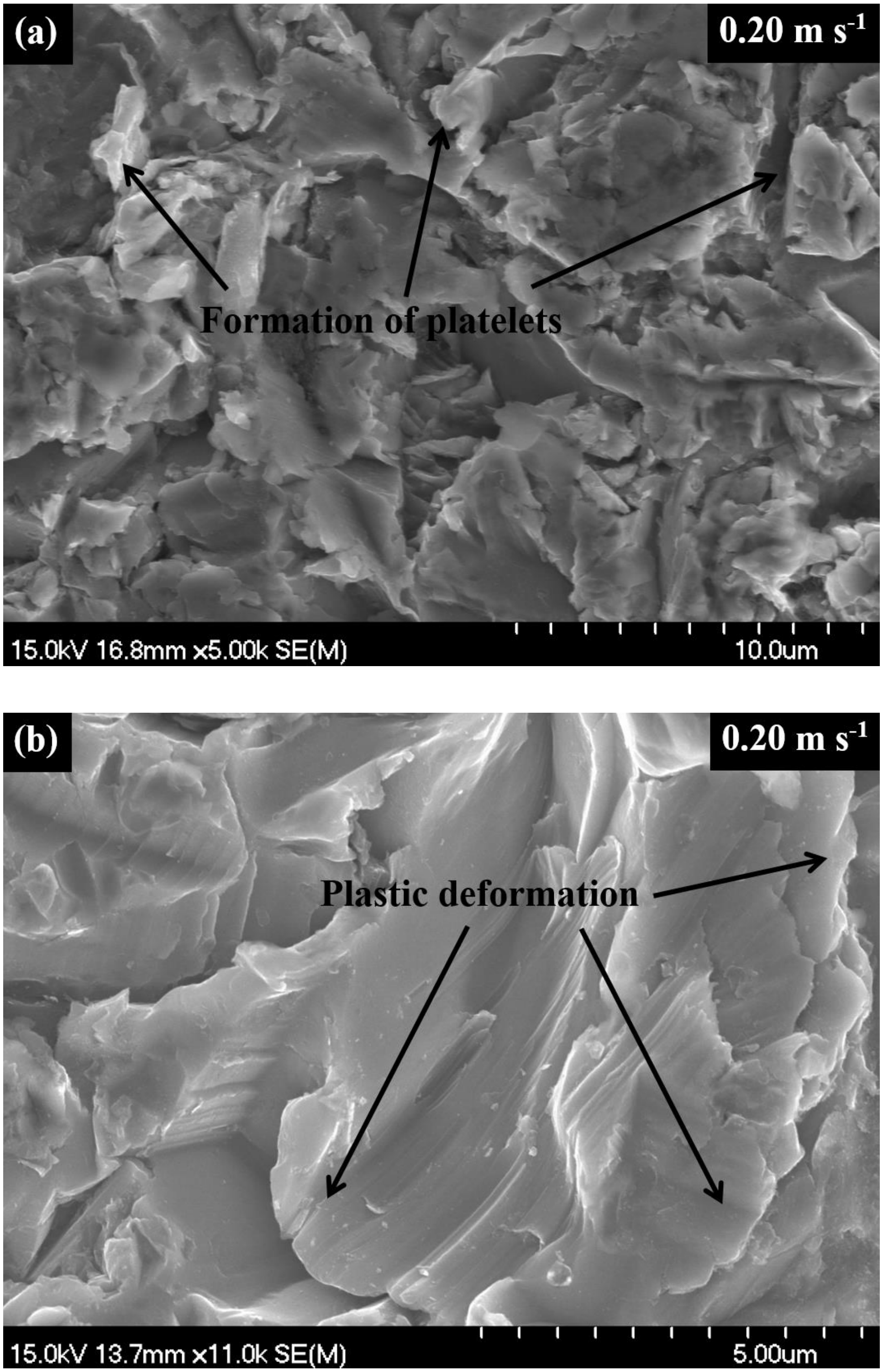

Figure 4-8 SEM micrograph of steel samples after slurry erosion, (a) formation of platelets due to plastic deformation (AISI 1018, 0.20 m s^{-1}) and (b) plastic deformation (API X70, 0.20 m s^{-1}).

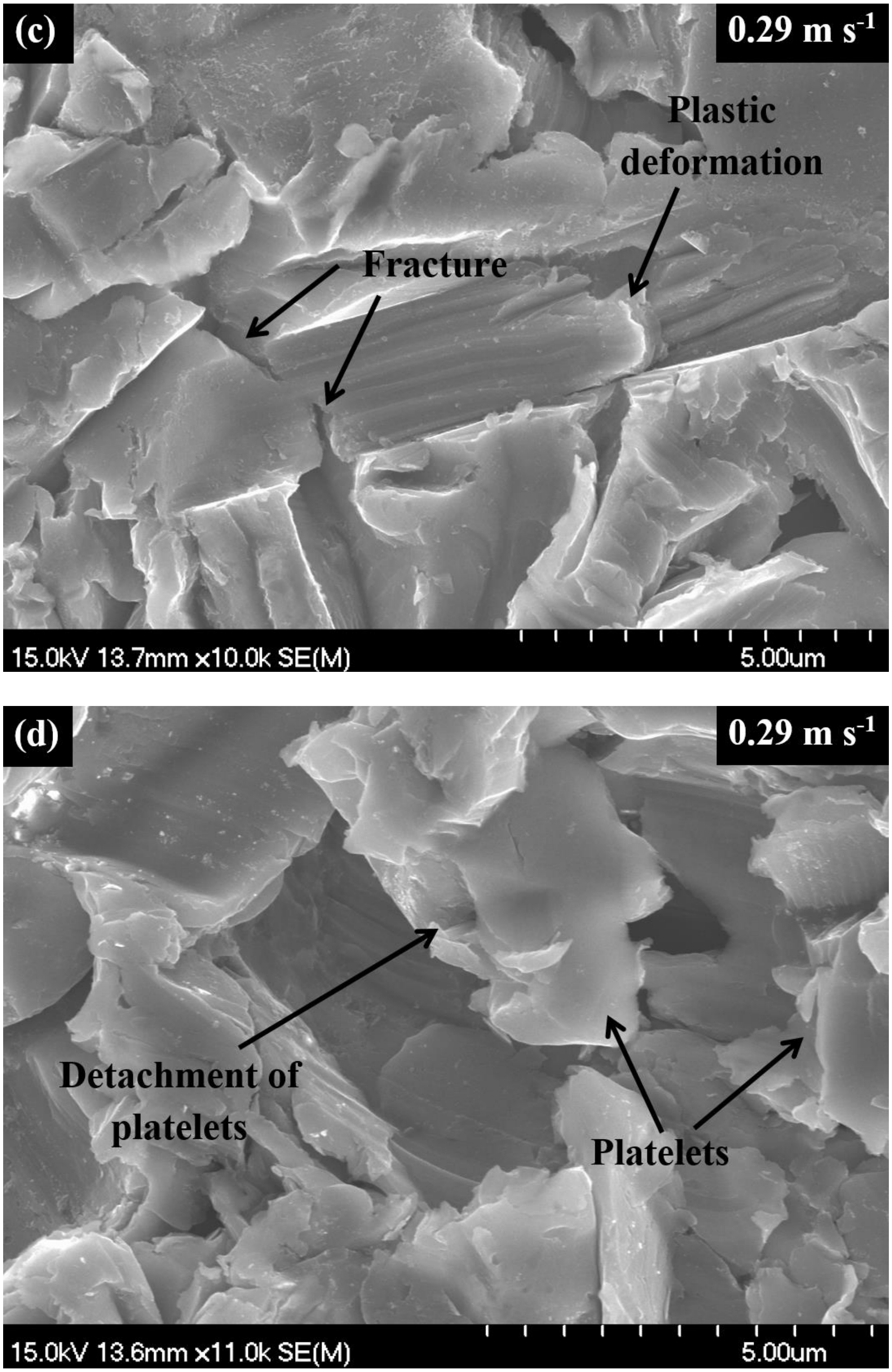

Figure 4-8 SEM micrograph of steel samples after slurry erosion, (c) initiation of fracture at deformed platelets (API X70, 0.29 m s^{-1}) and (d) detachment of deformed platelets (API X70, 0.29 m s^{-1}).

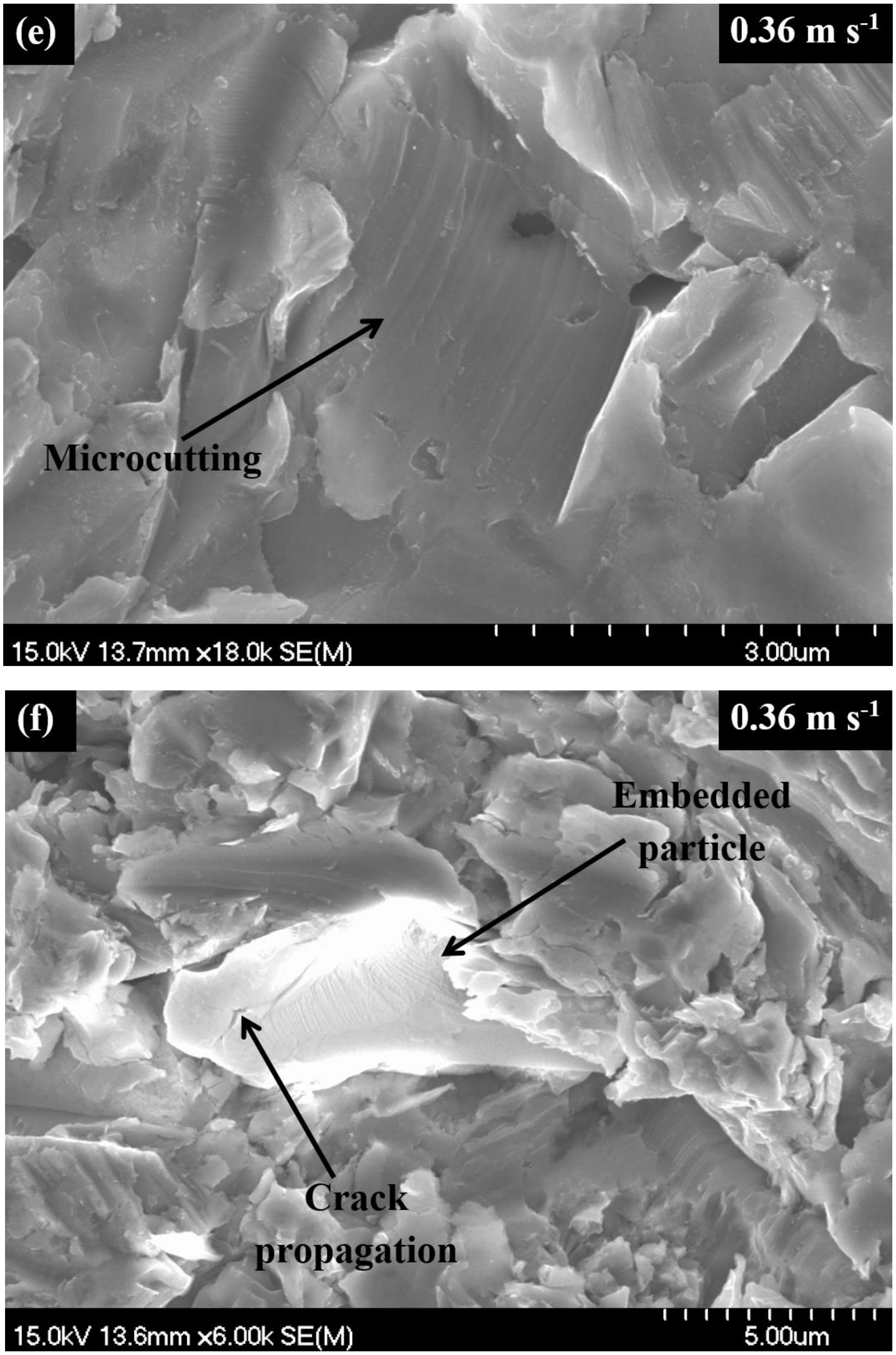

Figure 4-8 SEM micrograph of steel samples after slurry erosion, (e) microcutting (API X70, 0.36 m s^{-1}) and (f) embedded abrasive particle (API X42, 0.36 m s^{-1}).

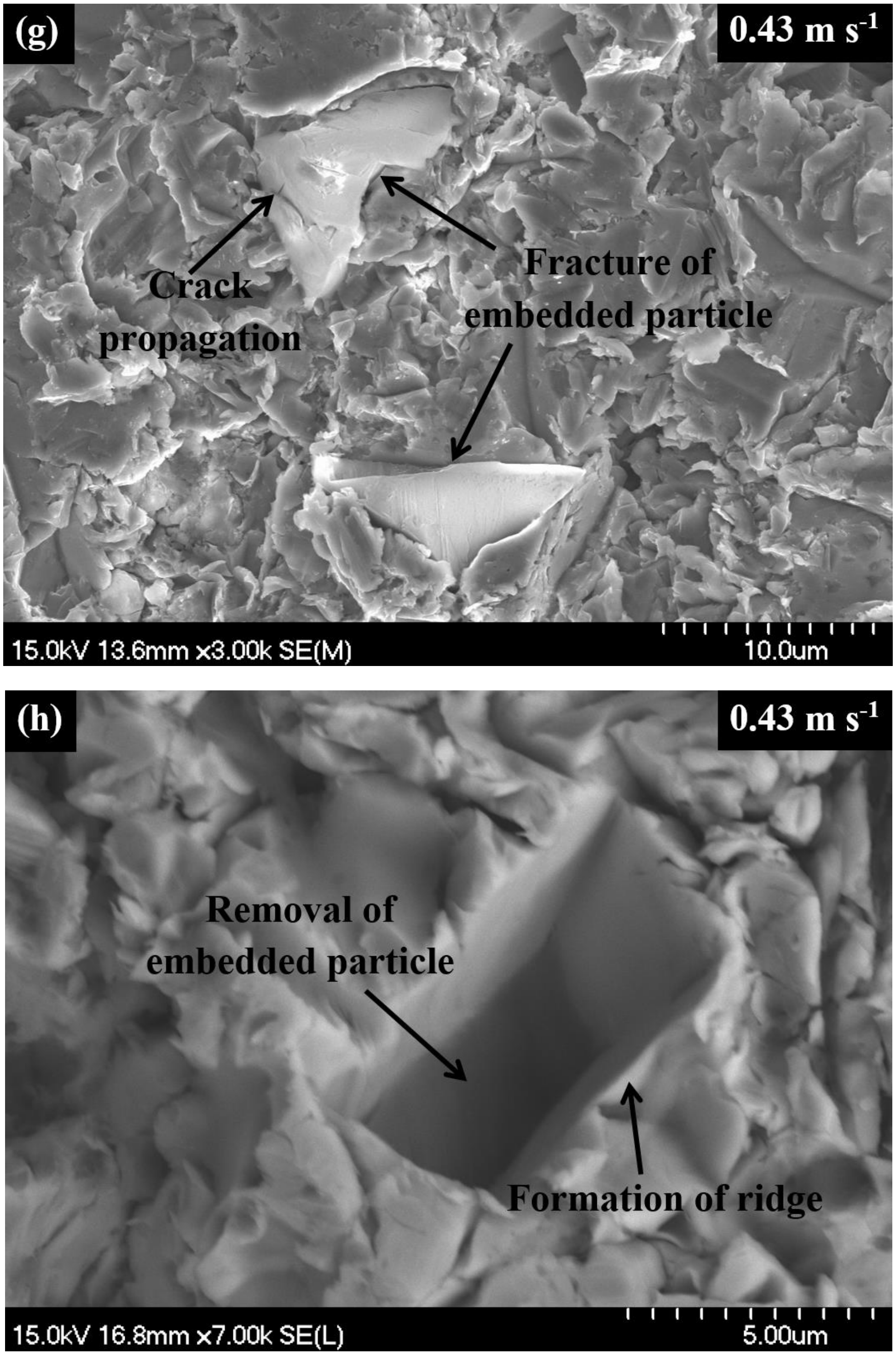

Figure 4-8 SEM micrograph of steel samples after slurry erosion, (g) crack propagation in embedded particle (API X42, 0.43 m s^{-1}) and (h) removal of embedded particle (API X42, 0.43 m s^{-1}).

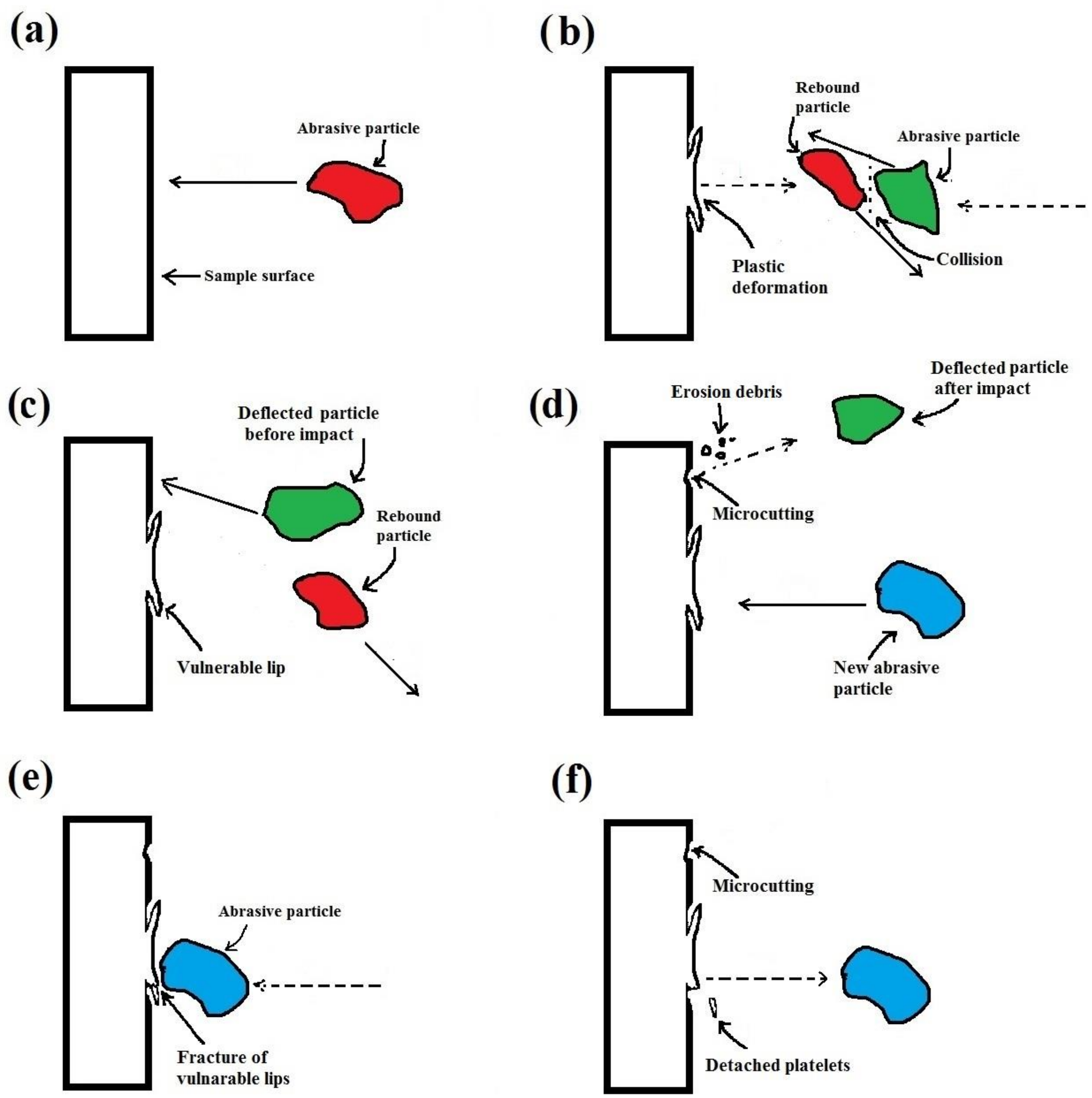

Figure 4-9 Effect of rebound particle on slurry erosion mechanism, (a) abrasive particle impacts on the sample surface at 90° angle, (b) plastic deformation and formation of vulnerable lip due to impact of abrasive particle impact and rebound abrasive particle collide with new incoming abrasive particle, (c) deflection of abrasive particle after collision, (d) deflected abrasive particle strikes sample surface at acute angle and material is removed through microcutting and (e)-(f) repeated impact by the abrasive particle causes fracture and removed vulnerable lips.

4.2.2Effect of Slurry Concentration

In this study, the eroded profile shows two distinct zones on the material surface which are denoted as the stagnation zone and the highly eroded zone. Figure 4-10(a) shows the optical image of an eroded surface where the stagnation zone at the center and the highly eroded zone are clearly visible. Figure 4-10 (b) and Figure 4-10 (c) represents a low magnificent SEM images of the stagnation zone and the highly eroded zone respectively. The stagnation zone shows evidence of plastic deformation. On the other hand, the presence of plastically deformed platelets, crater, microcutting, and ploughing were observed in the highly eroded zone.

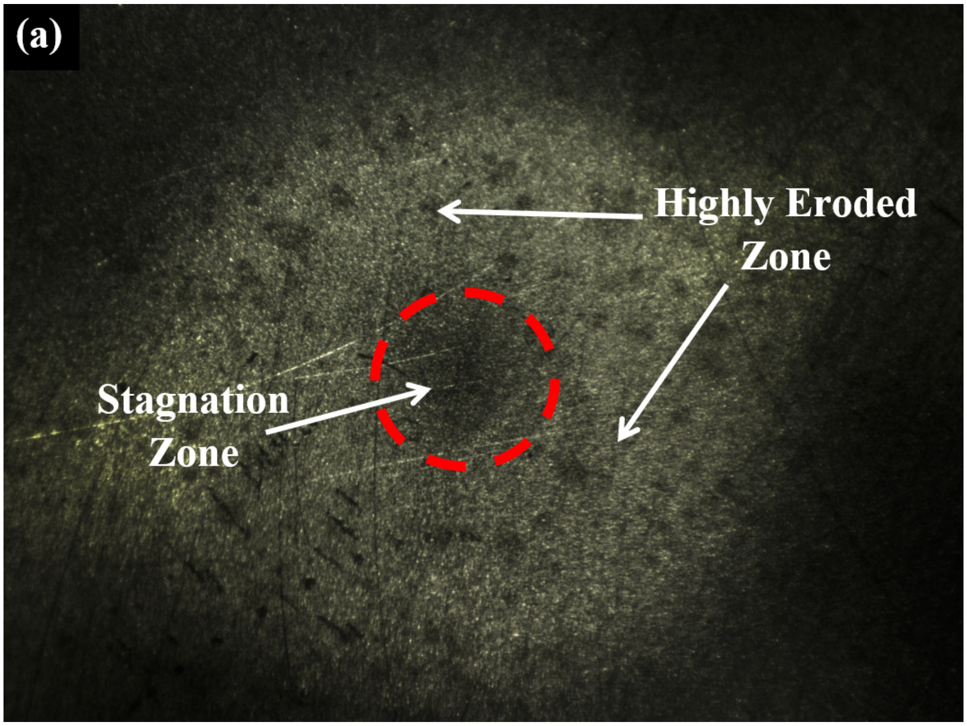

Figure 4-10 (a) Optical micrograph of eroded profile of API X120.

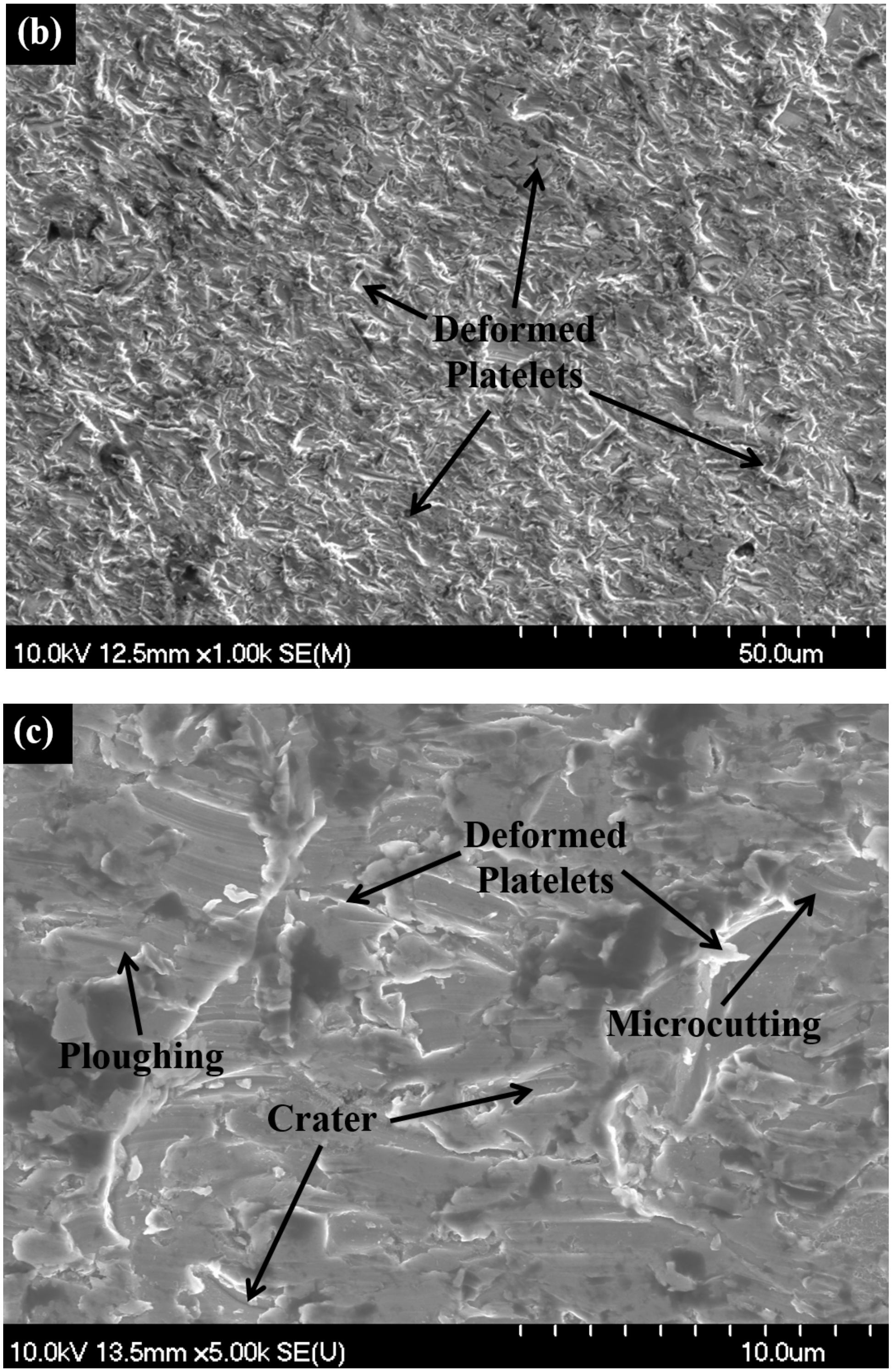

Figure 4-10 (b) SEM micrograph of the stagnation zone of API X120 and (c) SEM micrograph of the highly eroded zone of API X120 steel at 4% slurry concentration.

When the slurry strikes the highly eroded zone, abrasive particles in slurry induce plastic deformation on the steel surface. Figure 4-11(a) shows the formation of plastically deformed platelets on the highly eroded zone. As more particles impact the surface, crack initiates at the deformed platelets as shown in Figure 4-11(b). Repeated impact by the energized abrasive particles completely detached the deformed platelets as evident in Figure 4-11(c) and form small fragments. These fragments are then washed away by the incoming slurry flow. Formation and detachment of plastically deformed platelets were identified as the dominant erosion mechanism for all the slurry concentrations used in this study as reported by other researchers[144], [179], [180]. Also, formation of craters was observed under SEM examination. Probable reason for crater formation is deep penetration of abrasive particles. The penetrated abrasive particles were then subjected to repeated impacts by incoming abrasive particles and subsequently removed from the material surface. Removal of the abrasive particles results in crater and vulnerable lip formation (Figure 4-11(d)). These vulnerable lips are then detached by further impact of forthcoming particles and cause erosion. Furthermore, continuous impact of the slurry on the material surface induces strain hardening and creates a work hardened layer on the surface. Normal impact of abrasive particles on the work hardened layer induces brittle fracture as evident in Figure 4-11(e). Figure 4-11(f) is the magnified image of Figure 4-11(e) and shows detached work hardened fragments caused by brittle fracture. These detached fragments are then removed from the steel surface by continuous slurry flow. Mass loss due to crater formation and strain hardening was reported by Shivamurthy et al. [154] and Bhandari et al. [111].

It was observed that, at higher slurry concentration, cushioning effect significantly influences erosion mechanisms. As we increase the slurry concentration, abrasive particles pile up in front of the material surface due to rebounding effect. These backscattered particles collide with the incoming slurry stream and alter the velocity and impact angle of incoming abrasive particles. Due to cushioning effect, some incoming abrasive particles deflect from their original trajectory. Depending upon the impingement angle and velocity of these deflected particles, several erosion mechanisms were observed on the material surface. When the deflected particles strike the material surface at low angle and low velocity, the horizontal component of the kinetic energy of the abrasive particle ploughs the surface as the particle slides over it (Figure 4-11(g)). Ploughing was reported as a dominant erosion mechanism at low angle and low velocity [122], [181]. Accordingly, the vertical component of kinetic energy of the abrasive particle at low angle and high velocity causes microcutting as evident in Figure 4-11(h). Presence of microcutting at the normal impact angle was also observed in other studies [154], [182].

In summary, different erosion mechanisms were identified acting on the steel surface depending upon the operating conditions. The formation and removal of heavily deformed platelets was found as the dominant erosion mechanism. Furthermore, deflected particles, created by the collision with the backscattering particles, also caused erosion damage. Ploughing and microcutting were found to be caused by deflected particles depending upon the altered impact angle and particle velocity.

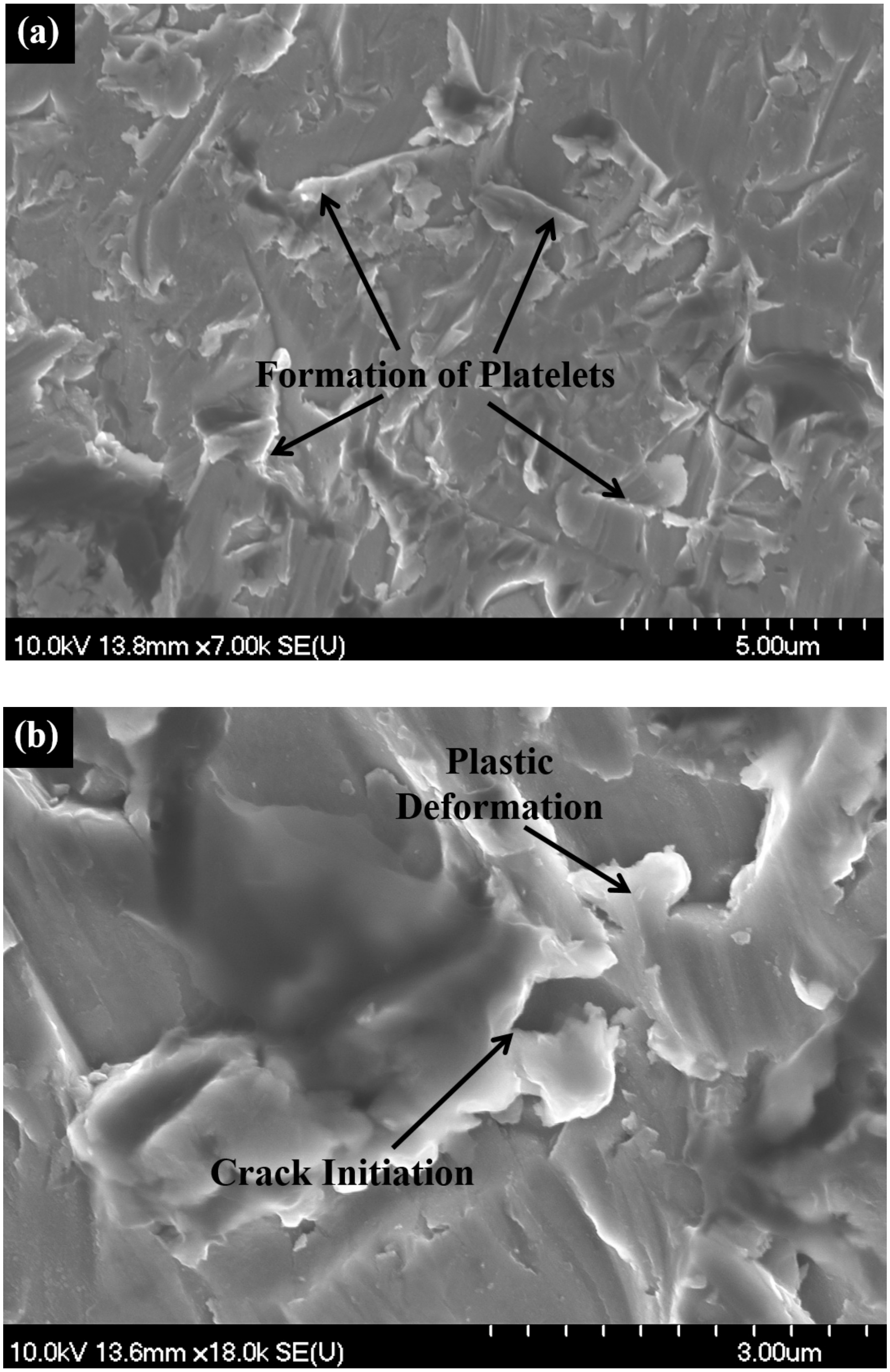

Figure 4-11 SEM micrograph of highly eroded zone of steel specimens, (a) formation of deformed platelets (API X120) and (b) plastic deformation and initiation of crack at deformed platelets (API X120).

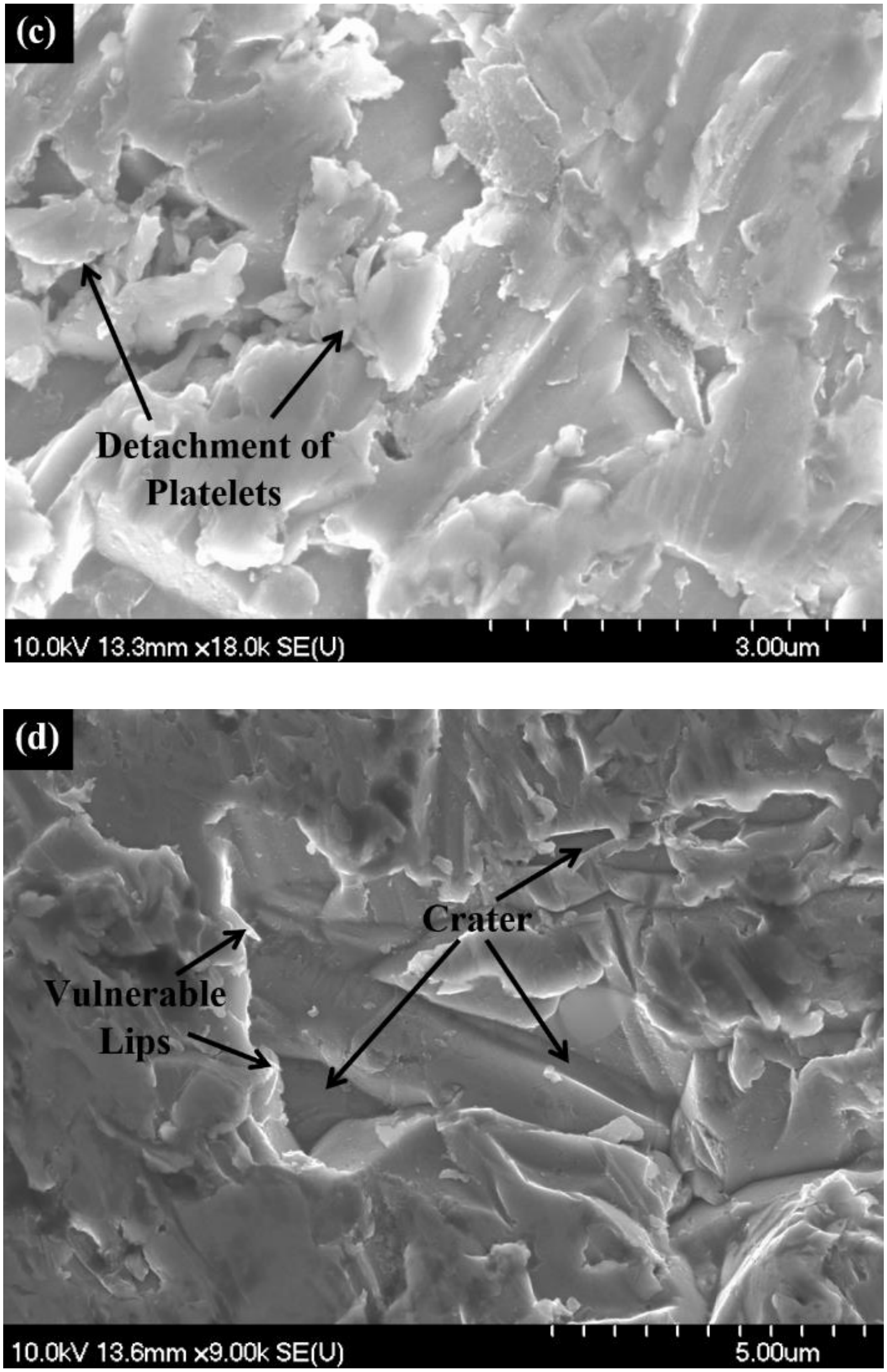

Figure 4-11 SEM micrograph of highly eroded zone of steel specimens, (c) detachment of deformed platelets (API X120) and (d) crater and vulnerable lip formation (API X120).

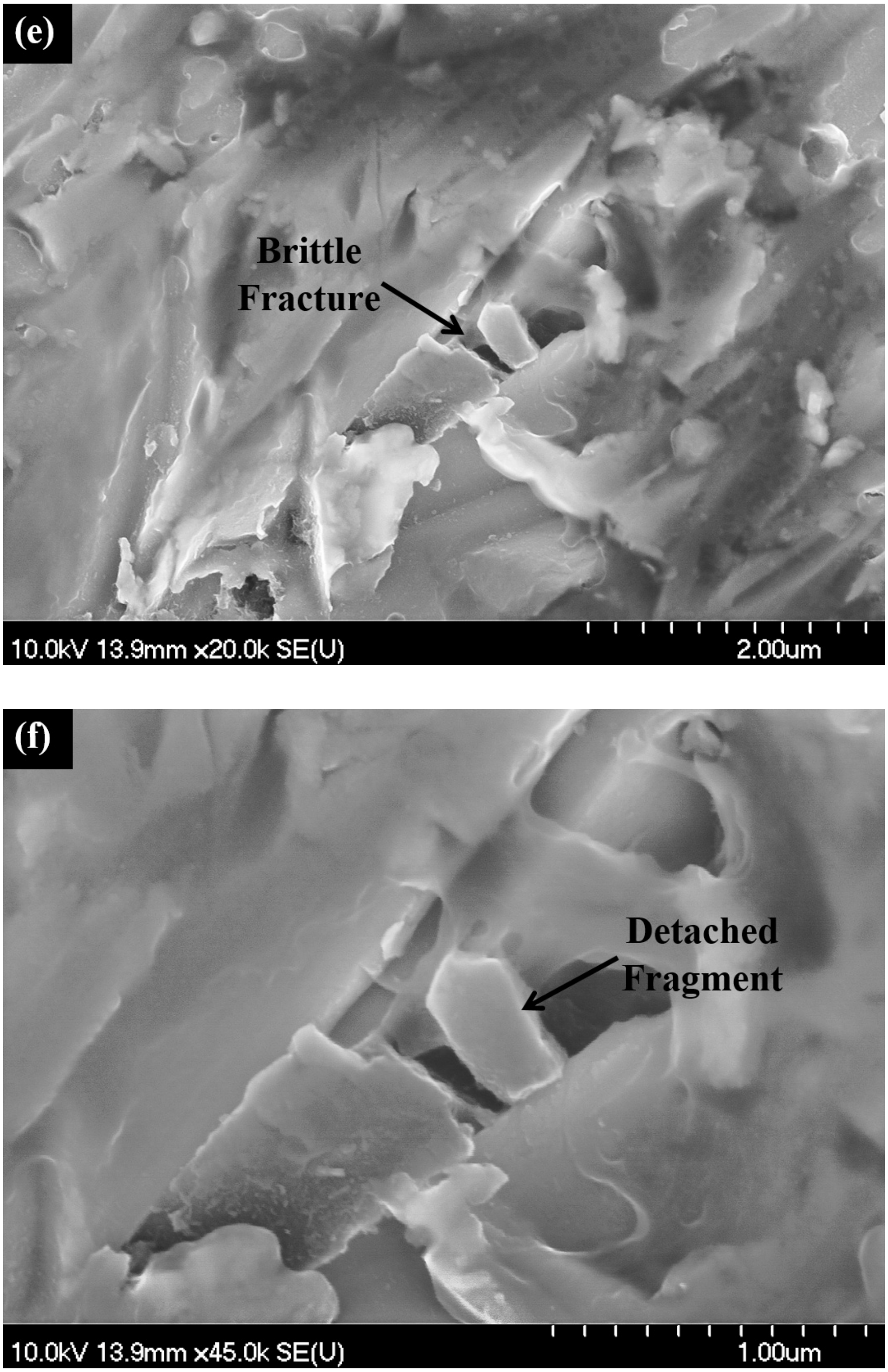

Figure 4-11 SEM micrograph of highly eroded zone of steel specimens, (e) brittle fracture of work hardened layer (AISI 1018) and (f) detached work hardened fragment (AISI 1018).

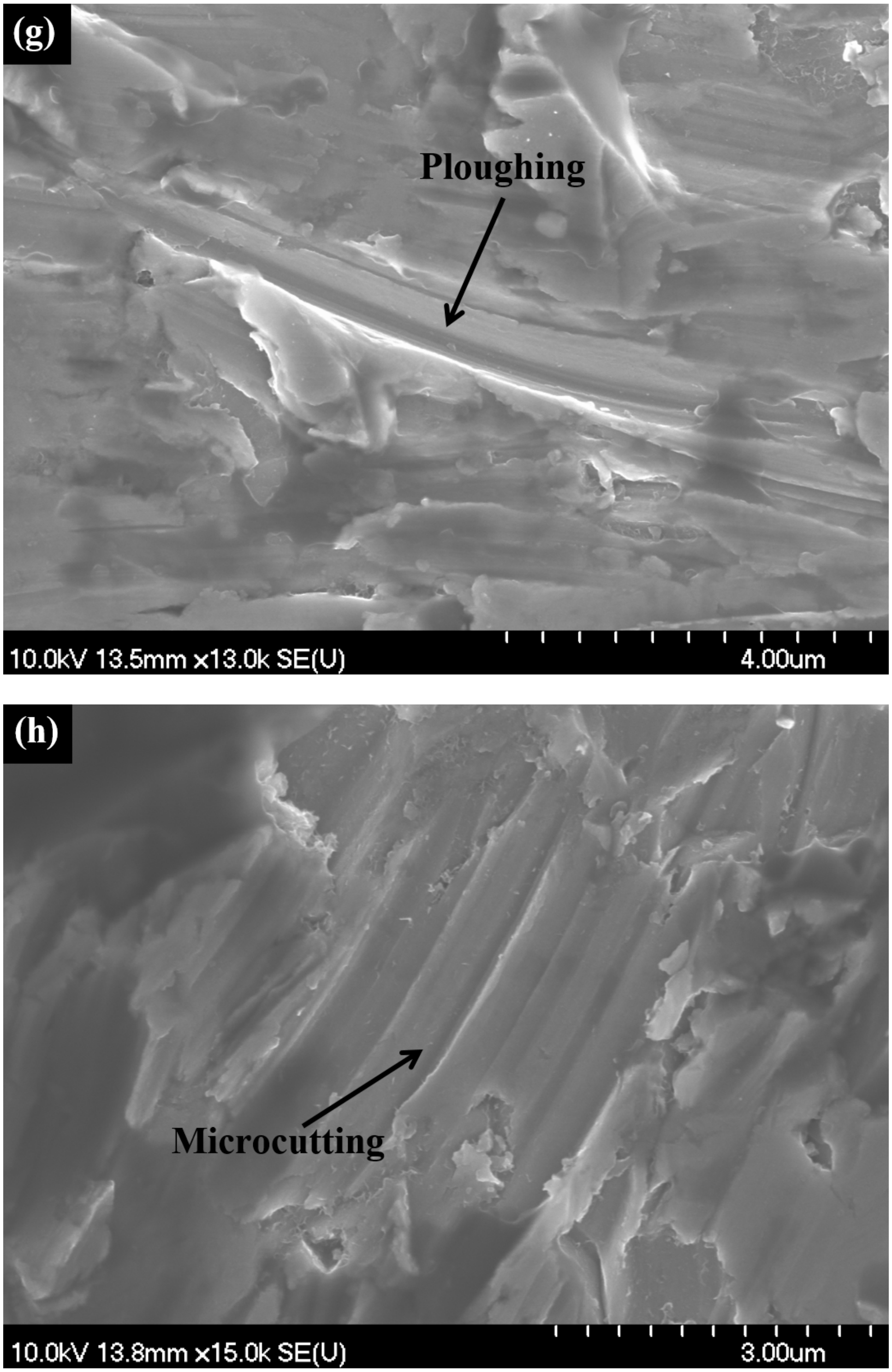

Figure 4-11 SEM micrograph of highly eroded zone of steel specimens, (g) ploughing (AISI 1018) and (h) microcutting (AISI 1018).

During plastic deformation, material is squeezed out of the contact zone. Further impact is necessary to detach the deformed platelets in order to cause erosion. At the highly eroded zone and stagnation zone boundary, deformed material flows from the eroded zone to the stagnation zone. Figure 4-12(a) shows the flow of materials due to plastic deformation. However, the slurry velocity approaches zero at the stagnation zone, as a result, no particle-material collision takes place at the stagnation zone. Hence, metal, flow from the eroded zone, piled up at the stagnation zone without material detachment (Figure 4-12(b)). This explains the increase in height of the stagnation zone compared to the unaffected surface which is evident in Figure 4-4.

Figure 4-13 shows a schematic diagram explaining the erosion mechanisms at the highly eroded zone-stagnation zone boundary. At the initial stage, abrasive particles impact the steel surface and induce plastic deformation (Figure 4-13 (a) and (b)). Deformed material then flows and creates vulnerable lips (Figure 4-13 (b)). At the highly eroded zone, slurry contains critically energized abrasive particles. Repeated impact by these energized particles initiate fracture of the vulnerable lips at the highly eroded zone and cause erosion (Figure 4-13 (c)). However, the velocity of the abrasive particles are zero at the stagnation zone. Thus, flow of deformed material from the highly eroded zone piled up at stagnation zone without any material removal and raises the surface height compared to the unaffected area (Figure 4-13 (d)).

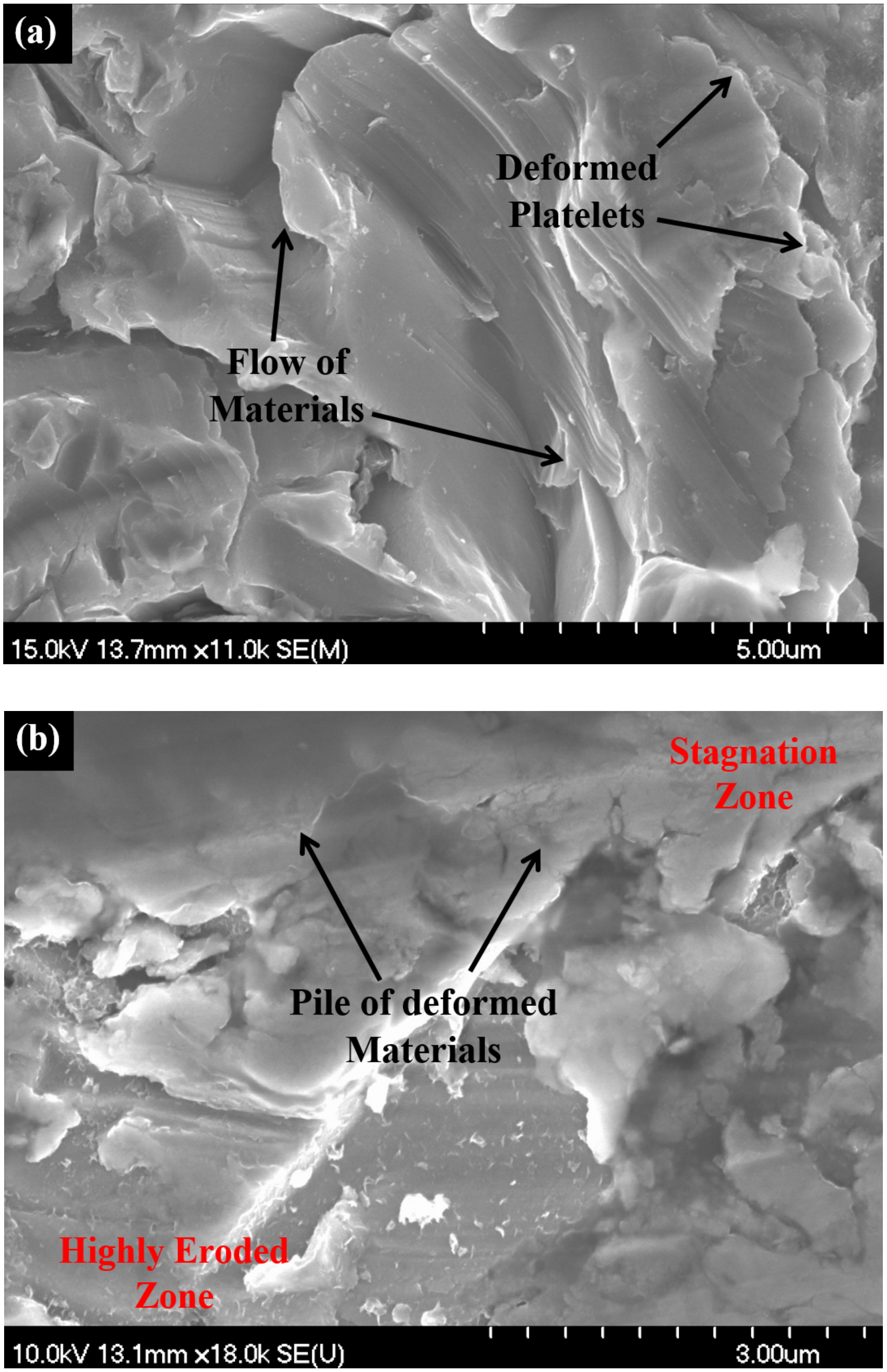

Figure 4-12 SEM micrograph of stagnation zone of steel specimens, (a) flow of materials due to plastic deformation (API X120) and (b) Pile of deformed platelets at stagnation zone (API X120).

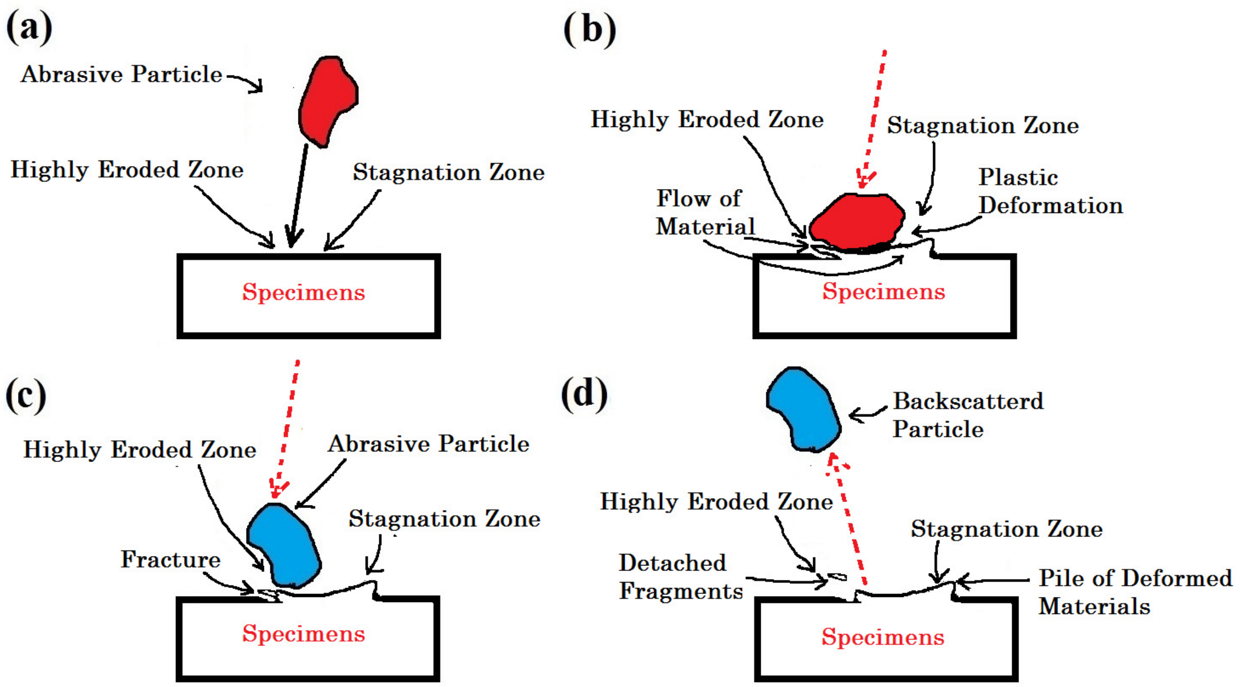

Figure 4-13 **Schematic diagram of erosion mechanism at the highly eroded zone - stagnation zone boundary, (a) abrasive particle impacts on the sample surface, (b) flow of material to stagnation zone from highly eroded zone and formation of vulnerable lips, (c) fracture of vulnerable lips at highly eroded zone and (d) pile of deformed materials at stagnation zone.**

4.2.3 Effect of Steel Microstructure

Slurry erosion of carbon steel is significantly influenced by the steel microstructure. In this study, the erosion response of ferritic and pearlitic microstructures were thoroughly investigated. Different degradation patterns were observed depending upon slurry velocity and microstructural orientation. SEM micrographs of eroded surface of AISI 1018 steel is shown in Figure 4-14.

During slurry erosion, localized and uniform surface deformations were observed as a result of the impact by the abrasive particles and the fluid flow. It was found that the deformation by abrasive particles is localized, while that due to fluid flow is uniform. Figure 4-14(a) shows an SEM micrograph depicting ferritic and pearlitic microstructure post slurry erosion. The continuous impact of the high pressure fluid flow induces uniform deformation on the surface and compresses the ferritic phase (Figure 4-14 (a)) and flattens the pearlitic plates as evident from Figure 4-14 (b). As can be seen in Figure 7(a), the ferrite phase is depressed deeper compared to the pearlite phase. This is expected as ferrite is softer than pearlite.

Figure 4-14 (c-d) shows the localized deformation on the steel surface caused by the abrasive particles. Abrasive particles deform the ferritic microstructure plastically (Figure 4-14 (c)) and create craters and ridges. Material is then removed upon further impact on the previously formed ridges. When abrasive particles impact a pearlite phase, heavy plastic deformation of the cementite lamellae is observed as shown in Figure 4-14 (d). It is interesting to note that, the localized degradation of pearlite by the abrasive particles depends on the orientation of pearlitic plates and the shape of the end of the particle that impacts the surface. Abrasive particles may strike pearlitic plates either with flat or sharp ends. Figure 4-14 (e) shows the deformation of cementite lamellae when the abrasive particle impacts with a flat end. As a result, heavy plastic deformation takes place. The impression that the particle left behind on the pearlite phase (Figure 4-14 (d,e)) indicates that the end of the particle which struck the surface had a flat shape (somewhat triangular). On the other hand, other particles strike the pearlite phase with sharp ends penetrate the pearlite plates along the cementite lamellae, as illustrated in Figure 4-14(f).

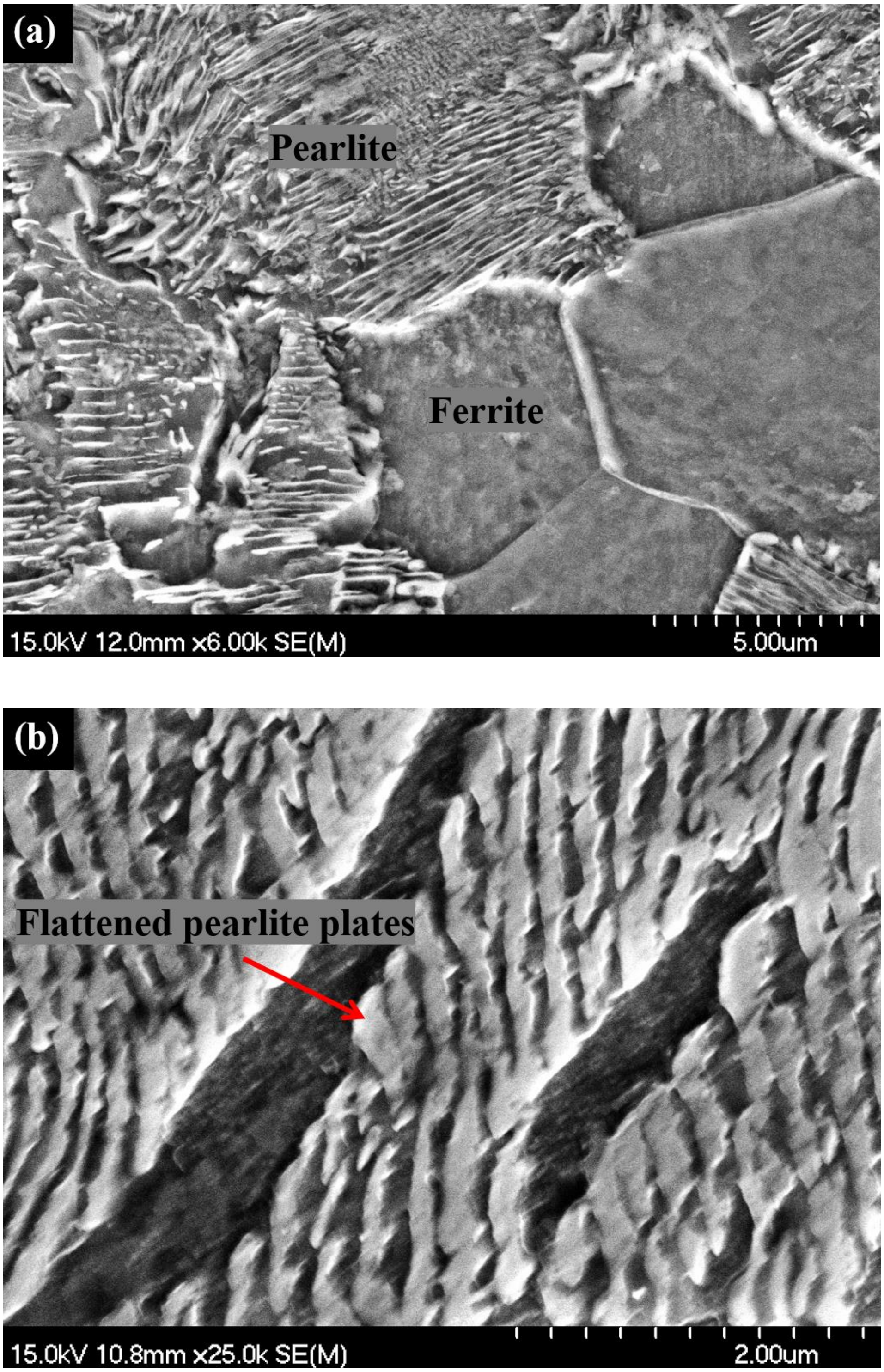

Figure 4-14 SEM close-up image of AISI 1018 steel (a) uniform deformation due to fluid impact and (b) flattened pearlite.

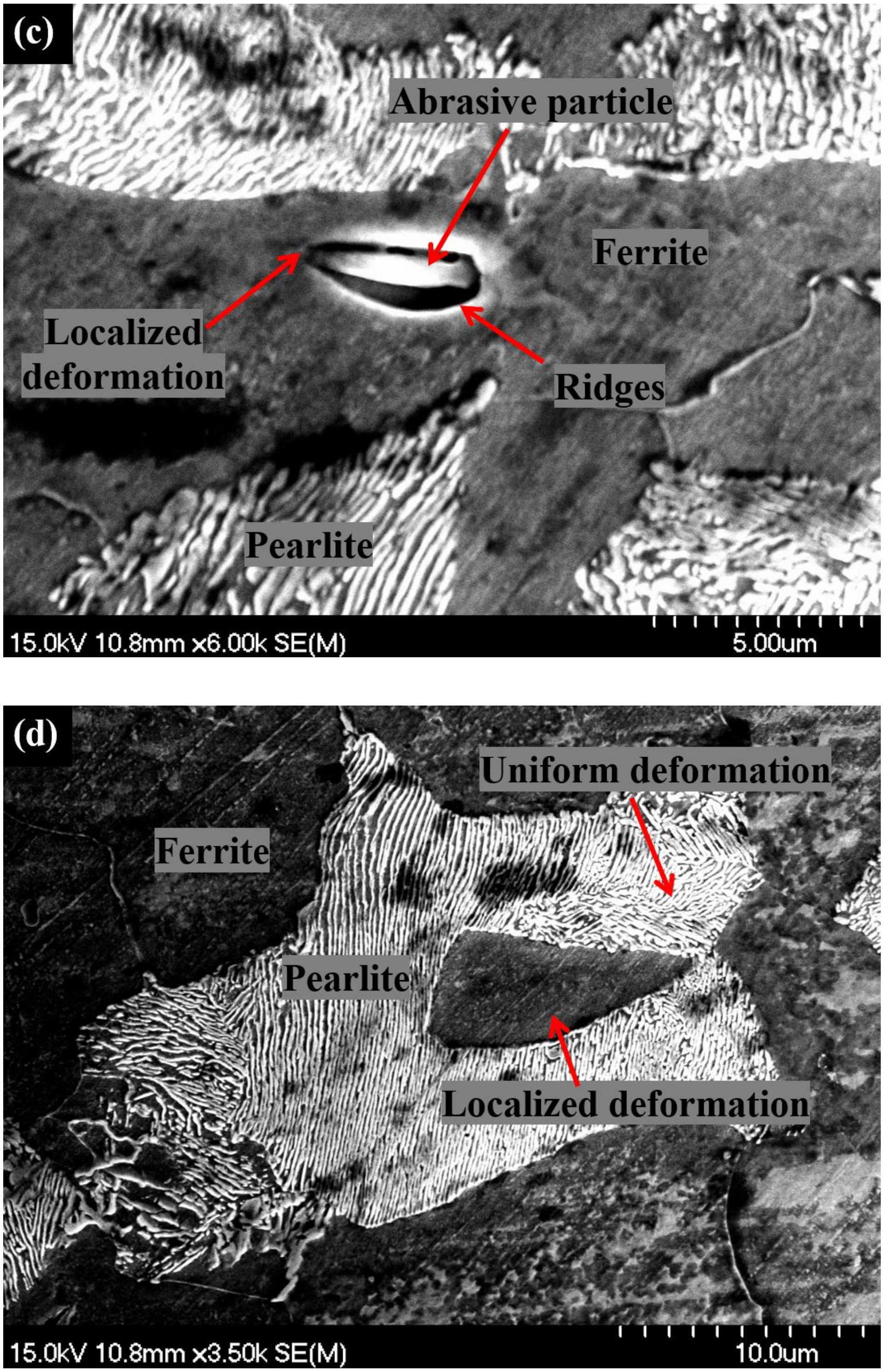

Figure 4-14 SEM close-up image of AISI 1018 steel (c) localized deformation of ferrite and (d) localized deformation of pearlite.

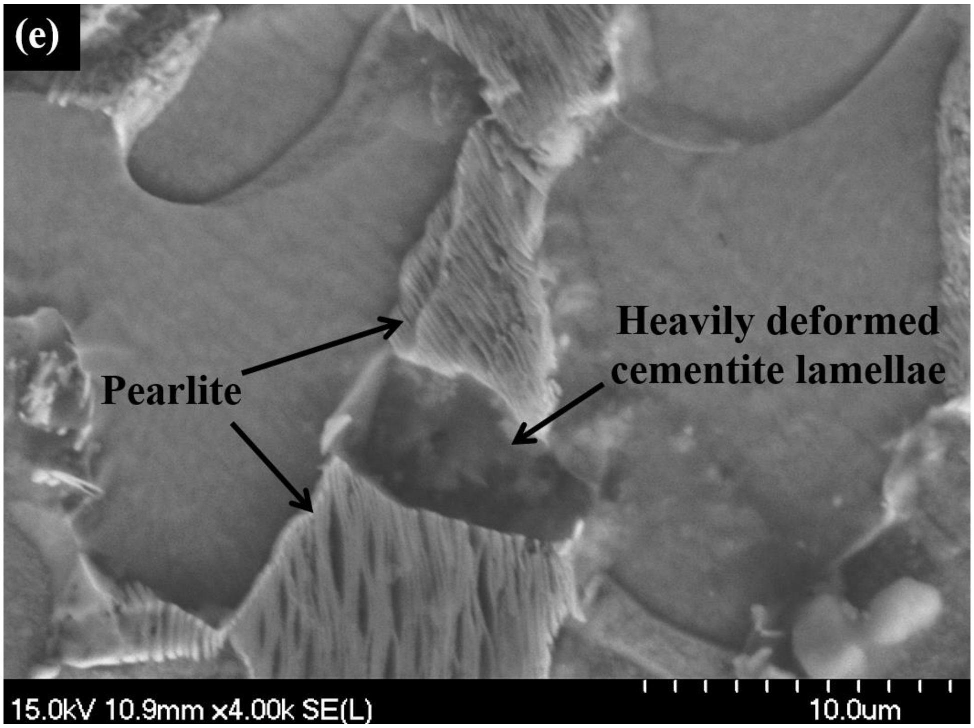

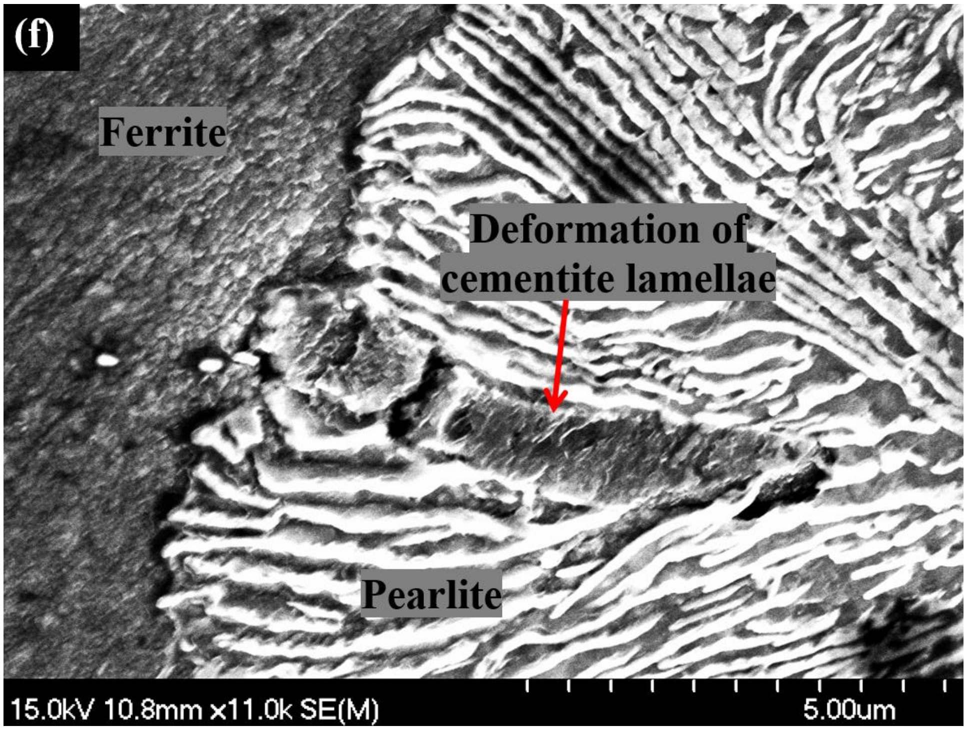

Figure 4-14 SEM close-up image of AISI 1018 steel (e) heavy deformation of cementite lamellae due to particle impact and (f) deformation of cementite lamellae due to penetration of abrasive particle along the interface.

SEM micrographs of cross-sections of eroded surfaces show a different response of ferritic and pearlitic microstructures when subjected to slurry flow (Figure 4-15). When abrasive particles strike ferritic microstructure, severe plastic deformation is induced on the surface. Deformed materials then detached from the surface upon further impact. On the other hand, when abrasive particles strike pearlitic microstructure, pearlitic plates deform ahead of the abrasive particle tip (Figure 4-15(a)). These deformed stack of pearlitic plates resist further deformation. As seen in Figure 4-15 (b), ferrite exhibits more metal removal compared to pearlite. The inset in Figure 4-15(b) is a magnified image of the marked circle to illustrate that ferrite erodes faster than pearlite. During impact of abrasive particles on ferrite, deformed material is squeezed out of the contact zone to the sides and form craters and ridges. Upon repeated impact, the deformed material accumulates on the sides of the crater and piled up over previous layers (Figure 4-15(c)). Figure 4-15(d) is a magnified image of Figure 4-15(c) (marked as circle) and shows accumulation of deformed metal. These layers of displaced metal (ridges) are then removed upon continuous interaction with slurry (liquid + abrasive particles). On the other hand, when an abrasive particle strikes the pearlitic phase, it deforms the cementite lamellae. Figure 4-15(e) shows an abrasive particle as it strikes a pearlitic phase and deforms cementite plates. The deformed pearlitic plates are more visible in Figure 4-15(f). These deformed pearlitic plates absorb the kinetic energy of the abrasive particles and prevent further damage. Delamination of cementite lamellae is also observed underneath the particle impact location (Figure 4-15(f)). Hence, it is clearly evident that pearlite exhibits higher resistance to slurry erosion (by both liquid and abrasive particles) than ferrite.

In summary, ferritic microstructure undergoes severe plastic deformation during slurry erosion. Plastically deformed platelets are then detached by further impact. On the other hand, cementite lamellae of pearlite absorb the kinetic energy and material removal occurs by delamination of cementite lamellae upon further impact (Figure 4-15(f)). At higher slurry velocity, deflected abrasive particles strike the surface at an acute angle and result in microcutting. AISI 1018, API X42 and API

X70 steels consist of ferritic and pearlitic microstructures whereas AISI 1080 steel consists of 100% pearlite. As clearly seen from micrographs, pearlite is more effective in resisting erosion than ferrite. Hence, AISI 1080 steel has higher erosion resistance compared to AISI 1018, API X42 and API X70 steels (Figure 4-1).

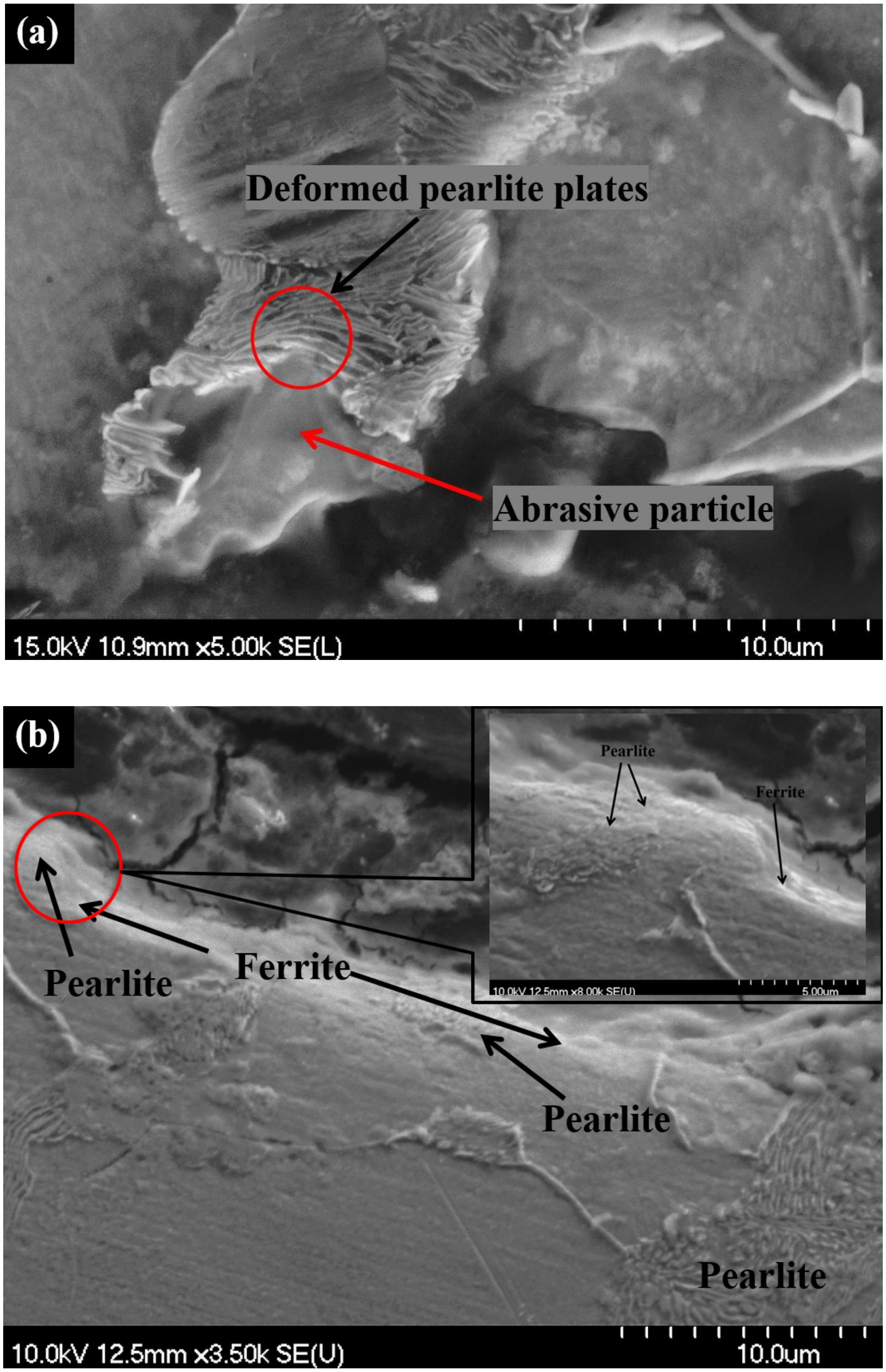

Figure 4-15 SEM micrograph of the cross section of AISI 1018 steel: (a)-(b) different erosion response of ferrite and pearlite.

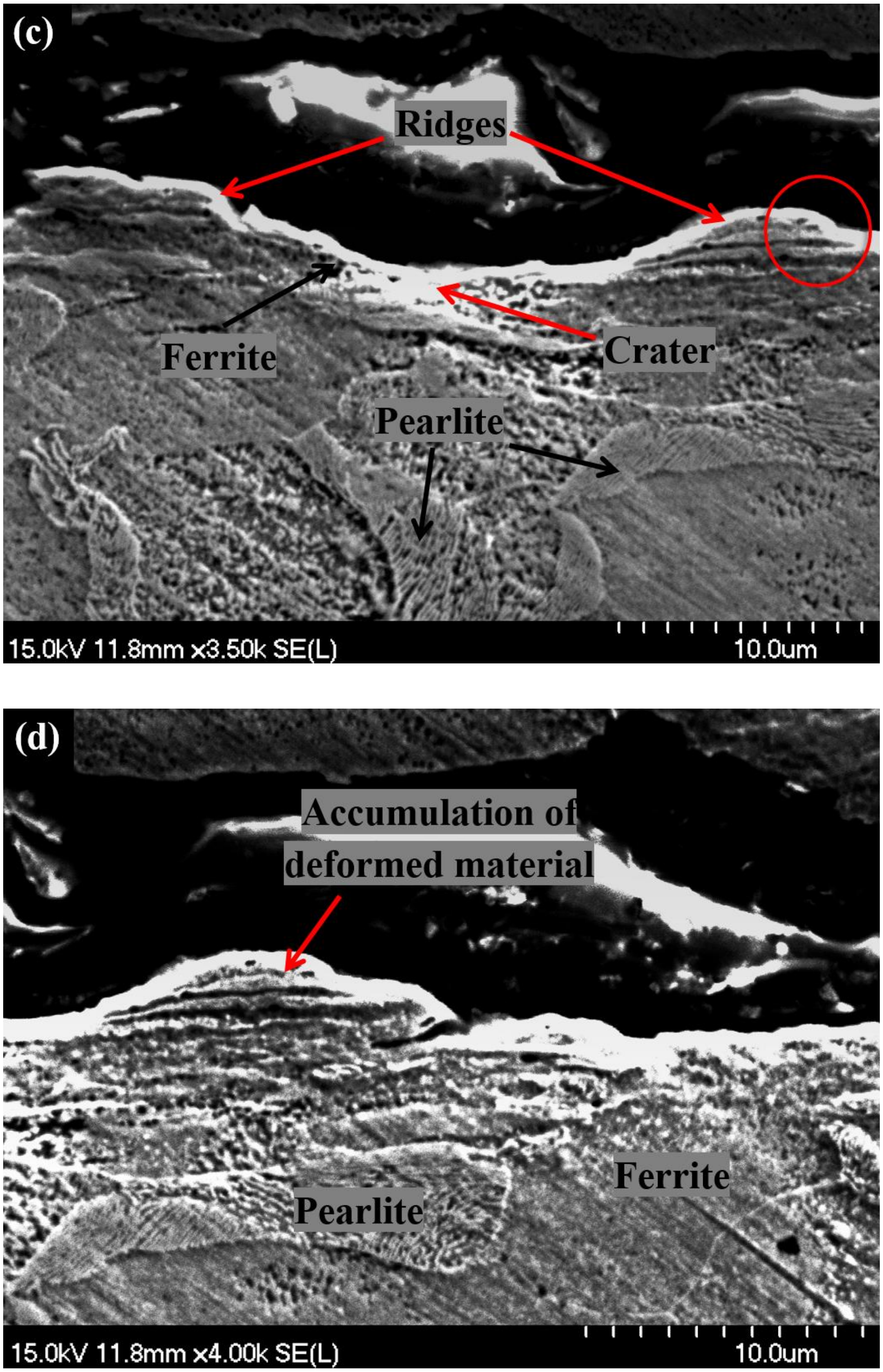

Figure 4-165 SEM micrograph of the cross section of AISI 1018 steel: (c)-(d) accumulation of deformed material in ferrite.

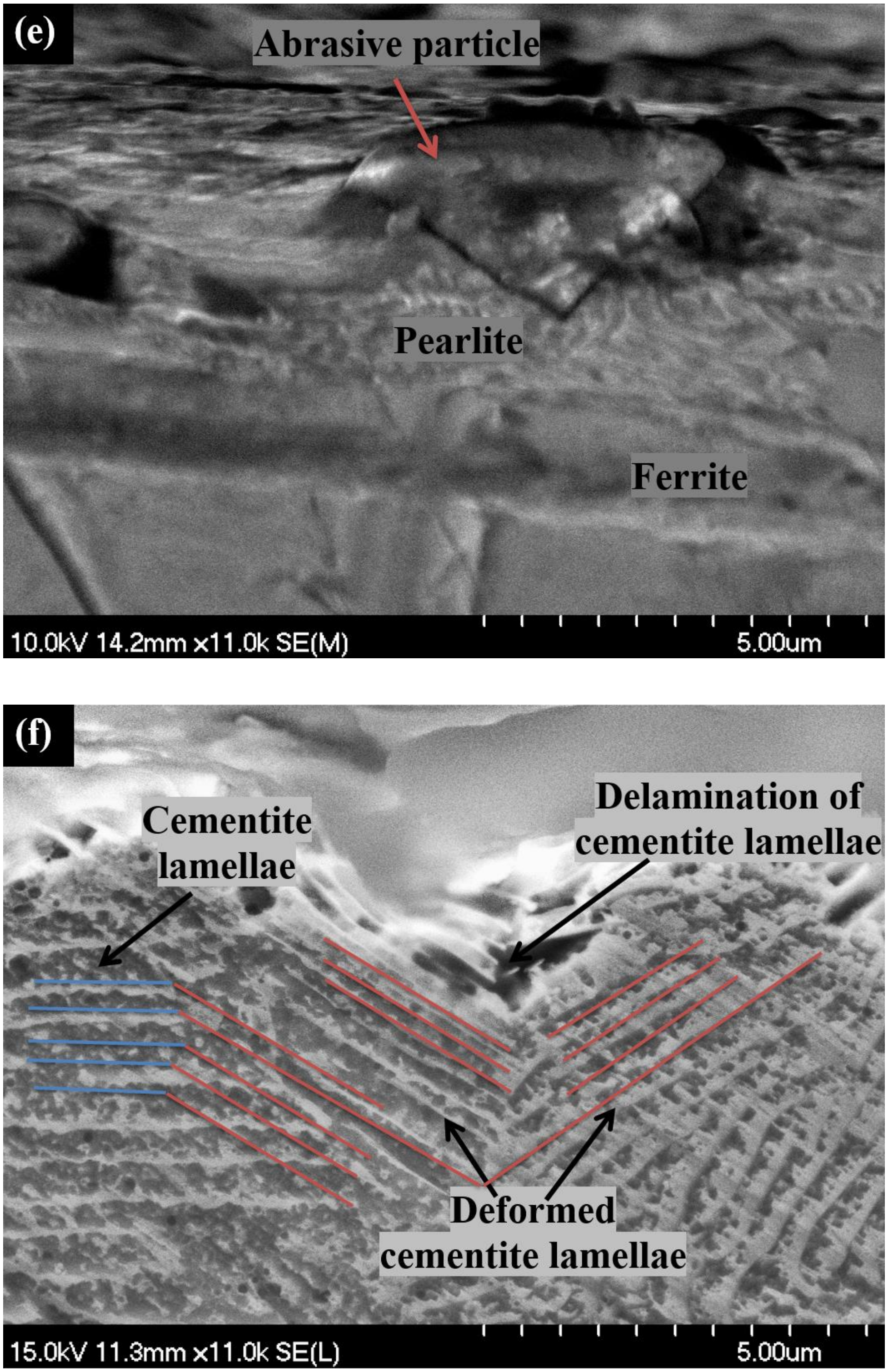

Figure 4-15 SEM micrograph of the cross section of AISI 1018 steel: (e) abrasive particle strike pearlitic phase. And the cross section of AISI 1080 steel: (f) fracture and deformation of cementite lamellae due to abrasive particle impact.

Chapter 5

Conclusions

In this study, a set of erosion tests were performed on various carbon and API X-series pipeline steels in a jet type wet erosion test rig. The impingement angle (90°) was kept constant while altering the slurry velocity (0.20, 0.29, 0.36, 0.43 and 12 m s^{-1}) and the slurry concentration (0, 1, 2, 3, 4 and 5 wt.% slurry). The effect of slurry velocity and concentrations on erosion behavior were thoroughly investigated. Dominant erosion mechanisms were identified by SEM observation. The effects of the steel microstructure on erosion of carbon steels was also studied. The following conclusions can be drawn from the current work:

1. Normalized erosion rate of the steels increases with increasing slurry velocity. This is because of the fact that higher particle velocity has higher kinetic energy, which cause more material removal from the matrix.

2. Normalized erosion rate of the steels increases with increasing slurry concentration. The higher slurry concentration results more particles to material surface collisions. Hence, more material removal occurs with increasing slurry concentration.

3. Due to flow characteristics of slurry, a stagnation zone was created at the center of the eroded profile, and a highly eroded zone was found around the stagnation zone.

4. Abrasive particle of the slurry causes localized erosion while liquid causes uniform erosion to the steel matrix.

5. Heavy plastic deformation and removal of the deformed platelets were found to be the dominant erosion mechanism for AISI 1018, API X42, API X70, API X80, API X100 and API X120 steels. On the other hand, delamination of cementite lamellae is dominant for AISI 1080 steel. In addition, at higher slurry concentration, ploughing and microcutting were observed as erosion mechanism due to cushioning effect.

6. Slurry erosion rate of carbon and low alloy steels decrease with increasing amount of pearlite in the microstructure. Erosion of ferrite and pearlite is controlled by slurry velocity, solid concentration, impacting particle trajectory and microstructural orientation.

7. Pearlitic microstructure exhibits enhanced erosion resistance compared to ferrite at every single erosion condition used in this study due to its lamellar structure, which is more effective in absorbing the impacting particle energy.

8. API X120 and AISI 1080 steel show higher erosion resistance while AISI 1018 steel shows higher erosion rate.

5.1 Contributions

This research is original and expands our knowledge in the area of erosion of carbon steel and API X-series steels used in manufacturing oil and gas transportation pipelines. The contribution of this research work is listed below:

1. The effects of slurry velocity and concentration on erosion behavior were detected.
2. Effectively characterized the eroded profile by identifying different zones.
3. Dominant erosion mechanisms under different environmental conditions were identified.
4. Successfully explored the effect of microstructure on erosion behavior of carbon steel.

It is important to note that the findings of this research have resulted in 3 conference presentations/posters and in the following 4 journal papers:

1. T. Alam and Z. N. Farhat, “Slurry Erosion Surface Damage Under Normal Impact for Piprline Steels,” *ASME*, (2016) (Under Review).

2. T. Alam, M. Aminul Islam, and Z. N. Farhat, “Slurry Erosion of Pipeline Steel: Effect of Velocity and Microstructure,” *ASME*, vol. 138, no. 2, p. 021604, 2015.

3. Islam, Md. Aminul, Alam, Tahrim, Farhat, Z, Mohamed, Adel, Alfantazi, Akram; ‘Effect of Microstructure on the Erosion Behavior of Carbon Steel” *Wear*, 332-333 (2015) 1080–1089.

4. Islam, Md. Aminul, Alam, Tahrim, Farhat, Z; ‘Construction of Erosion Mechanism Maps for Pipeline Steels” *Tribology International*, (2016). (Under Review).

5.2 Recommendations for Future Work

Based on the findings of the present work, the following subjects can be recommended in particular for further studies:

1. Design a new specimen holder for current test rig to alter the impact angle and generate more erosion data covering wider range of particle velocity and impact angle.

2. Develop an erosion mechanism map for a wider range of slurry concentration, impact angle and velocity.

3. Develop a comprehensive erosion model that takes microstructural effects and erosion micro-mechanics into consideration.

References

[1] J. Davidson and R. V. Jewell, “K-sea Transportation,” *United States Securities and Exchange Commission, 2003*, 2003. [Online]. Available: https://www.nasdaq.com/markets/ipos/filing.ashx?filingid=2247105.

[2] D. Furchtgott, “Pipelines Are Safest For Transportation Of Oil And Gas,” *Manhattan Institute*, 2003. .

[3] C. J. Trench, “How Pipelines Make the Oil Market Work,” *Allegro Energy Gr.*, no. December, pp. 1–22, 2001.

[4] “The World Factbook,” *CIA Library*, 2014. [Online]. Available: https://www.cia.gov/library/publications/the-world-factbook/fields/2117.html.

[5] D. Furchtgott, “Pipelines Are Safest For Transportation Of Oil And Gas,” *Manhattan Institute*, 2003. .

[6] A. C. on C. and A. Steels, *ASM Metals Handbook*, 9th ed. American Society for Metals, 1980.

[7] H.-G. Hillenbrand, M. Graf, and C. Kalwa, “Development and production of high strength pipeline steels,” *Int. Symp. Niobium 2001*, 2001.

[8] J. Gray, “Niobium bearing steels in pipeline projects,” *Proc. Int. Symp. Niobium*, 2001.

[9] R. M. Andrews and A. D. Batte, “Developments in fracture control technology for gas pipelines utilising high strength steels.,” *Korean Gas Union*, pp. 1–11, 2011.

[10] A. K. JHA, R. BATHAM, M. AHMED, A. K. MAJUMDER, O. P. MODI, S. CHATURVEDI, and A. K. GUPTA, “Effect of impinging angle and rotating speed on erosion behavior of aluminum,” *Trans. Nonferrous Met. Soc. China*, vol. 21, no. 1, pp. 32–38, Jan. 2011.

[11] A. J. S. Steward, N. R., & Spearing, “Combating Pipeline Wear--an Advancing Technology,” *J. South African Inst. Min. Metall. Africa)*, vol. 92, no. 6, pp. 149–157, 1992.

[12] T. Ross and N. Lott, "Billion Dollar U.S. Weather Disasters, 1980–2001," *National Climatic Data Center*, 2001. [Online]. Available: http://www.infoplease.com/ipa/A0882823.html.

[13] and J. H. P. G.H. Koch, M.P. Brongers, N.G. Thompson, P. Virmani, "Corrosion Cost and Preventative Strategies in the United States," *NACE Int.*, no. March, 2002.

[14] U. S. N. P. Plants, "Erosion / Corrosion-Induced Pipe Wall Thinning in DO NOT MICROFILM."

[15] SAE, "Carbon and Alloy Steels," *SAE International*, 2015. .

[16] SAE, "Carbon Steel, Sheet, Strip, and Plate, (SAE 1020 and 1025), Annealed," *SAE International*, 2012. .

[17] SAE, "Carburizing, Carbon and Low-Alloy Steel Parts," *SAE International*, 2013. .

[18] SAE, "Chemical Compositions of SAE Wrought Stainless Steels," *SAE International*, 1998. .

[19] P. Cunat, "Stainless Steel In Structural Automotive Applications," *SAE Tech. Pap.*, pp. 1–10, 2002.

[20] R. J. K. Wood, "Erosion–corrosion interactions and their effect on marine and offshore materials," *Wear*, vol. 261, no. 9, pp. 1012–1023, Nov. 2006.

[21] P. Santacreu, J. Glez, N. Roulet, and T. Fröhlich, "Austenitic Stainless Steels For Automotive Structural Parts," *SAE Tech. Pap.*, pp. 1–8, 2006.

[22] S. H. Avner, *Introduction to physical metallurgy*. McGraw-Hill, 1964.

[23] ISO, "Carbon steel tubes suitable for screwing," *Int. Organ. Stand.*, vol. 65, pp. 1–3, 1981.

[24] ISO, "Hot-rolled steel sections - Part 1: Equal-leg angles - Dimensions," *Int. Organ. Stand.*, vol. 657–1, pp. 1–4, 1989.

[25] ISO, "Hot-rolled steel sections - Part 2: Unequal-leg angles - Dimensions," *Int. Organ. Stand.*, vol. 657–2, pp. 1–5, 1989.

[26] ISO, "Mechanical properties of fasteners made of carbon steel and alloy steel -- Part 1: Bolts, screws and studs with specified property classes - Coarse thread and fine pitch thread," *Int. Organ. Stand.*, vol. 898–1, pp. 1–57, 2013.

[27] ISO, “Mechanical properties of fasteners made of carbon steel and alloy steel - Part 2: Nuts with specified property classes - Coarse thread and fine pitch thread,” *Int. Organ. Stand.*, vol. 898–2, pp. 1–21, 2012.

[28] ISO, “Stainless steel clamp pipe couplings for the food industry,” *Int. Organ. Stand.*, vol. 2852, pp. 1–12, 1993.

[29] ISO, “Classification of steels into unalloyed and alloy steels based on chemical composition,” *Int. Organ. Stand.*, pp. 1–2, 1982.

[30] ISO, “Preparation of steel substrates before application of paints and related products - Visual assessment of surface cleanliness - Part 1: Rust grades and preparation grades of uncoated steel substrates and of steel substrates after overal,” *Int. Organ. Stand.*, vol. 8501–1, pp. 1–74, 2007.

[31] ISO, “Mechanical properties of corrosion-resistant stainless steel fasteners - Part 1: Bolts, screws and studs,” *Int. Organ. Stand.*, vol. 3506–1, pp. 1–27, 2009.

[32] S. W. Thompson, D. J. Colvin, and G. Krauss, “Continuous Cooling transformatios and Microstructures in Low-carbon, High-Strength Low Alloy Plate Steel,” *Metall. Trans. A*, vol. 21A, pp. 1493–1497, 1990.

[33] W.-S. Lee and T.-T. Su, “Mechanical properties and microstructural features of AISI 4340 high-strength alloy steel under quenched and tempered conditions,” *J. Mater. Process. Technol.*, vol. 87, no. 1–3, pp. 198–206, Mar. 1999.

[34] B. Hirosh, N. Yamada, and H. Matsuda, “Effect of the Thermo-Mechnical control process on the properties of hig hstrength low alloy steel,” *Trans. ISIJ*, vol. 25, no. 54, pp. 54–61, 1985.

[35] C. L. Davis and J. E. King, “Effect of cooling rate on intercritically reheated microstructure and toughness in high strength low alloy steel,” *Mater. Sci. Technol.*, vol. 9, no. 1, pp. 8–15, Jan. 1993.

[36] F. B. Pickering, “High Strength Low Alloy Steels,” in *Materials Science and Technology*, Wiley-VCH Verlag GmbH & Co. KGaA, 2006.

[37] C. Y. Chen, H. W. Yen, F. H. Kao, W. C. Li, C. Y. Huang, J. R. Yang, and S. H. Wang, “Precipitation hardening of high-strength low-alloy steels by nanometer-sized carbides,” *Mater. Sci. Eng. A*, vol. 499, no. 1–2, pp. 162–166, Jan. 2009.

[38] V. Stephanie, “Control of the Non-Recrystallization Temperature in High Strength Low Alloy (HSLA) Steels,” Ghent University, 2010.

[39] H. G. Hillenbrand, A. Liessem, K. Bierman, C. J. Heckman, and V. Schwinn, "Development of high strength material and pipe production technology for grade X120 line pipe," in *2004 International Pipeline Conference*, 2004, pp. 1743–1749.

[40] H. . Hillenbrand, A. Liessem, C. Kalwa, M. Erdelen-Peppler, and C. Stallybrass, "Technological solutions for high strength gas pipelines.," in *1st International Conference on Super-High Strength Steels*, 2008, pp. 1–16.

[41] D. A. Skobir, "High-Strength Low-Alloy (Hsla) Steels," *Mater. Technol.*, vol. 45, no. 4, pp. 295–301, 2011.

[42] J. T. Black and R. A. Kohser, *Degarmo's Materials and Processes in Manufacturing*, 11 th. Wiley, 2011.

[43] D. G. Stalheim and G. Muralidharan, "The Role of Continuous Cooling Transformation Diagrams in Material Design for High Strength Oil and Gas Transmission Pipeline Steels," in *International Pipeline Conference*, 2006.

[44] M. Shome and O. N. Mohanty, "Continuous cooling transformation diagrams applicable to the heat-affected zone of HSLA-80 and HSLA-100 steels," *Metall. Mater. Trans. A Phys. Metall. Mater. Sci.*, vol. 37, no. 7, pp. 2159–2169, 2006.

[45] J. T. Mcgrath, J. A. Gianetto, and R. F. Orr, "Microstructure / Mechanical Property Relationships of Submerged Arc Welds in HSLA 80 Steel," in *Welding Research Supplement*, 1989, pp. 112–120.

[46] P. A. Peters and H. G. Hillendbrand, "Experience in Supply of Arctic Grdae Line Pipe for Soviet Construction Projects," in *World Materials Congress*, 1988.

[47] W. F. Smith, *Structure and Properties of Engineering Alloys*, 2nd ed. McGraw-Hill, 1993.

[48] H. G. Hillenbrand and P. Schwaab, "Quantitative determination of the microstructure of high strength structural steels for correlation with their mechanical properties," *Mater. Sci. Eng.*, vol. 94, pp. 71–78, Oct. 1987.

[49] D. B. Rosado, W. D. Waele, D. Vanderschueren, and S. Hertelé, "Latest developments in mechanical properties and metallurgical features of high strength line pipe steels," *Int. J. Sustain. Constr. Des.*, vol. 4, no. 1, p. 10, 2013.

[50] H. Asahi, N. R. V Bangaru, T. Hara, J. Koo, M. J. Luton, C. W. Petersen, H. Tamehiro, and Y. Terada, "Ultra-high strength, weldable steels with excellent ultra-low temperature toughness," May-1999.

[51] A. Liessem, G. Knauf, and S. Zimmermann, “Strain Based Design—What the Contribution of a Pipe Manufacturer Can Be,” in *The Seventeenth International Offshore and Polar Engineering Conference*, 2007.

[52] A. Neville and T. Hodgkiess, “Study of effect of liquid corrosivity in liquid-solid impingement on cast iron and austenitic stainless steel,” *Br. Corros. J.*, vol. 32, no. 3, pp. 197–205, 1997.

[53] D. J. O’Flynn, M. S. Bingley, M. S. A. Bradley, and A. J. Burnett, “A model to predict the solid particle erosion rate of metals and its assessment using heat-treated steels,” *Wear*, vol. 248, no. 1–2, pp. 162–177, Mar. 2001.

[54] J. R. Laguna-Camacho, A. Marquina-Chávez, J. V. Méndez-Méndez, M. Vite-Torres, and E. A. Gallardo-Hernández, “Solid particle erosion of AISI 304, 316 and 420 stainless steels,” *Wear*, vol. 301, no. 1–2, pp. 398–405, Apr. 2013.

[55] T. H. MCCLOSKEY and C. BELLANCA, “Minimizing solid particle erosion in power plant steam turbines,” *Power Eng.*, vol. 93, no. 8, pp. 35–38.

[56] M. Matsumura, Y. Oka, H. Hiura, and M. Yano, “The role of passivating film in preventing slurry erosion-corrosion of austenitic stainless steel.,” *ISIJ Int.*, vol. 31, no. 2, pp. 168–176, 1991.

[57] Y. I. Oka, K. Okamura, and T. Yoshida, “Practical estimation of erosion damage caused by solid particle impact,” *Wear*, vol. 259, no. 1–6, pp. 95–101, Jul. 2005.

[58] J. I. Ukpai, R. Barker, X. Hu, and A. Neville, “Exploring the erosive wear of X65 carbon steel by acoustic emission method,” *Wear*, vol. 301, no. 1–2, pp. 370–382, Apr. 2013.

[59] Y. I. Oka, S. Mihara, and T. Yoshida, “Impact-angle dependence and estimation of erosion damage to ceramic materials caused by solid particle impact,” *Wear*, vol. 267, no. 1–4, pp. 129–135, Jun. 2009.

[60] H. S. Grewal, H. Singh, and A. Agrawal, “Understanding Liquid Impingement erosion behaviour of nickel–alumina based thermal spray coatings,” *Wear*, vol. 301, no. 1–2, pp. 424–433, Apr. 2013.

[61] R. G. Rateick, K. R. Karasek, A. J. Cunningham, K. C. Goretta, and J. L. Routbort, “Solid-particle erosion of tungsten carbide/cobalt cermet and hardened 440C stainless steel—A comparison,” *Wear*, vol. 261, no. 7–8, pp. 773–778, Oct. 2006.

[62] M. Vite-Torres, J. R. Laguna-Camacho, R. E. Baldenebro-Castillo, E. A. Gallardo-Hernández, E. E. Vera-Cárdenas, and J. Vite-Torres, "Study of solid particle erosion on AISI 420 stainless steel using angular silicon carbide and steel round grit particles," *Wear*, vol. 301, no. 1–2, pp. 383–389, Apr. 2013.

[63] A. V. Levy and G. Hickey, "Liquid-solid particle slurry erosion of steels," *Wear*, vol. 117, no. 2, pp. 129–146, Jun. 1987.

[64] K. Jordan, "Erosion in Multiphase Production of Oil and Gas," 1998.

[65] E. F. McLaury, B.S., Shirazi, S.A., Shadley, J.R., & Rybicki, "How operating and environmental conditions affect erosion," 1999.

[66] B. McLaury and S. Shirazi, "Generalization of API RP 14E for erosive service in multiphase production," *SPE Annu. Tech. Conf. Exhib.*, pp. 423–432, 1999.

[67] H. . Lin, S. . Wu, and C. . Yeh, "A comparison of slurry erosion characteristics of TiNi shape memory alloys and SUS304 stainless steel," *Wear*, vol. 249, no. 7, pp. 557–565, Jul. 2001.

[68] J. G. A. Bitter, "A study of erosion phenomena," *Wear*, vol. 6, no. 3, pp. 169–190, May 1963.

[69] H. M. Clark and K. K. Wong, "Impact angle, particle energy and mass loss in erosion by dilute slurries," *Wear*, vol. 186–187, pp. 454–464, Aug. 1995.

[70] X. Chen, B. S. McLaury, and S. A. Shirazi, "Application and experimental validation of a computational fluid dynamics (CFD)-based erosion prediction model in elbows and plugged tees," *Comput. Fluids*, vol. 33, no. 10, pp. 1251–1272, Dec. 2004.

[71] J. A. . Humphrey, "Fundamentals of fluid motion in erosion by solid particle impact," *Int. J. Heat Fluid Flow*, vol. 11, no. 3, pp. 170–195, Sep. 1990.

[72] H. M. Clark, "The influence of the flow field in slurry erosion," *Wear*, vol. 152, no. 2, pp. 223–240, Jan. 1992.

[73] H. M. Clark and R. B. Hartwich, "A re-examination of the 'particle size effect' in slurry erosion," *Wear*, vol. 248, no. 1–2, pp. 147–161, Mar. 2001.

[74] J. B. Zu, I. M. Hutchings, and G. T. Burstein, "Design of a slurry erosion test rig," *Wear*, vol. 140, no. 2, pp. 331–344, Nov. 1990.

[75] A. V. Levy, J. Yan, and V. D. Arora, "Sand-water slurry erosion of carburized AISI 8620 steel," *Wear*, vol. 101, no. 2, pp. 117–126, Jan. 1985.

[76] B. S. McLaury and S. A. Shirazi, "An Alternate Method to API RP 14E for Predicting Solids Erosion in Multiphase Flow," *J. Energy Resour. Technol.*, vol. 122, no. 3, pp. 115–122, May 2000.

[77] M. A. Islam, T. Alam, Z. N. Farhat, A. Mohamed, and A. Alfantazi, "Effect of microstructure on the erosion behavior of carbon steel," *Wear*, vol. 332–333, pp. 1080–1089, May 2015.

[78] Q. H. Mazumder, S. A. Shirazi, B. S. McLaury, J. R. Shadley, and E. F. Rybicki, "Development and validation of a mechanistic model to predict solid particle erosion in multiphase flow," *Wear*, vol. 259, no. 1–6, pp. 203–207, Jul. 2005.

[79] G. R. Desale, B. K. Gandhi, and S. C. Jain, "Slurry erosion of ductile materials under normal impact condition," *Wear*, vol. 264, no. 3–4, pp. 322–330, Feb. 2008.

[80] G. R. Desale, B. K. Gandhi, and S. C. Jain, "Improvement in the design of a pot tester to simulate erosion wear due to solid–liquid mixture," *Wear*, vol. 259, no. 1–6, pp. 196–202, Jul. 2005.

[81] G. R. Desale, B. K. Gandhi, and S. C. Jain, "Effect of erodent properties on erosion wear of ductile type materials," *Wear*, vol. 261, no. 7–8, pp. 914–921, Oct. 2006.

[82] A. A. C. Recco, D. López, A. F. Bevilacqua, F. da Silva, and A. P. Tschiptschin, "Improvement of the slurry erosion resistance of an austenitic stainless steel with combinations of surface treatments: Nitriding and TiN coating," *Surf. Coatings Technol.*, vol. 202, no. 4–7, pp. 993–997, Dec. 2007.

[83] M. A. Al-Bukhaiti, S. M. Ahmed, F. M. F. Badran, and K. M. Emara, "Effect of impingement angle on slurry erosion behaviour and mechanisms of 1017 steel and high-chromium white cast iron," *Wear*, vol. 262, no. 9–10, pp. 1187–1198, Apr. 2007.

[84] G. T. Burstein and K. Sasaki, "Effect of impact angle on the slurry erosion–corrosion of 304L stainless steel," *Wear*, vol. 240, no. 1–2, pp. 80–94, May 2000.

[85] R. Bellman and A. Levy, "Erosion mechanism in ductile metals," *Wear*, vol. 70, no. 1, pp. 1–27, Jul. 1981.

[86] R. J. Llewellyn, S. K. Yick, and K. F. Dolman, "Scouring erosion resistance of metallic materials used in slurry pump service," *Wear*, vol. 256, no. 6, pp. 592–599, Mar. 2004.

[87] R. . Wellman and J. . Nicholls, “High temperature erosion–oxidation mechanisms, maps and models,” *Wear*, vol. 256, no. 9–10, pp. 907–917, May 2004.

[88] R. Hamzah, D. J. Stephenson, and J. E. Strutt, “Erosion of material used in petroleum production,” *Wear*, vol. 186–187, pp. 493–496, Aug. 1995.

[89] K. Haugen, O. Kvernvold, A. Ronold, and R. Sandberg, “Sand erosion of wear-resistant materials: Erosion in choke valves,” *Wear*, vol. 186–187, pp. 179–188, Jul. 1995.

[90] H. M. Shalaby, W. T. Riad, A. A. Alhazza, and M. H. Behbehani, “Failure analysis of fuel supply pipeline,” *Eng. Fail. Anal.*, vol. 13, no. 5, pp. 789–796, Jul. 2006.

[91] Y. P. Wang, D. Y. Li, L. Parent, and H. Tian, “Performances of hybrid high-entropy high-Cr cast irons during sliding wear and air-jet solid-particle erosion,” *Wear*, vol. 301, no. 1–2, pp. 390–397, Apr. 2013.

[92] R. Mohsin, Z. A. Majid, and M. Z. Yusof, “Multiple failures of API 5L X42 natural gas pipe: Experimental and computational analysis,” *Eng. Fail. Anal.*, vol. 34, pp. 10–23, Dec. 2013.

[93] Z. A. Majid, R. Mohsin, Z. Yaacob, and Z. Hassan, “Failure analysis of natural gas pipes,” *Eng. Fail. Anal.*, vol. 17, no. 4, pp. 818–837, Jun. 2010.

[94] J. L. F. Freire, R. D. Vieira, and a. C. Benjamin, “Part 2: Experimental Strain Analysis of Metal Loss Defects in Pipeline,” *Exp. Tech.*, vol. 30, no. 5, pp. 42–47, 2006.

[95] I. Finnie, G. R. Stevick, and J. R. Ridgely, “The influence of impingement angle on the erosion of ductile metals by angular abrasive particles,” *Wear*, vol. 152, no. 1, pp. 91–98, Jan. 1992.

[96] G. W. Stachwick and A. W. Batchelor, *Engineering tribology*, 2nd ed. Boston: Butterworth-Heinemann, 2001.

[97] R. S. Lynn, K. K. Wong, and H. M. Clark, “On the particle size effect in slurry erosion,” *Wear*, vol. 149, no. 1–2, pp. 55–71, Sep. 1991.

[98] A. Misra and I. Finnie, “On the size effect in abrasive and erosive wear,” *Wear*, vol. 65, no. 3, pp. 359–373, Jan. 1981.

[99] S. Bahadur and R. Badruddin, “Erodent particle characterization and the effect of particle size and shape on erosion,” *Wear*, vol. 138, no. 1–2, pp. 189–208, Jun. 1990.

[100] H. M. Clark, “Particle velocity and size effects in laboratory slurry erosion measurements OR… do you know what your particles are doing?,” *Tribol. Int.*, vol. 35, no. 10, pp. 617–624, Oct. 2002.

[101] B. . Gandhi, S. . Singh, and V. Seshadri, “Study of the parametric dependence of erosion wear for the parallel flow of solid–liquid mixtures,” *Tribol. Int.*, vol. 32, no. 5, pp. 275–282, Apr. 1999.

[102] R. Gupta, S. N. Singh, and V. Sehadri, “Prediction of uneven wear in a slurry pipeline on the basis of measurements in a pot tester,” *Wear*, vol. 184, no. 2, pp. 169–178, May 1995.

[103] A. V. Levy and P. Yau, “Erosion of steels in liquid slurries,” *Wear*, vol. 98, pp. 163–182, Nov. 1984.

[104] A. V. Levy, N. Jee, and P. Yau, “Erosion of steels in coal-solvent slurries,” *Wear*, vol. 117, no. 2, pp. 115–127, Jun. 1987.

[105] R. Cooke, “Pipeline material evaluation for the Mina Grande hydrohoist system,” 1996, pp. 455–478.

[106] K. K. Wong and H. M. Clark, “A model of particle velocities and trajectories in a slurry pot erosion tester,” *Wear*, vol. 160, no. 1, pp. 95–104, Jan. 1993.

[107] R. J. K. Wood, T. F. Jones, J. Ganeshalingam, and N. J. Miles, “Comparison of predicted and experimental erosion estimates in slurry ducts,” *Wear*, vol. 256, no. 9–10, pp. 937–947, May 2004.

[108] L. Fuyan and S. Hesheng, “The effect of impingement angle on slurry erosion,” *Wear*, vol. 141, no. 2, pp. 279–289, Jan. 1991.

[109] and A. W. J. D. G. De Bree, S. E. M., W. F. Rosenbrand, “On the erosion resistance in water-sand mixtures of steels for application in slurry pipelines,” in *8th International Conference on Hydraulic Transport of Solids in Pipes,BHRA Fluid Eng., Johannesburg, South Africa*, 1982.

[110] V. Bhandari, S., Singh, H., Kansal, H. K., & Rastogi, “Slurry erosion studies of hydroturbine steels under hydroaccelerated conditions,” *Proc. Inst. Mech. Eng. Part J J. Eng. Tribol.*, 2011.

[111] V. Bhandari, S., Singh, H., Kumar, H., & Rastogi, “Slurry erosion performance study of detonation gun-sprayed WC-10Co-4Cr coatings on CF8M steel under hydro-accelerated conditions,” *J. Therm. spray Technol.*, vol. 21, no. 5, pp. 1054–1064, 2012.

[112] J. Postlethwaite and S. Nesic, "Erosion in Disturbed Liquid/Particle Pipe Flow: Effects of Flow Geometry and Particle Surface Roughness," 1993, p. Vol. 49, No. 10, pp. 850–857.

[113] M. M. Salama, "An Alternative to API 14E Erosional Velocity Limits for Sand-Laden Fluids," *J. Energy Resour. Technol.*, vol. 122, no. 2, p. 71, 2000.

[114] R. C. Stack, M. M., Zhou, S., & Newman, "Effects of particle velocity and applied potential on erosion of mild steel in carbonate/bicarbonate slurry," *Mater. Sci. Technol.*, vol. 12, no. 3, pp. 261–268, 1996.

[115] D. López, J. P. Congote, J. R. Cano, A. Toro, and A. P. Tschiptschin, "Effect of particle velocity and impact angle on the corrosion–erosion of AISI 304 and AISI 420 stainless steels," *Wear*, vol. 259, no. 1–6, pp. 118–124, Jul. 2005.

[116] I. Finnie, "Erosion of surfaces by solid particles," *Wear*, vol. 3, no. 2, pp. 87–103, Mar. 1960.

[117] G. P. Tilly, "A two stage mechanism of ductile erosion," *Wear*, vol. 23, no. 1, pp. 87–96, Jan. 1973.

[118] A. N. J. Stevenson and I. M. Hutchings, "Scaling laws for particle velocity in the gas-blast erosion test," *Wear*, vol. 181–183, pp. 56–62, Feb. 1995.

[119] J. F. Molinari and M. Ortiz, "A study of solid-particle erosion of metallic targets," *Int. J. Impact Eng.*, vol. 27, no. 4, pp. 347–358, Apr. 2002.

[120] J. . Mbabazi, T. . Sheer, and R. Shandu, "A model to predict erosion on mild steel surfaces impacted by boiler fly ash particles," *Wear*, vol. 257, no. 5–6, pp. 612–624, Sep. 2004.

[121] E. Akbarzadeh, E. Elsaadawy, A. M. Sherik, J. K. Spelt, and M. Papini, "The solid particle erosion of 12 metals using magnetite erodent," *Wear*, vol. 282–283, pp. 40–51, Apr. 2012.

[122] M. A. Islam and Z. N. Farhat, "Effect of impact angle and velocity on erosion of API X42 pipeline steel under high abrasive feed rate," *Wear*, vol. 311, no. 1–2, pp. 180–190, Mar. 2014.

[123] P. Blau, *Friction, Lubrication, and Wear Technology*, vol. 18. ASM International, 1992.

[124] D. Vigolo, I. M. Griffiths, S. Radl, and H. a. Stone, "An experimental and theoretical investigation of particle–wall impacts in a T-junction," *J. Fluid Mech.*, vol. 727, pp. 236–255, 2012.

[125] I. M. Hutchings, “Wear by particulates,” *Chem. Eng. Sci.*, vol. 42, no. 4, pp. 869–878, Jan. 1987.

[126] A. Mansouri, H. Arabnejad, S. A. Shirazi, and B. S. McLaury, “A combined CFD/experimental methodology for erosion prediction,” *Wear*, vol. 332–333, pp. 1090–1097, May 2015.

[127] H. M. Clark, “On the impact rate and impact energy of particles in a slurry pot erosion tester,” *Wear*, vol. 147, no. 1, pp. 165–183, Jul. 1991.

[128] P. G. Shewmon, “Particle size threshold in the erosion of metals,” *Wear*, vol. 68, no. 2, pp. 253–258, May 1981.

[129] I. M. Hutchings, *Tribology - Friction and wear of engineering materials*. Edward Arnold, UK, 1992.

[130] A. Levy and P. Chik, “The effects of erodent composition and shape on the erosion of steel,” *Wear*, vol. 89, no. 2, pp. 151–162, Aug. 1983.

[131] I. M. Hutchings, “A model for the erosion of metals by spherical particles at normal incidence,” *Wear*, vol. 70, no. 3, pp. 269–281, Aug. 1981.

[132] I. Finnie, “The Mechanism of Erosion of Ductile Metals,” in *3rd U.S. Nat. Congress of Applied Mechanics*, 1958, pp. 527–532.

[133] I. M. Hutchings, R. E. Winter, and J. E. Field, “Solid particle erosion of metals: the removal of surface material by spherical projectiles,” in *Proceedings of the Royal Society of London A: Mathematical, Physical and Engineering Sciences*, 1976, vol. 348, no. 1654, pp. 379–392.

[134] D. G. Rickerby and N. H. MacMillan, “Erosion of Aluminum and Magnesium Oxide by Spherical Particles,” in *Wear of Materials*, 1981, pp. 548–563.

[135] D. G. Rickerby and N. H. Macmillan, “On the oblique impact of a rigid sphere against a rigid-plastic solid,” *Int. J. Mech. Sci.*, vol. 22, no. 8, pp. 491–494, Jan. 1980.

[136] I. M. Hutchings, N. H. Macmillan, and D. G. Rickerby, “Further studies of the oblique impact of a hard sphere against a ductile solid,” *Int. J. Mech. Sci.*, vol. 23, no. 11, pp. 639–646, Jan. 1981.

[137] N. Gane, “The direct measurement of the strength of metals on a sub-micrometre scale,” in *Proceedings of the Royal Society of London A: Mathematical, Physical and Engineering Sciences*, 1970, vol. 317, no. 1530, pp. 367–391.

[138] N. Gane and J. M. Cox, "The micro-hardness of metals at very low loads," *Philos. Mag.*, vol. 22, no. 179, pp. 881–891, 1970.

[139] G. W. Stachowiak, "Particle angularity and its relationship to abrasive and erosive wear," *Wear*, vol. 241, no. 2, pp. 214–219, Jul. 2000.

[140] M. Roy, Y. Tirupataiah, and G. Sundararajan, "Effect of particle shape on the erosion of Cu and its alloys," *Mater. Sci. Eng. A*, vol. 165, no. 1, pp. 51–63, Jun. 1993.

[141] J. Salik and D. Buckley, "Effects of Erodent Particle Shape and Various Heat Treatments on Erosion Resistance of Plain Carbon Steel," in *NASA Technical Paper*, 1981.

[142] R. Brown, E. J. Jun, and J. W. Edington, "Mechanisms of Erosive Wear for 90° Impact on Copper and Iron Targets," in *Wear of Materials*, 1981, pp. 583–591.

[143] J. Maji and G. L. Sheldon, "Mechanisms of Erosion of a Ductile Material by Solid Particles," in *Erosion: Prevention and Useful Applications*, 1979, pp. 136–147.

[144] A. A. Torrance, "An explanation of the hardness differential needed for abrasion," *Wear*, vol. 68, no. 2, pp. 263–266, May 1981.

[145] K. Wellinger and H. Uetz, "Gleit-, Spül- und strahlverschleiss-prüfung," *Wear*, vol. 1, no. 3, pp. 225–231, Dec. 1957.

[146] I. Finnie, "Some observations on the erosion of ductile metals," *Wear*, vol. 19, no. 1, pp. 81–90, Jan. 1972.

[147] I. M. Hutchings, "Deformation of metal surfaces by the oblique impact of square plates," *Int. J. Mech. Sci.*, vol. 19, no. 1, pp. 45–52, Jan. 1977.

[148] R. E. Winter and I. M. Hutchings, "Solid particle erosion studies using single angular particles," *Wear*, vol. 29, no. 2, pp. 181–194, Aug. 1974.

[149] I. M. Hutchings, "Mechanisms of the erosion of metals by solid particles," *Eros. Prev. Useful Appl. ASTM STP*, vol. 664, pp. 59–76, 1979.

[150] I. Finnie, A. Levy, D. H. McFadden, S. M. Wolf, and N. H. Macmillan, "Fundamental mechanisms of the erosive wear of ductile metals by solid particles. Discussion," *ASTM Spec. Tech. Publ.*, no. 664, pp. 36–58, 1979.

[151] R. A. Mayville, "Mechanisms of material removal in the solid particle erosion of ductile materials," *Lawrence Berkeley Natl. Lab.*, 2011.

[152] J. F. Santa, J. C. Baena, and A. Toro, “Slurry erosion of thermal spray coatings and stainless steels for hydraulic machinery,” *Wear*, vol. 263, no. 1–6, pp. 258–264, Sep. 2007.

[153] D. Kumar Goyal, H. Singh, H. Kumar, and V. Sahni, “Slurry erosion behaviour of HVOF sprayed WC–10Co–4Cr and Al2O3+13TiO2 coatings on a turbine steel,” *Wear*, vol. 289, pp. 46–57, Jun. 2012.

[154] R. C. Shivamurthy, M. Kamaraj, R. Nagarajan, S. M. Shariff, and G. Padmanabham, “Influence of microstructure on slurry erosive wear characteristics of laser surface alloyed 13Cr–4Ni steel,” *Wear*, vol. 267, no. 1–4, pp. 204–212, Jun. 2009.

[155] S. Das, B. K. Prasad, A. K. Jha, O. P. Modi, and A. H. Yegneswaran, “Three-body abrasive wear of 0.98% carbon steel,” *Wear*, vol. 162–164, pp. 802–810, Apr. 1993.

[156] H. C. Meng and K. C. Ludema, “Wear models and predictive equations: their form and content,” *Wear*, vol. 181–183, pp. 443–457, Mar. 1995.

[157] J. G. A. Bitter, “A study of erosion phenomena part I,” *Wear*, vol. 6, no. 1, pp. 5–21, Jan. 1963.

[158] M. Hashish, “An improved model of erosion by solid particle impact,” 1987, p. 66.

[159] M. M. Salama, “Sand production management,” *J. Energy Resour. Technol.*, vol. 122, no. 1, pp. 29–33, 2000.

[160] M. M. Salama, “Influence of sand production on design and operations of piping systems,” in *In CORROSION 2000*, 2000.

[161] S. Shirazi and B. McLaury, “Generalization of the API RP 14E Guideline for erosive services,” *JPT. J. Pet. …*, pp. 693–698, 1995.

[162] K. B. Yoo, J. Y., Ahn, S. S., Seo, D. H., Song, W. H., & Kang, “New development of high grade X80 to X120 pipeline steels,” *Mater. Manuf. Process.*, vol. 26, no. 1, pp. 154–160, 2011.

[163] J.-Y. Yoo, S.-S. Ahn, D.-H. Seo, W.-H. Song, and K.-B. Kang, “New Development of High Grade X80 to X120 Pipeline Steels,” *Mater. Manuf. Process.*, vol. 26, no. 1, pp. 154–160, 2011.

[164] B. Madsen, “No Title,” *Wear Erosion, Met. Corros.*, vol. G119–09, pp. 1–7, 1994.

[165] ASTM, “Standard Test Method for Conducting Erosion Tests by Solid Particle Impingement Using Gas Jets,” *ASTM Int.*, vol. G76–07, pp. 1–6, 2013.

[166] J. N. Kamalu, N., Wen, F., Troutt, T. R., Crowe, C. T., & Chung, "Particle dispersion by ordered motion in turbulent mixing layers," *ASME Cavitation Multiph. Flow Forum*, pp. 150–154, 1988.

[167] F. Wen, "A study on particle dispersion in two-dimensional mixing layer flows.," 1990.

[168] B. A. Lindsley and A. R. Marder, "The effect of velocity on the solid particle erosion rate of alloys," *Wear*, vol. 225–229, pp. 510–516, Apr. 1999.

[169] H. S. Grewal, A. Agrawal, and H. Singh, "Slurry Erosion Mechanism of Hydroturbine Steel: Effect of Operating Parameters," *Tribol. Lett.*, vol. 52, no. 2, pp. 287–303, 2013.

[170] M. A. Islam and Z. N. Farhat, "The synergistic effect between erosion and corrosion of API pipeline in CO2 and saline medium," *Tribol. Int.*, vol. 68, pp. 26–34, Dec. 2013.

[171] K. . Tan, R. J. . Wood, and K. . Stokes, "The slurry erosion behaviour of high velocity oxy-fuel (HVOF) sprayed aluminium bronze coatings," *Wear*, vol. 255, no. 1–6, pp. 195–205, Aug. 2003.

[172] H. M. Clark, "A comparison of the erosion rate of casing steels by sand-oil suspensions," *Wear*, vol. 150, no. 1–2, pp. 217–230, Oct. 1991.

[173] H. Grewal, H. S., Agrawal, A., & Singh, "Slurry Erosion Mechanism of Hydroturbine Steel: Effect of Operating Parameters," *Tribol. Lett.*, vol. 52, no. 2, pp. 287–303, 2013.

[174] Y. I. Oka, M. Matsumura, and T. Kawabata, "Relationship between surface hardness and erosion damage caused by solid particle impact," *Wear*, vol. 162–164, pp. 688–695, Apr. 1993.

[175] G. Sundararajan, "The depth of plastic deformation beneath eroded surfaces: The influence of impact angle and velocity, particle shape and material properties," *Wear*, vol. 149, no. 1–2, pp. 129–153, Sep. 1991.

[176] H. S. Arora, H. S. Grewal, H. Singh, and S. Mukherjee, "Zirconium based bulk metallic glass—Better resistance to slurry erosion compared to hydroturbine steel," *Wear*, vol. 307, no. 1–2, pp. 28–34, Sep. 2013.

[177] Z. B. Zheng, Y. G. Zheng, W. H. Sun, and J. Q. Wang, "Erosion–corrosion of HVOF-sprayed Fe-based amorphous metallic coating under impingement by a sand-containing NaCl solution," *Corros. Sci.*, vol. 76, pp. 337–347, Nov. 2013.

[178] Q. B. Nguyen, C. Y. H. Lim, V. B. Nguyen, Y. M. Wan, B. Nai, Y. W. Zhang, and M. Gupta, “Slurry erosion characteristics and erosion mechanisms of stainless steel,” *Tribol. Int.*, vol. 79, pp. 1–7, Nov. 2014.

[179] T. Foley and A. Levy, “The erosion of heat-treated steels,” *Wear*, vol. 91, no. 1, pp. 45–64, Oct. 1983.

[180] A. V. Levy, J. Yan, and J. Patterson, “Elevated temperature erosion of steels,” *Wear*, vol. 108, no. 1, pp. 43–60, Mar. 1986.

[181] A. K. Chauhan, D. B. Goel, and S. Prakash, “Solid particle erosion behaviour of 13Cr–4Ni and 21Cr–4Ni–N steels,” *J. Alloys Compd.*, vol. 467, no. 1–2, pp. 459–464, Jan. 2009.

[182] T. Alam, M. Aminul Islam, and Z. N. Farhat, “Slurry Erosion of Pipeline Steel: Effect of Velocity and Microstructure,” *J. Tribol.*, vol. 138, no. 2, p. 021604, 2015.

Appendix A

Materials Characterization

Table A-1 Inductively Coupled Plasma Mass Spectrometry (ICP) analysis for carbon and pipeline steels.

Elements	AISI 1018	AISI 1080	API X42	API X70	API X80	API X100	API X120
C	0.182	0.814	0.169	0.061	0.14	0.103	0.14
Si	0.095	0.120	0.067	0.150	0.12	0.151	0.13
Mn	0.754	0.598	0.372	1.223	0.55	1.221	0.56
Cr	0.181	0.122	0.027	0.018	0.06	0.070	0.07
P	0.040	0.040	0.040	0.010	0.01	0.010	0.01
Cu	0.186	0.230	0.008	0.008	0.02	0.009	0.019
Ti	0.008	0.001	0.002	0.015	0.004	0.018	0.001
V	0.001	0.021	0.001	0.028	0.03	0.036	0.01
S	0.021	0.014	0.004	0.002	0.001	0.001	0.001
Mg	0.001	0.002	0.002	0.001	0.001	0.002	0.001
Mo	0.052	0.012	0.001	0.001	0.001	0.009	0.001
Na	0.003	0.003	0.005	0.004	0.0004	0.004	0.0003
Ni	0.173	0.055	0.006	0.006	0.019	0.007	0.019
W	<0.005	<0.005	<0.005	<0.005	0.005	0.021	0.005
Nb	<0.001	<0.001	<0.001	0.057	0.0021	0.058	0.0025
Zn	<0.005	0.006	<0.005	0.001	0.001	0.001	0.001
Zr	<0.001	<0.001	<0.001	<0.001	<0.001	<0.001	<0.001
Ta	<0.010	<0.010	<0.010	<0.010	<0.010	<0.010	<0.010
Te	<0.010	<0.010	<0.010	<0.010	<0.010	<0.010	<0.010
Ge	<0.010	<0.010	<0.010	<0.010	<0.010	<0.010	<0.010
In	<0.010	<0.010	<0.010	<0.010	<0.010	<0.010	<0.010
K	<0.005	<0.005	<0.005	<0.005	<0.005	<0.005	<0.005
La	<0.001	<0.001	<0.001	<0.001	<0.001	<0.001	<0.001
Li	<0.001	<0.001	<0.001	<0.001	<0.001	<0.001	<0.001
Fe	balance	balance	balance	balance	balance	balance	balance